The application of mechanism based and equivalent frame methods for the seismic assessment of URM terraced houses in Groningen

Romy Brouwer

July 10, 2020

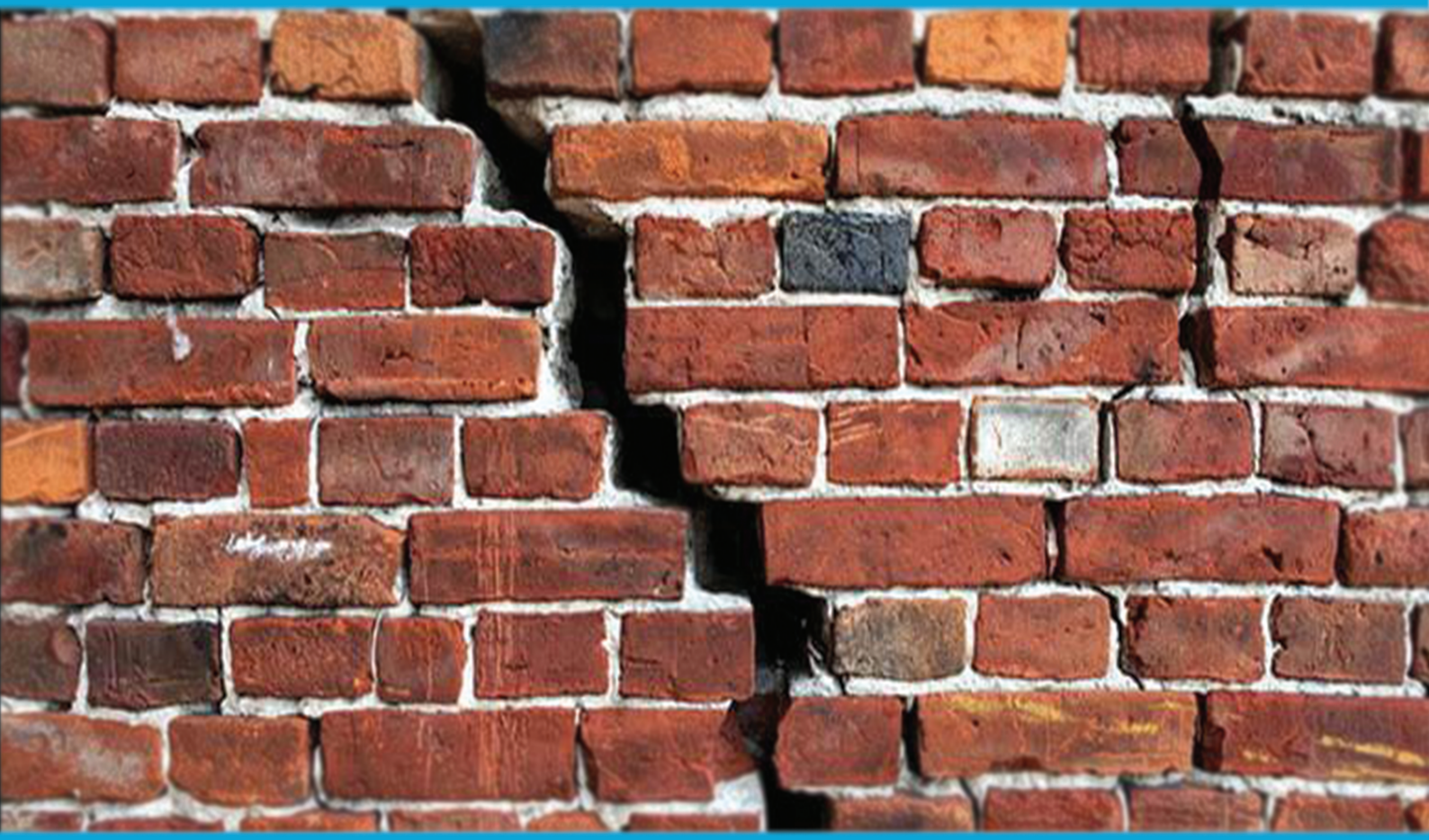

TU Delft

THE APPLICATION OF MECHANISM BASED AND EQUIVALENT FRAME METHODS FOR THE SEISMIC ASSESSMENT OF URM TERRACED HOUSES IN GRONINGEN

A thesis submitted to the Delft University of Technology in partial fulfillment of the requirements for the degree of

Master of Science in Building Engineering

by

Romy Brouwer

July 2020

Cover photo: Fantastic Handyman Team (2018)

The work in this thesis was made in the:

Building Engineering
Faculty of Civil Engineering
Delft University of Technology

Supervisors: Prof. dr. ir. J.G. Rots
Ir. S. Pasterkamp
Dr. F. Messali

SUMMARY

Since the 60's the Nederlandse Aardolie Maatschappij (NAM) has been extracting gas from the province of Groningen in the Netherlands. This resulted into seismic activity. However, the buildings in Groningen are not designed to withstand any seismic loading. The assessment of the seismic behavior of the building stock of Groningen is required to verify whether a structure causes any life safety risk during an earthquake.
In this thesis two main objectives are studied. Firstly, it is studied whether the simplified analysis approaches: Simplified Lateral Mechanism Analysis (SLaMA), as described in the NPR9998-2018, and the Equivalent Frame Method (EFM) as implemented into the software package 3Muri are able to describe the seismic behavior of an Unreinforced Masonry (URM) terraced house. Secondly, the influence of the geometry of the piers in a facade is assessed. Both the objectives are studied by means of two case studies.

The first case study served as a verification of the use of the SLaMA method and the 3Muri software with version 12.2.1.4. A relative simple two-storey structure of a typical but idealized URM terraced house was tested in the TU Delft lab under cyclic pushover load. The structure consists of slender piers in combination with large openings without spandrels to connect the piers. This resulted into difficulties in the modelling process with 3Muri. In fact, the floor is not included in the mesh and an element which connects the piers was required. A reinforced concrete beam and a reinforced concrete lintel were used as connecting element, initially the properties of these connecting elements are similar as the floor. A sensitivity study has been performed to conclude which model represented the physical model most accurately. For the sensitivity study the stiffness of the connecting element and the load distribution of the floor during the initial static conditions towards the piers is varied. It must be noted that the Eurocode 8 was used as guideline since the results obtained with the NPR9998-2018 were not realistic. The piers remained undamaged during the analysis with the NPR9998-2018, but still the seismic capacity was lower than the seismic demand.

From the sensitivity study it was concluded that varying the load distribution of the floor during the initial static condition towards the piers or decreasing the stiffness of the connecting element, resulted into changes of the internal load distribution which are not in line with the physics. The flange effect was no longer visible in the corresponding piers. Additionally, the drift varies per element even if located on the same floor level. The reinforced concrete beam with similar properties as the floor and the floor spanning between the transverse walls was chosen as best representation of the physical model, even though the seismic capacity was highly underestimated.
The outcome of the first case study has shown that the SLaMA method gives a conservative but valid indication about the seismic behavior of this URM structure. The outcome of the EFM as implemented into the software 3Muri highly underestimated the seismic capacity. Due to the limitations in the software, the current employed version of 3Muri is not suitable to represent the URM terraced house structure without spandrels.

The second case study concerns a specific two-storey URM terraced house which consists of a block of four units. The case study is located in Groningen and serves as a validation of the SLaMA method and 3Muri software on a larger building scale. The results obtained with 3Muri were mainly based on the Eurocode 8 assumptions. The reliability of the results obtained with the NPR9998-2018 as guideline were namely questionable, the 50% strength decay is not reached

while a significant percentage of the elements has failed.
A proper indication was given by 3Muri and SLaMA. However, it is possible that the assumptions which where made during the analysis influenced the results and are not an accurate representation of the seismic behavior. To start with SLaMA, it is assumed that the piers capacity is governing over the spandrels capacity. Additionally, it is determined by the user (from an engineering point of view) whether dynamic instability is reached. In 3Muri it is not possible to include the concrete lintels which are present in the case study. The concrete lintels are therefore replaced by URM lintels. For both the models determined with SLaMA and 3Muri it was chosen to neglect the outer leaf for the in-plane assessment.
There are no experimental results for a benchmark and therefore more research is required in order to validate the results. The benchmark can be obtained by either experimental or numerical research with more advanced modelling strategies.

Finally, the influence of the geometry of the piers in the facade on the seismic behavior is analyzed. Three models are created in which the total area of openings is equal, but the width of the openings is varied while their height is adapted accordingly. The seismic behavior is analyzed with SLaMA and 3Muri. The 3Muri models are created with both the Eurocode 8 and the NPR9998-2018 as guideline.
The analysis showed that the governing failure mechanism is decisive for the seismic behavior of the structure. The results obtained with the variation study are implemented in a final proposal for an improved design of the facade of the second case study. Since the influence of the governing failure mechanism is decisive for the seismic behavior, the geometry of the piers is adjusted in such a way that the flexural failure mechanism is governing for all the piers in the improved design. The adjustments are based upon the equations as formulated in the NPR9998-2018. The new geometry of the facade leads to improved results for the SLaMA method because this mechanism is determined by the NPR9998-2018 at local and global level as ductile failure mechanism. The new geometry doesn't lead to significant changes in the results obtained with 3Muri.

ACKNOWLEDGEMENTS

This thesis is written in order to complete my Master Building Engineering at the Faculty of Civil Engineering and Geosciences at Delft University of Technology. In this report the seismic behavior of URM terraced houses in the province of Groningen in the Netherlands is analyzed. The analysis are computed with two simplified methods: SLaMA and the equivalent frame method as implemented into the software 3Muri.

Through this way I would like to thank my graduation committee members. First of all I would like to thank my daily supervisor Francesco Messali for his guidance and help during this process. Thank you for helping me with all my questions during this process. I also would like to thank the other members of my committee Jan Rots and Sander Pasterkamp for their feedback during the committee meetings.

Finally, I would also like to thank my friends, family and roommates for their support and motivation during my thesis.

Romy Brouwer
Delft, July 2020

CONTENTS

LIST OF FIGURES

LIST OF TABLES

ACRONYMS

ADRS Acceleration Displacement Response Spectrum 1
CS Calcium Silicate 35
EFM Equivalent Frame Method v
FEM Finite Element Modelling 74
MDoF Multi Degree of Freedom 15
NC Near Collapse xix
NAM Nederlandse Aardolie Maatschappij v
NLPO Non Linear Pushover 1
PGA Peak Ground Acceleration 16
SLaMA Simplified Lateral Mechanism Analysis v
SDoF Single Degree of Freedom 15
ULS Ultimate Limit State 10
URM Unreinforced Masonry v

1 INTRODUCTION

1.1 PROBLEM DESCRIPTION

Since the 60's the NAM has been extracting gas from the province of Groningen in the Netherlands. The gas field in Groningen is the largest gas field in Europe. With the extraction of gas from the reservoir, stress is released from the soil which leads to a stress redistribution and subsequently compaction of the reservoir. Consequently, shallow earthquakes of relative low magnitude are induced. However, the buildings in Groningen are not designed to withstand any seismic loading and are vulnerable to such loading.
The building stock of Groningen is inspected to verify the seismic capacity of a structure and whether a structure creates any life safety risk if subjected to seismic loading. However, the assessment of the seismic capacity with advanced models is time consuming and additionally it is impossible to use complex modelling techniques in order to determine the seismic capacity of the individual buildings in the total building stock of Groningen. Furthermore, the strengthening process for the structures which are most vulnerable should start as soon as possible in order to prevent any life safety risk due to another earthquake. The use of a method with relative low computation time is preferred in order to give a quick indication about the seismic capacity of a structure.

The building stock of Groningen is classified by ARUP & NAM (2018) into different typologies. The classification is based upon similarities within the geometric and structural layout and the materials used in the structure. It is expected that buildings within a specific typology show similarities within the structural behavior and its failure mechanisms. With the classification, the seismic capacity of a structure can be determined and it is assumed that the seismic behavior is quite similar for all the buildings within a typology. However, the geometrical properties of the facade are not taken into account. A study into the classification process would be useful in order to verify whether the buildings within a typology show similarities as regards the seismic behavior.

In this thesis the focus will be on the assessment of the Non Linear Pushover (NLPO) method. With this method the capacity curve of a structure can be obtained and subsequently compared to the seismic demand in an Acceleration Displacement Response Spectrum (ADRS) format. Two methods from which the non linear capacity curve can be obtained will be analyzed and validated for a typical building in Groningen.
Firstly, the SLaMA method which is a simplified analysis technique will be studied. The SLaMA method gives an indication of the seismic capacity of a structure via an analytical approach. The technique is less time consuming and could be used as a first step in the analysis of the seismic capacity of a structure. Secondly, the EFM as implemented into the software 3Muri will be analyzed. The computational time is less since the masonry walls are considered as an idealized frame in which the wall is divided into a set of macro-elements. Therewith the total amount of degrees of freedom is limited, still it is possible to analyze complex structures (Lagomarsino et al., 2013).
A significant amount of the Groningen building stock are the URM terraced houses (ARUP & NAM, 2018). For this reason the focus in this thesis will lie on the typology URM terraced houses.

The applicability of both the SLaMA method and the EFM as implemented into the software 3Muri to an URM terraced house structure will be studied. A comparison between both methods is made in order to give a validation of the workability of the methods and whether these methods are able to describe the seismic behavior.

Another aspect related to the verification of the strength of the structures lies in the validation of the classification process. The geometrical aspects of the piers in the facade will be varied since this aspect is not taken into account in the classification process. The influence of the geometry of the piers on the seismic behavior of an URM terraced house structure will be analyzed with both SLaMA and 3Muri.

1.2 RESEARCH QUESTIONS

In this report the main focus will be on the problem description as described above, with as main goal to find an answer to the following two research questions:

1. To what extent are the SLaMA method and the equivalent frame approach as implemented in the software package 3Muri able to describe the seismic behavior of an URM terraced house in Groningen

2. To what extent is the seismic behavior of an URM terraced house case study in Groningen influenced by the variation of the geometry of the facades?

In order to formulate an answer to the main research questions, two case studies will be analyzed. Both the case studies concern specific URM terraced house structures. Both the SLaMA method and the 3Muri software will be used in order to describe the seismic capacity of these case studies. The SLaMA method will be applied as described in the NPR9998-2018. For the analysis with the software 3Muri the focus will be mainly on the Eurocode 8 as guideline.

1.3 REPORT STRUCTURE

The report consists of five parts which will be elaborated here:

1. Literature study

A literature study is executed in order to provide the background information on the behavior of URM structures during an earthquake. Firstly, the mechanical properties of masonry and the failure mechanisms of URM structures will be elaborated. Secondly, the seismic analysis methods which are studied in this thesis are introduced: the SLaMA method, as described in the NPR9998-2018, and the EFM as implemented into the software 3Muri. The EFM will be studied mainly based upon the Eurocode 8 assumptions.

2. Case study 1

In the second part of the thesis the knowledge obtained in the literature study will be applied to a case study. The case study concerns a two storey URM structure from which the seismic performance was tested in the TU Delft lab under cyclic pushover load. The seismic capacity will be determined according to the SLaMA method and the EFM as implemented in the software 3Muri and compared to the results obtained in the lab.

3. Case study 2

Thirdly, a new case study will be introduced. The second case study regards the Martini type K house located in Loppersum in the region Groningen. The case study concerns an URM terraced house from the typology "block unit multiple". The seismic capacity of the Martini type K structure is determined according to the SLaMA method and the 3Muri software. At the end of the analysis the results obtained with both the methods will be compared to each other. The second case study serves as a second validation of the SLaMA method and the software 3Muri on a larger building scale.

4. Variation study

In the fourth part of this report the different parameters which affect the geometry of the facade, and consequently the seismic behavior of a structure are analysed. The URM terraced house as introduced in case study 2 will be used for the variation study. The influence of the parameters are analyzed with the SLaMA method according to the NPR9998-2018 and the 3Muri software according to the Eurocode 8. Additional analyzes will be made with 3Muri according to the NPR9998-2018. The results obtained from the variation study will be implemented in a final proposal for an improved design.

4. Conclusion and recommendations

A final answer will be given to the two research questions in the conclusion. Additionally, the recommendations will be described for further research.

2 THE STRUCTURAL BEHAVIOUR OF MASONRY

In this chapter the structural behaviour of an URM structure will be elaborated. Firstly, more insight will be given in the mechanical properties of masonry. The mechanical properties are studied on micro level and explained more in detail based upon earlier research. In the second part of this chapter the structural behaviour of masonry on macro level will be elaborated. The failure mechanisms of URM structures will be studied, a division is made in elements loaded in-plane and out-of-plane.

2.1 THE MECHANICAL PROPERTIES OF MASONRY

An URM structure is composed out of brick elements which are connected to each other by mortar. The strength of masonry is mainly determined by the type of brick and the composition of the mortar (Mosalam et al., 2009). Due to the different material properties and geometry of the bricks and the mortar, masonry is considered as a an-isotropic material. Therewith the predicting of the behaviour of a masonry structure can be rather complex.

Since masonry is composed out of brick elements and mortar, the interaction between these elements is an important aspect of the load bearing capacity. The behaviour of masonry depends upon the strength of the individual components and the connection between the components. Generally the brick-mortar interface is the weakest link of masonry (Angelillo, 2014). The bond between the bricks and the mortar ensures the connection between the elements. Through this connection horizontal forces can be transferred by adhesion and/or friction (Pfeifer et al., 2001). Additionally, the interface and the mortar (in the bed joints) helps to distribute the vertical forces equally over the brick elements, in other words stress concentrations in masonry are prevented.

Both the bricks and the mortar behave almost similar in compression and tension. The materials have sufficient compressive strenght (σ_c), and a lower tensile capacity (σ_t). The ratio σ_t/σ_c of masonry can reach a minimum value of 0.01, but is generally 0.1 (Angelillo, 2014). Simple compression and tensions tests have been executed on a masonry wall by Angelillo (2014), the relation between the stress- and displacement is represented in figure Figure 2.1. The graphs are only qualitative and as previously stated the ratio σ_t/σ_c lies within a range of 0.01 – 0.1.

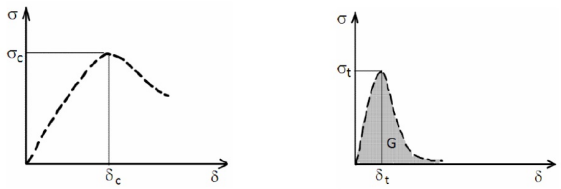

(a) Compression **(b)** Tension

Figure 2.1: Stress-displacement graph masonry.
Source: Angelillo (2014)

2.1.1 Behavior of the brick units

The bricks units are considered to be heterogeneous which behave quasi-brittle. As the brick is loaded in compression it behaves linear elastic until the peak load is reached. After the development of the first micro-cracks the material starts to harden; the material stiffness decreases, but it it still possible to increase the load. With a further increase of the load, more micro-cracks develop in the element. After the peak load is reached softening behavior can be observed, softening is a decrease of the mechanical resistance of the element while the deformations increase continuously, see Figure 2.2a (Angelillo, 2014). The micro cracks in the brick are initially stable that is to say that the micro cracks develop only with an increase of the load. When approaching the peak load the cracks develop into macro cracks which are considered to be unstable. Further increase of the load results in a uncontrolled development of the cracks (Laurenço, 1996). Similar behavior can be observed for the element in tension, see Figure 2.2b. The material behaves linear elastic until the peak load is reached, the micro cracks are stable until the peak load is reached. Subsequently the micro-cracks develop into macro-cracks, softening behavior can be observed. The bricks compressive capacity is much higher than the tensile capacity as explained with Figure 2.1

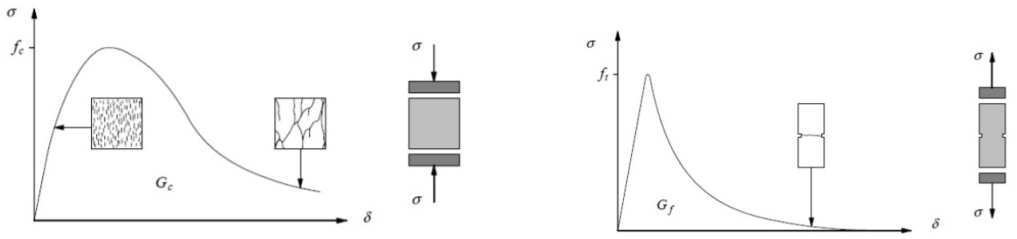

(a) Compression **(b)** Tension

Figure 2.2: Mechanical behavior bricks.
Source: Angelillo (2014)

2.1.2 Compressive behavior

If masonry is loaded in compression into the direction normal to the head joints, the bricks start to deform into the transverse direction. The deformability capacity of the mortar is higher than the deformability capacity of the bricks, the mortar starts to deform horizontally (Hayen et al., 2004). The bond between the bricks and mortar obstruct the deformation of the mortar with respect to the bricks. Consequently, tensile stresses develop in the bricks and compressive stresses in the mortar, see Figure 2.3. To conclude, the compressive strength of the masonry is dependent upon the tensile capacity in the transverse direction of the bricks. Additionally, the tensile stresses can decrease because of the cross contraction (Pfeifer et al., 2001). Unfortunately there is no literature available which considers the behaviour of the masonry loaded into the direction normal to the bed joints.

As a final point, the compressive strength of the masonry reduces if the structure is exposed to cyclic compressive loads. The tensile stresses which develop in the bricks after the deformation of the mortar, partly remain after the unloading of the masonry. Hence, the tensile transverse stresses accumulate over time in the bricks. Consequently, this can lead to the failure of the masonry where the tensile stresses in the bricks become too large (Pfeifer et al., 2001).

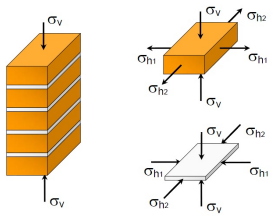

Figure 2.3: Stress distribution masonry subjected to compression.
Source: Hayen et al. (2004)

2.1.3 Tensile behavior

For masonry under tension normal to the bed joints, the tensile stresses are transferred by means of shear resistance through the bed joints (Pfeifer et al., 2001). Generally the head joints are not able to transfer tensile stresses since the adhesive tensile strength in the head joints is very low. Two type of failure can be distinguished for in the direction normal to the bed joints. In Figure 2.4 the stress-displacement curve for both the corresponding cracking patterns is visualized. In the first type the bricks have a higher tensile strength than the mortar. In this situation the mortar cracks and a zigzag pattern develops (a). For the second failure type the mortar has a higher tensile strength than the bricks. In this situation the bricks crack, a straight cracks develops through the bricks (b).

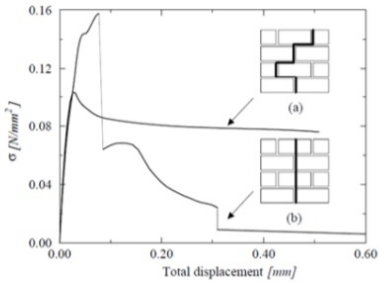

Figure 2.4: Stress displacement curve for masonry loaded in tension (direction: normal to the bed joints).
Source: Backes (1985)

The stress-displacement curve which belongs to crack pattern (a) first shows linear elastic behaviour. After the maximum tensile strength of the bed joints is reached, the load can still be transferred by means of shear. For the stress-displacement curve which belongs to crack pattern (b) an increase of the tensile stress can be found until the bricks fail. After the failure the curve decreases, this can be determined as softening behaviour.

For masonry which is loaded in the direction normal to the head joints, the structure is mainly dependent upon the adhesive tensile strength between the bricks and the mortar layer. Two failure modes for this situation have been observed for the masonry. In the first failure mode the interface between the bricks and the mortar has failed. In the second failure mode the tensile strength of the bricks is exceeded, resulting in a crack through the bricks.

2.1.4 Shear behavior

Masonry behaves quite similar under shear as it does in tension, in Figure 2.5 the relation between the shear stress over the shear displacement is presented. After the development of the micro-cracks into macro-cracks, the shear stress which can be transferred decreases rapidly. In contrast to the tensile behaviour of masonry, the capacity to transfer any shear stresses stabilizes if there are compressive stresses present.

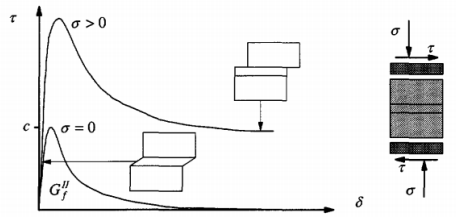

Figure 2.5: Relation between the shear stress and shear displacement of masonry.
Source: Laurenço (1996)

Experiments have been performed by van der Pluijm (1999) in order to describe the shear behavior of a masonry element loaded in both shear and compression. An experimental setup was used which was able to apply compressive stresses and keep this constant in combination with an applied increasing shear load. The results from the experiment are visualized in Figure 2.6. From the results obtained in Figure 2.6b it can be concluded that with an increase of the compressive stress, the shear capacity increases as well. After the cracking of the interface there is still some adhesion between the bricks and the mortar, this coheres with the compressive stresses. The shear stress can be transferred here by means of dry friction. The stabilization of the graphs, after the cracking of the masonry, is thus due to the presence of compressive stresses.

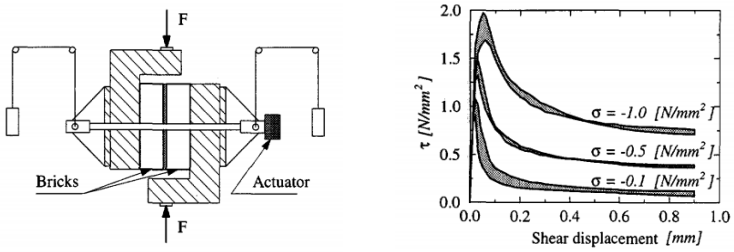

(a) Setup shear experiments **(b)** Results experiment

Figure 2.6: Shear behavior masonry element.
Source: van der Pluijm (1999)

2.1.5 Brick-mortar interface

The connection between the bricks and the mortar is also known as the interface and is generally the weakest link in masonry according to Angelillo (2014). In other words, cracks are usually concentrated in this area. The strength of the interface is determined by the material properties of the bricks and the mortar and the workmanship. Experimental research as regards the interface was done by van der Pluijm (1992), he found that the parts where the brick and the mortar are bonded to each other is smaller than the cross-sectional area. The bond area was generally located at the center of the brick, which could be due to shrinkage of the mortar and the construction process (Angelillo, 2014). In Figure 2.7 the observations by van der Pluijm (1992) are visualized of the net bond surface area.

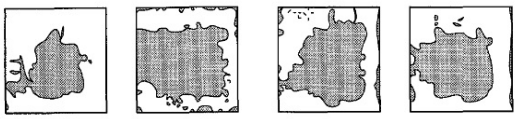

Figure 2.7: Typical net bond surface area.
Source: van der Pluijm (1992)

Two different failure modes can be distinguished as regards failure of the interface; mode I and mode II. The mode I failure is related to the tensile failure of the interface. Experimental research which was performed by van der Pluijm (1992) resulted in an exponential softening curve. The fracture energy (G_f) of this failure mode was 0.005 to 0.02 Nmm/mm^2.
Failure mode II is related to the shear behavior of the interface. Similar as for failure mode I, exponential softening can be observed. This is based upon the same experiment as described in Section 2.1.4. The fracture energy of this failure mode was 0.01 to 0.25 Nmm/mm^2.

2.1.6 Biaxial behaviour

For the description of the biaxial behaviour of masonry both the principal stresses and the orientation of the principal stresses with respect to the orientation of the bricks should be taken into account according to Laurenço (1996). The rotation of the principal stresses should also be taken into account because masonry is a an-isotropic material. Page (1982) tested the constitutive behaviour of masonry where the orientation of the bricks varied from the orientation of the principal stresses. For panels in biaxial compression failure generally occurred at the middle of the wall due to splitting parallel to the free surface. This despite the orientation of the principal stresses, see Figure 2.8a (Page, 1982). In Figure 2.8b the failure surface of the panel is shown with its corresponding orientation of the principal stresses. If the principal stress is on or outside the failure surface, the material fails. The increase of the compressive capacity when the panel is in biaxial compression can be clarified with the same tests as explained in Section 2.1.4.

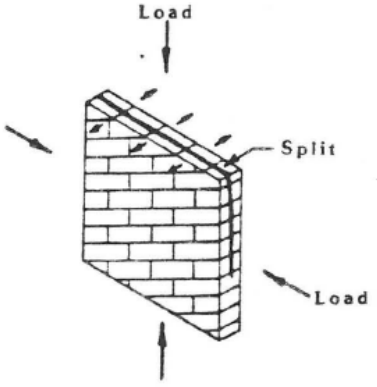

(a) Failure mode biaxial compression

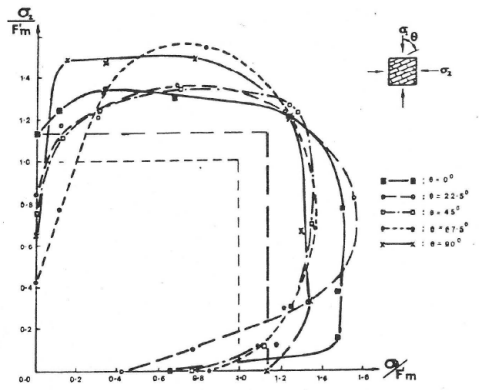

(b) Failure surface masonry under biaxial compression

Figure 2.8: Biaxial behaviour masonry.
Source: Page (1982)

2.2 FAILURE MECHANISMS

During a seismic event a distinction can be made between in-plane and out-of-plane failure mechanisms. The failure mechanisms which can develop if an element is loaded in or out-of-plane are elaborated here. Finally more insight will be given in the overall behavior of an URM structure based upon the type of diaphragm in the structure.

2.2.1 In-plane failure modes

For vertical elements loaded in-plane, three possible failure mechanisms can develop according to Kilar and Petrovc (2013). In Figure 2.9 the possible failure mechanism are visualized: flexural failure, shear sliding failure and diagonal cracking failure. The failure mechanism which is governing over these three depends upon various parameters such as the geometry of the pier, the boundary conditions, the mechanical properties and geometry of the masonry components and the axial load in the element (Calderini et al., 2009).

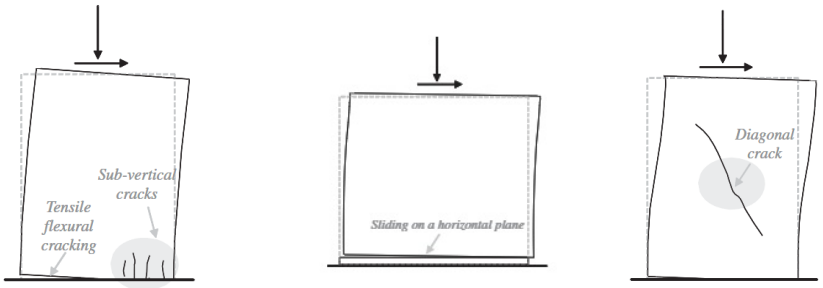

(a) Flexural **(b)** Shear sliding **(c)** Diagonal cracking

Figure 2.9: Failure mechanisms vertical elements.
Source: Calderini et al. (2009)

Flexural

In the literature a distinction is made within the flexural failure mechanism between rocking and toe crushing. In both the mechanisms the failure of the compressed corner is governing in the Ultimate Limit State (ULS) (Calderini et al., 2009).
The first failure mechanism is also known as rocking and occurs mainly in slender piers in combination with low vertical load. In order to explain the rocking mechanism, a relative low vertical load is applied in combination with a lateral load. Due to the lateral loading, the element starts to rotate around its compressed corner. Originally the stress distribution is linear elastic, but due to the rotation the normal stresses in the outer fiber approach zero and subsequently the first cracks develop (Vaculik, 2012). The development of the normal stresses in the pier is visualized in Figure 2.10.
The effective uncracked length of the element decreases and the resultant compressive force moves into the direction of the compressed corner, the stress distribution is nonlinear here (Vaculik, 2012). The effective uncracked length of the cross-section is the length of the area which is able to still transfer the compressive force in the pier. The effective uncracked length for a rectangular cross-section is expressed as (Magenes and Calvi, 1997):

$$l_{eff} = \beta l_w = 3 \cdot (\frac{1}{2} - \frac{V_r}{P}\frac{H_0}{l_w}) \cdot l_w \tag{2.1}$$

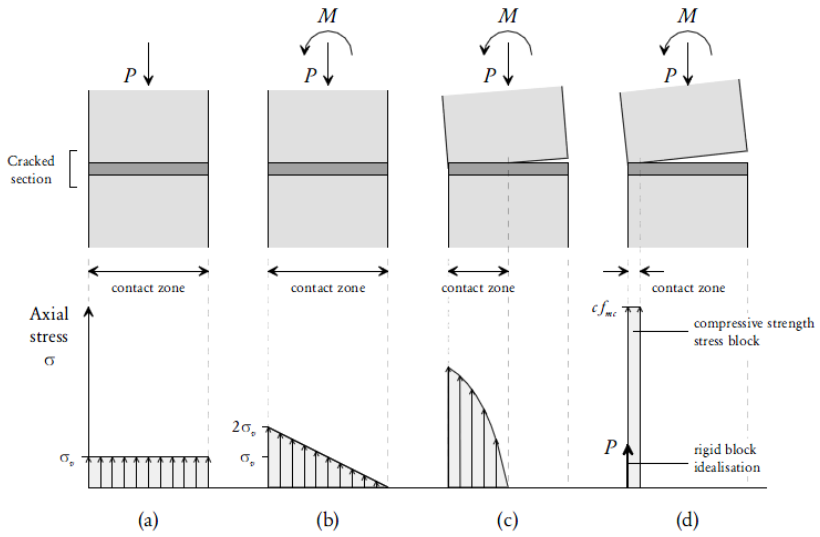

Figure 2.10: Development of the normal stresses in a pier, when subjected to a moment.
Source: (Vaculik, 2012)

This is the area of the cross-section which still has a contact zone and is able to transfer a compressive force in the pier. In which l_w is the length of the pier, P is the axial loading and H_0 represents the effective height of the pier which is defined by its boundary conditions. This is generally 0.5 times the height for double clamped piers and 1 times the height if the pier is clamped at only one end. In Figure 2.11 the specific forces on the pier and compressed corner are visualized, equilibrium in the element gives the following equation:

$$V_r = \frac{{l_w}^2 \cdot t_w \cdot \sigma_y}{H_0 \cdot 2}(1 - \frac{\sigma_y}{0.85 f'_m}) \tag{2.2}$$

The factor between the brackets is a reduction factor of the shear resistance due to the rotation of the element (Vaculik, 2012). The factor 0.85 is a constant factor which is applicable to rectangular sections. The factor takes the vertical stress distribution at the compressed toe into account (Magenes and Calvi, 1997), f'_m is the compressive strength of masonry and σ_y represents the average vertical stress in the element.

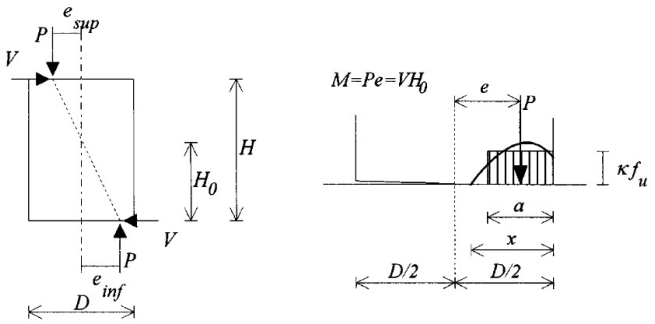

Figure 2.11: Flexural failure mechanism.
Source: Magenes and Calvi (1997)

The second failure mechanism is also known as toe crushing and occurs generally due to the combination of a relative high vertical load (with respect to rocking), in combination with a

lateral load. Due to the high vertical load, the development of the flexural cracks is nearly prevented. However, vertical cracks develop in the compressed corner due to the moment and vertical load.

The maximum shear resistance of element which fails due to toe crushing is described by NZSEE (2017) with the following equation:

$$V_r = (\alpha P + 0.5P_w)(\frac{l_w}{H_0})(1 - \frac{f_a}{0.7 \cdot f'_m})) \tag{2.3}$$

In which α is a factor which takes the boundary conditions into account and is 1.0 for a double clamped pier and 0.5 for a pier which is clamped on one side only. A distinction is made here between the self weight of the element (P) and the load imposed load (P_w), the factor f_a represents the axial compressive stress at the base.

Shear Sliding

The shear sliding failure mechanism occurs mostly in squat piers. A crack develops through the bed joint which is initiated by cracks due to flexure. The shear resistance of the element can be described with the Mohr-Coulomb relation (Magenes and Calvi, 1997). The Mohr-Coulomb relation is expressed with the following equation:

$$\tau = f_{v0} + \mu f_a \tag{2.4}$$

In which f_{v0} is the initial shear strength of masonry, μ is the shear friction coefficient and f_a as maximum average shear stress of effective uncracked section. The uncracked length can be expressed as Equation 2.1, if the section is rectangular. By substituting Equation 2.1 into Equation 2.4, the ultimate shear stress can now be expressed as:

$$V_r = l_w \cdot t_w \cdot \tau = l_w \cdot t_w(f_{v0} + \mu f_a) = l_w \cdot t_w(f_{v0} + \mu \cdot \frac{P}{l_w \cdot t_w}) \tag{2.5}$$

Further elaboration of the equation results into the ultimate shear capacity of the pier:

$$V_r = 3 \cdot (\frac{1}{2} - \frac{V_r}{P}\frac{H_0}{l_w}) \cdot l_{pier} \cdot t(f_{v0} + \mu\sigma_y) = l_w \cdot t\frac{1.5f_{v0} + \mu f_a}{1 + 3\frac{f_{v0}}{f_a}\frac{H_0}{l_w}} \tag{2.6}$$

Diagonal cracking

The diagonal cracking failure mechanism is generally initiated by a crack in the center of the element which spreads towards the corners of the element. According to Kilar and Petrovc (2013) the crack develops through both the mortar joints and the bricks, the crack formation is dependent upon the quality of both the mortar and the bricks.
One of the approaches in order to determine the resistance of a pier is based upon experiments by Turnsek and Cacovic. The approach is based upon the assumption that the strength limit is reached after the stress reaches a critical value. The stress is analyzed at the center of the pier in which the critical value is defined as the tensile strength of the masonry (Magenes and Calvi, 1997). This is expressed with the following equation for double clamped piers as:

$$V_r = \frac{f_{tu} \cdot l_w \cdot t_w}{b}\sqrt{1 + \frac{f_a}{f_{tu}}} \tag{2.7}$$

In which f_{tu} represents the tensile strength of the masonry, in other words the reference value. The factor b represent a shape factor: b=1 for $b/l \leq 1$; b=h/l for $1 \leq b \leq 1.5$; b=1.5 for $h/l \geq 1.5$

2.2.2 Out-of-plane failure modes

Elements which are loaded in the out-of-plane direction undergo bending. With the relative low tensile capacity of an URM wall, the walls subjected to loading into this direction are quite weak. Dependent upon the boundary conditions and eventual constraints along the edges, a certain stress and cracking pattern develops in the element. The out-of-plane behavior of a structure subjected to a seismic load is generally not considered because this isn't part of the primary load path. However, it is important that the walls are properly designed with sufficient capacity in order to avoid out-of-plane failure.
One-way spanning elements subjected to a load out-of-plane, undergo uni-axial bending. A crack develops in the wall which is generally parallel to the supporting edges, see Figure 2.12a.

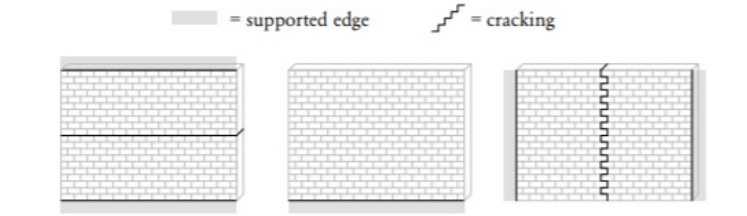

(a) One-way spanning

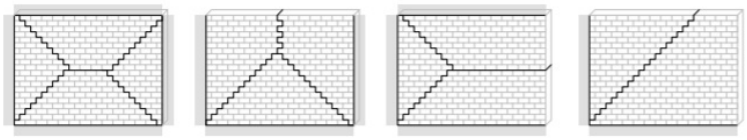

(b) Two-way spanning

Figure 2.12: Cracking pattern wall loaded out-of-plane.
Source: Vaculik (2012)

Two-way spanning elements undergo biaxial bending. The bending stresses are both in horizontal as vertical direction. A cracking pattern develops into multiple directions, see Figure 2.12b.
Not only the boundary conditions but also the quality and strength of the connection influences the out-of-plane behavior. If the walls are poorly connected to the floor, roof or the internal walls, local out-of-plane failure can occur due to seismic loading. According to D'Ayala, D. and Speranza (2003) the failure mechanism which occur mostly during an earthquake is the cantilevering of the street facade with parts of the party walls. Six possible failure mechanisms can be distinguished where the street facade fails out-of-plane, dependent upon the connection of the facade with the walls. In Figure 2.13 the failure modes are visualized. Failure mode A - D are all dependent upon the connection, failure mode E is depended upon the relation between the amount of openings and the width of the piers. Failure mode G and H occur due to a low constraining of the load bearing walls, the wall displaces outwards.

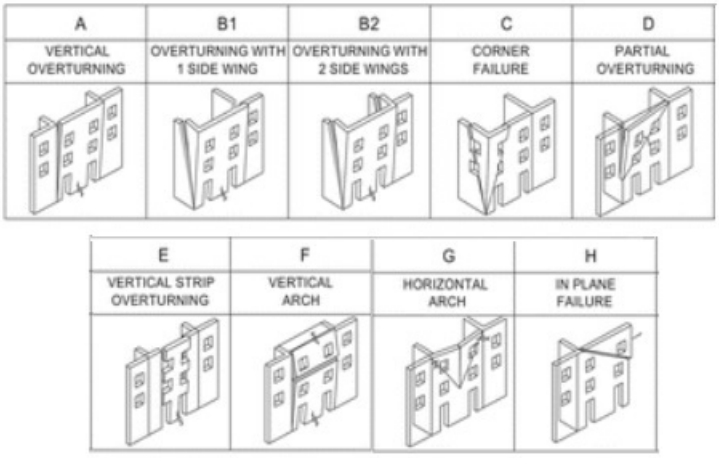

Figure 2.13: Out-of-plane failure modes.
Source: D'Ayala, D. and Speranza (2003)

2.2.3 Diaphragm related failure

For the overall stability of a structure the type of diaphragm in combination with the connection to the load bearing elements is essential, especially during an earthquake. The diaphragm ensures the transfer of lateral loads and ties the walls together during an earthquake. The diaphragm working is also known as 'box-action'.
Structures which have a sufficient diaphragm connection have more potential to withstand an earthquake. With the in-plane capacity, which is generally higher than the out-of-plane strength of masonry, a proper redistribution of the lateral load is essential. With the box-action chance of out-of-plane failure can be limited, and the building is able to use the in-plane capacity optimal. The redistribution is dependent upon the stiffness of the diaphragm and the connection between diaphragm and the masonry wall. In Figure 2.14 the effect of the stiffness of the diaphragm in combination with the connection type is visualised. The connection is thus essential for the overall stability, the connection between the floor and the wall could fail due to failure of the metal or local rupture. With a lack of anchorage, the exterior wall can fall of the building this is also known as cantilevering out-of-plane failure.

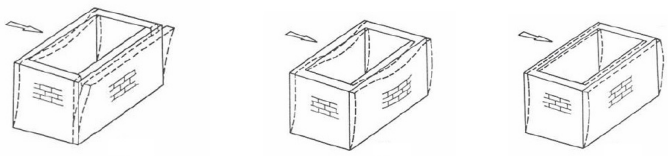

(a) Flexible floors, no ties

(b) Flexible floors, tied walls

(c) Rigid floors, tied walls

Figure 2.14: Influence floor type and connection during earthquake.
Source: NZSEE (2017)

3 SEISMIC ANALYSIS METHODS

In this chapter the seismic analysis methods which are applied in this thesis are elaborated. The approaches which are used are the SLaMA method according to the NPR9998-2018 and the EFM as implemented into the software 3Muri. Both the methods use the NLPO method from which firstly the background will be explained.

3.1 NONLINEAR PUSHOVER METHOD

With the NLPO analysis the probable global seismic capacity of a structure can be determined. The analysis is a nonlinear static method which is generally used to determine the seismic capacity of a structure. For the NLPO analysis it is assumed that the structural response to the first mode of vibration is dominant and that the shape of the first mode is constant. Therewith the dynamic problem can be translated into a static problem (Themelis, 2008). The method is applicable for regularly structures which height is low to medium since the first mode is here generally dominant. The second assumption is that the response of the structure can be represented as a Single Degree of Freedom (SDoF) system (Krawinkler and Seneviratna, 1998).

For the NLPO analysis, a lateral load is applied on the structure and monotonically increased until the NC limit state is reached. With the analysis the relation between the base shear and the top displacement of the structure can be obtained and is presented as a pushover curve, an example is visualized in Figure 3.1.

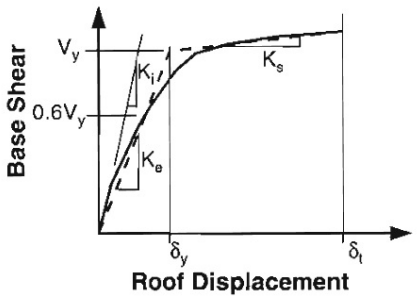

Figure 3.1: Pushover curve.
Source: ATC (1996)

The pushover curve of the structure, which is a Multi Degree of Freedom (MDoF) system, is translated to its equivalent SDoF system with a transformation factor (Γ). The transformation factor is defined in the NEN-EN 1998-1 as:

$$\Gamma = \frac{\Sigma F_i}{\Sigma \frac{F_i^2}{m_i}} \tag{3.1}$$

The base shear force (F) and the displacement (d) of the MDoF system are divided by the transformation factor. The obtained values represent the base shear force (F*) and displacement (d*) of its equivalent SDoF system:

$$F^* = \frac{F}{\Gamma} \qquad d^* = \frac{d}{\Gamma}$$

Finally, the target displacement of the equivalent SDoF system is determined. The target displacement represents the expected displacement of the structure during an earthquake. This is determined by comparing the capacity curve of the equivalent SDoF system with the seismic demand. The earthquake is represented as a response spectrum, a response spectrum represents the reaction of all possible linear SDoF systems to an earthquake. Each systems peak response gives one value of the response spectrum which visualizes the relation between the acceleration and the period.
Finally the design spectrum is used in order to verify the seismic capacity. The design spectrum is the corrected envelope of the measured earthquakes in a specific area since it is impossible to create the spectrum for each earthquake. The response spectrum is dependent upon the soil conditions of the specific area.

3.1.1 Seismic loading

The seismic loading is represented as an elastic response spectrum as explained in Section 3.1. The NPR9998 has developed a webtool in which the seismic loading of a specific area can be determined. From the NPR9998 webtool the Peak Ground Acceleration (PGA) and the soil types, which influence the spectral periods, can be obtained. Subsequently, the simplified smoothed design response spectrum can be obtained with the following equations:

$$0 \leq T \leq T_B \ : \ S_d(T) = a_{gS}[1 + \frac{T}{T_B} \cdot (\eta \cdot p - 1)] \tag{3.2}$$

$$0 \leq T \leq T_C \ : \ S_d(T) = a_{gS} \cdot \eta \cdot p \tag{3.3}$$

$$0 \leq T \leq T_D \ : \ S_d(T) = a_{gS} \cdot \eta \cdot p \cdot \frac{T_C}{T} \tag{3.4}$$

$$T_D \leq 4 \ : \ S_d(T) = a_{gS} \cdot \eta \cdot p \cdot [\frac{T_C \cdot T_D}{T^2}] \tag{3.5}$$

In which η represents the damping correction factor, which may be taken as $\eta = 1$ if the viscous damping is 5%. An example of the elastic response spectrum is given in Figure 3.2.

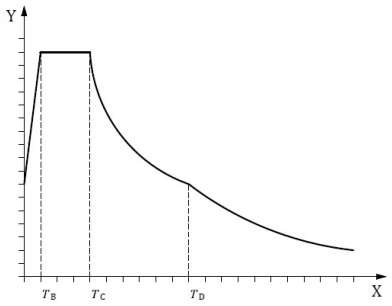

Figure 3.2: Elastic response spectrum.
Source: NPR9998-2018

3.1.2 Near collapse limit state

The global capacity curve is determined by the evaluation of strength hierarchy. In which the NC limit state is the limit such that the load bearing structure is still able to transfer the vertical load. The NC limit state of a structure is defined by the NPR9998 to be exceeded if:

- The total lateral resistance of the structure has been decreased with 50%, due to failure of individual elements.
- Part of the elements exceed the drift limit which results into failure of the structure.
- Dynamic instability is reached which results in failure of the structure.

The global drift limits for the NC limit state as defined by the NPR9998 are presented in Table 3.1.

Table 3.1: Drift limit NC limit NPR9998.

	Inter storey Drift limit	**Drift limit at h_{eff} [1 storey]**	**Drift limit at h_{eff} [2 storeys]**
Brittle response	1.5%	1.5%	0.8%
Ductile response	0.6%	0.6%	0.4%

In the Eurocode 8 different limits are prescribed for the NC limit state. After a strength decrease of 20% the NC limit stated is reached. The drift limit is determined locally and it is defined in the NEN-EN 1998-3 to use the following drift limit for flexural and shear failure in the NC limit state:

$$\theta_{nc;flexure} = \frac{4}{3} \cdot 0.008 \cdot \frac{H_0}{l_w} \tag{3.6}$$

$$\theta_{nc;shear} = \frac{4}{3} \cdot 0.004 \tag{3.7}$$

3.2 TARGET DISPLACEMENT METHOD

For the evaluation of the seismic capacity of a structure the seismic demand is determined at the corresponding target displacement. Several target displacement procedures are developed for the determination and included in guidelines. In the NPR9998 an adapted version of the capacity spectrum method is prescribed. The guideline approves the use of alternative methods which use the coefficient method. In the Eurocode the N2-method is prescribed which is in contradiction with the NPR9998 which strongly recommends to not use the N2-method for URM structures. The two methods will be explained in this chapter.

3.2.1 Capacity spectrum method

The capacity spectrum method is a graphical method where the seismic demand and the capacity of the structure are compared to each other. The graphics of the demand and capacity can be presented in an ADRS format, in which the relation between the spectral acceleration and spectral displacement is presented. Where the capacity and demand spectrum intersect the displacement demand and inelastic acceleration strength can be found, see figure Figure 3.3 (Fajfar, 1999). According to Ćosić (2009), the intersection of the curves shows that the construction will be damaged, but the size of the damage depends upon the non-linear deformations.

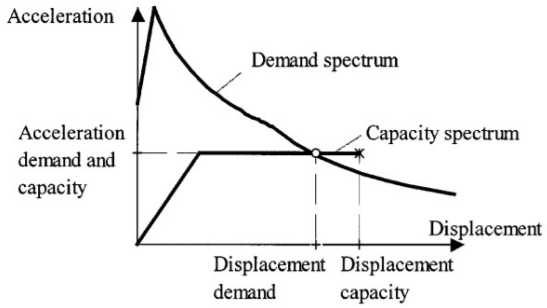

Figure 3.3: Capacity spectrum method.
Source: Fajfar (1999)

The first step of the method is to convert the obtained elastic response spectrum which is presented as a traditional spectrum to an ADRS spectrum. The conversion is visualized in Figure 3.4. The transformation can be realized with the following equation:

$$S_d(T) = S_a(T) \cdot \frac{T^2}{4 \cdot \pi^2} \tag{3.8}$$

In order to obtain a more accurate demand, the elastic spectrum can be reduced with a spectral reduction factor to obtain the inelastic spectrum (Fajfar, 1999). The transformation into the inelastic spectrum is made, assuming that a structure has the capacity to response inelastically.
The spectral reduction factor for URM as prescribed in the NPR9998 takes the energy dissipation and viscous damping of the structure into account. The spectral reduction factor can be expressed with the following formula:

$$\eta_\xi = \sqrt{\frac{7}{2 + \xi_{sys}}} \geq 0.55 \tag{3.9}$$

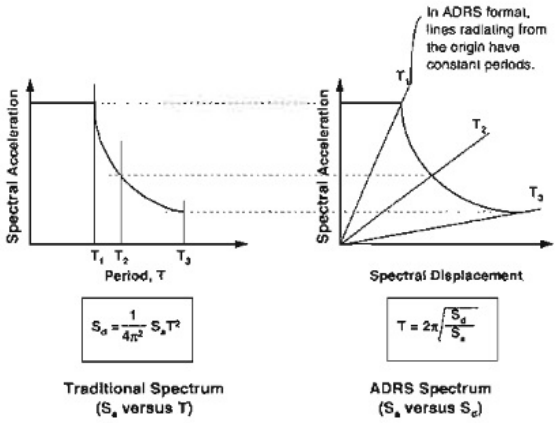

Figure 3.4: Transformation response spectrum to ADRS fomat.
Source: ATC (1996)

In which ξ_{sys} the effective viscous damping of the system presents, which consists of the inherent damping (ξ_0), the hysteretic damping (ξ_{hy}) and the damping due to the foundation (ξ_d). For URM structures the NPR9998 prescribes the inherent damping as 5% and the hysteretic damping depends upon whether the failure mechanism is ductile or not, but with a maximum of 15%. Finally to obtain the non-linear demand the spectral reduction factor is multiplied with the elastic demand.

Secondly the MDoF system is transformed into an equivalent SDoF system as explained in Section 3.1. The pushover curve of the equivalent SDoF is presented in ADRS format in order to compare the curve with the seismic demand. This pushover curve in ADRS format can be obtained by dividing the pushover curve of the SDoF system by the effective mass:

$$S_a = \frac{F*}{m_{eff}} \tag{3.10}$$

In which S_a represents the spectral acceleration of the equivalent SDoF system. However, it should be noted that in order to compare the seismic capacity the bilinearized capacity curve is required. The bilinearized curve is a linear approximation, an example of the curve is given in Figure 3.5. The initial lateral stiffness of the equivalent SDoF system can be determined by calculating the secant stiffness of the base shear force at 60% of the maximum base shear force. The displacement capacity of the system is equal to the displacement capacity in the NC limit state.
The bilinearized capacity curve of the equivalent SDoF system can now be computed by determining the spectral acceleration ($S_{a;y}$) of the SDoF system when it starts to yield. It is assumed that the force displacement relation is elasto-platic with the relevant energy criteria. This can be expressed in the following equation:

$$S_{a;y} = \frac{u_{cap;bilin} \cdot K_{init} - \sqrt{(u_{cap} \cdot K_{init})^2 - 2 \cdot E_m \cdot K_{init}}}{m_{eff}} \tag{3.11}$$

With the determination of the capacity and the demand curve in the ADRS format, the displacement demand of the structure can be determined. This can be done by graphics: at the intersection of the demand spectrum and capacity spectrum. If the capacity and demand spectrum

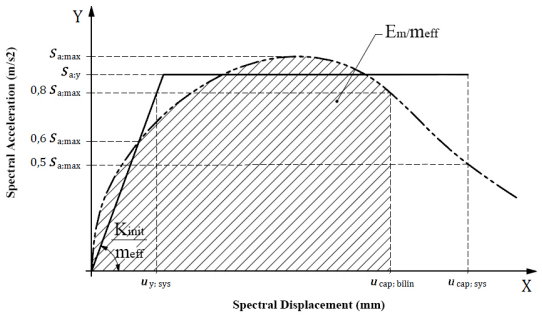

Figure 3.5: Bilinearized capacity curve.
Source: NPR9998-2018

don't intersect, the displacement demand can be determined based upon the effective period of the equivalent SDoF system. The effective period is expressed with the following equation:

$$T_{eff} = 2 \cdot \pi \sqrt{\frac{m_{eff}}{k_{eff}}} \tag{3.12}$$

With k_{eff} as the effective stiffness of the equivalent SDoF system:

$$k_{eff} = \frac{V_{prob}}{u_{cap}} \tag{3.13}$$

By plotting the effective period on the inelastic demand curve the intersection of the both represents the displacement demand of the structure. In Figure 3.6 this assessment is represented.

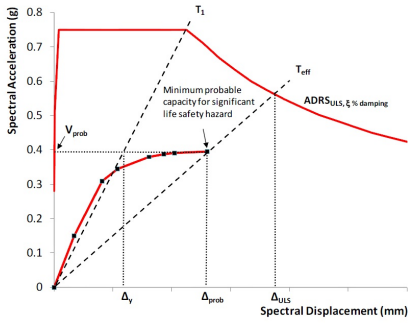

Figure 3.6: Nonlinear capacity curve assessment.
Source: NPR9998-2018

3.2.2 N2- Method

The N2-method is the method which is prescribed in the Eurocode 8 in order to determine the target displacement. The method uses the same format as the capacity spectrum method, the method is also based on the inelastic spectrum. Similar as for the NPR9998 a reduction factor, here the damping correction factor, is taken into account.
The first steps of the method are similar as the capacity spectrum method. The traditional

spectrum is converted to the ADRS spectrum with Equation 3.8. Secondly the MDoF system is converted to its equivalent SDoF system based upon the same transformation factor as described for the capacity spectrum method in Section 3.2.1.
Thirdly, the idealized force displacement relation is required of the equivalent SDoF system. With the procedure the yield force (F_y^*) of the system can be determined, which is equal to the maximum base shear force. In Figure 3.7 the procedure is visualized. The initial stiffness of the structure should be determined so that the area under and above the idealized force displacement curve are equal to each other. Therewith the yield displacement can be determined with the following equation:

$$d_y^* = 2(d_m^* - \frac{E_m^*}{F^*y}) \tag{3.14}$$

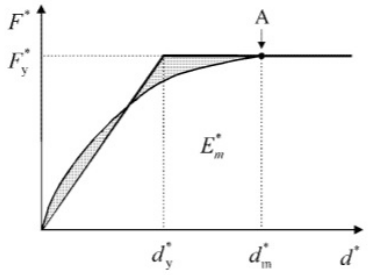

Figure 3.7: Idealized force displacement relation.
Source: Eurocode 8

The period (T^*) of the equivalent SDoF system is expressed with the following equation:

$$T^* = 2\pi\sqrt{\frac{m^* d_y^*}{F_y^*}} \tag{3.15}$$

A distinction is made between structures which have a short or a medium until long period range. Structures with a period $T^* < T_c$ are considered as short period range, else the structure is considered as a medium and long period range. It is taken into account whether the structures response is elastic or nonlinear. In Figure 3.8 the target displacement method is visualized for both the periods. The target displacement (d^*) for the equivalent SDoF system can be determined with the following equations:

1. $T^* < T_c$:
   a) If $F_y^*/m_{eff} > S_a(T^*)$:

$$d^* = d_{et}^* \tag{3.16}$$

   b) If $F_y^*/m_{eff} < S_a(T^*)$:

$$d_t^* = \frac{d_{et}^*}{q_u}(1 + ((q_u) - 1)(\frac{T_c}{T^*}) \leq d_{et}^* \tag{3.17}$$

2. $T^* > T_c$:

$$d_t^* = d_{et}^* \tag{3.18}$$

In which q_u represents the acceleration of the structure which behaves elastic unlimited over a structure which has limited strength. The factor is expressed in the following equation:

$$q_u = \frac{S_e(T^*)m_{eff}}{F_y^*} \tag{3.19}$$

Finally the target displacement of the equivalent SDoF system can be determined. If the target displacement is multiplied with the transformation factor, the target displacement of the corresponding MDoF system can be determined:

$$d_t = \Gamma \cdot d_t^* \tag{3.20}$$

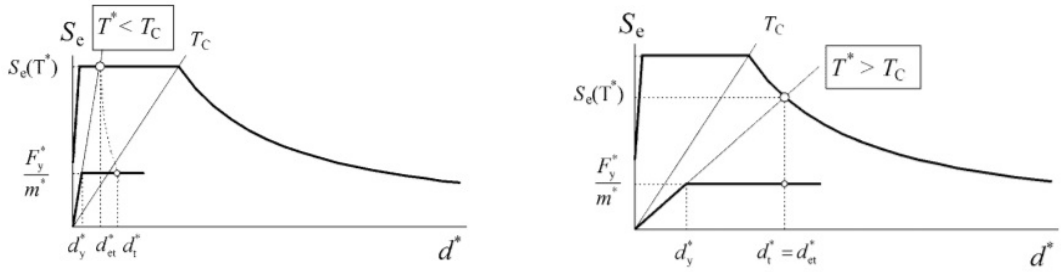

(a) Short period range **(b)** Medium and long period range

Figure 3.8: Target displacement method.
Source: Eurocode 8

3.3 ANALYTICAL MODELING STRATEGY

The analytical modeling strategy: the SLaMA method which will be studied in this thesis is elaborated here. In this section the method will be introduced according to the NPR9998-2018.

3.3.1 Simplified Lateral Mechanism Analysis (SLaMA)

The SLaMA method is a simplified analysis technique which can be used in order to determine the nonlinear pushover curve of a structure. In the method first the individual inelastic mechanisms are analysed. A lateral load is applied on top of a mechanism and increased until the element fails. Subsequently, the global capacity of a structure can be determined by adding the representations of the individual capacities. The global capacity is represented as a pushover curve which shows the relation between the base shear force and the top displacement.

The NZSEE (2017) recommends to use the SLaMA method as a first step in the analysis of a structure subjected to seimsic loading. With the SLaMA method the engineer is able to obtain more insight in the structural behaviour in a relative simple manner. Therewith the method can be used as a starting point before more complex analysis techniques are applied.
The main steps of the SLaMA method are summarized by the NPR9998 as follows:

1. Identify the main structural elements, potential structural weaknesses and severe structural weaknesses.
2. Asses the connection between the floor and the walls and determine whether the floor is able to fulfil its function properly.
3. Assessment of the out-of-plane behaviour.
4. Assessment of the in-plane capacity of the individual elements.
5. Comparison of the individual behavior and the assessment of the hierarchy of strength.
6. Determine the inelastic mechanism of the subsystems, extend the local behavior to global behavior.
7. Determine the probable governing mechanism, calculate the base shear force and the displacement capacity of the system.

The method will be explained more extensive on the basis of an example in the next chapter.

3.3.2 In-plane strength determination by the NPR9998

In Section 2.2.1 the analytical approaches to determine the in-plane capacity, as described in the literature, were introduced. As mentioned in this section three different in-plane failure mechanisms can be distinguished: flexural failure, shear sliding failure and diagonal cracking failure. The equations as prescribed by the NPR9998 are introduced here.

Flexural failure

The maximum resistance of a pier in which flexural failure is governing, is expressed with the following equation:

$$V_{R;f} = F \cdot \frac{l_w}{2H_0} \cdot (1 - 1.15\frac{\sigma_y}{f_{ma;m}}) \tag{3.21}$$

where:

F = Axial load at the critical section of the element [kN]
l_w = Width of the pier [mm]
H_0 = Effective height of the pier [mm]
σ_y = Mean vertical stress over the full section [N/mm^2]
$f_{ma;m}$ = Mean compressive strength of masonry in the vertical direction [N/mm^2]

The maximum rotation is obtained by experiments based upon piers as in Groningen and expressed with the following equation in the NPR9998:

$$\theta_{R;NC;f} = 0.0135(1 - 2.6 \cdot \frac{\sigma_y}{f_{ma;m}})(\frac{h_{ref}}{h})\sqrt{\frac{h}{l_w}} \tag{3.22}$$

where:

h_{ref} = Reference height of the pier, may be taken as 2.4 [m]
h = Height of the pier [m]

Shear failure

As mentioned before two types of shear failure can be distinguished in the literature: diagonal cracking and shear sliding failure. In the NPR9998 it is prescribed that the diagonal cracking failure mechanism can be neglected if the masonry bricks its quality is as specified in the NEN-EN 1996-1-1 section 3.1.1. The maximum strength of piers where shear sliding failure is governing, is determined according to Equation 2.6. Both the frictional and bond resistance are taken into account for the determination of the strength. However, after the cracks develop in the element the bond resistance decreases. After cracking, the force is transferred by means of friction only. The residual strength after cracking can be determined with the following equation:

$$V_{R;s;res} = \mu \cdot \sigma_y \cdot l_w \cdot t_w \tag{3.23}$$

In Figure 3.9 the development of the shear resistance as defined by the NPR9998 is visualized with the maximum drift limits.

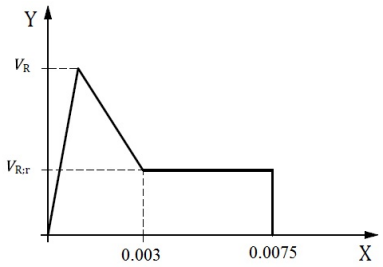

Figure 3.9: Resistance URM pier with shear sliding as governing failure mechanism. With on the y-axis the resistance and on the x-axis the drift limit.
Source: NPR9998-2018

An additional check is prescribed by the NPR9998 where the shear stress in the compressed section is analyzed. The exceeding of the shear stresses can result into splitting of the bricks in the compressed section. The failure mechanism is referred to as the "splitting failure mechanism".

In order to calculate the maximum shear resistance we assume to have a shear strength in the section of:

$$\tau = 0.1 \cdot f_b \tag{3.24}$$

In which f_b is the compressive strength of a brick. In order to calculate the maximum resistance of the pier the effective uncracked length for rectangular cross-sections as expressed in Equation 2.1 is used and substituted into Equation 3.24. The following relation is obtained:

$$V_r = \frac{0.15 \cdot f_b \cdot t_w \cdot l_w}{1 + 0.3(\frac{f_b}{f_a}\frac{H_0}{l_w})} \tag{3.25}$$

where:

t_w = Thickness of the pier [mm]

The drift limit which can be obtained with the failure mechanism is equal to the drift limit of the flexural failure mechanism. The drift limit is as defined in Equation 3.22.

3.4 COMPUTATIONAL MODELING STRATEGY

The computational modeling of masonry structures can be based upon different strategies. In this section firstly an introduction will be given to the different modeling strategies which can be used for masonry structures. Subsequently, the EFM will be discussed more extensive. Finally, the software 3Muri will be introduced in which the EFM is implemented.

3.4.1 Modeling strategies

Masonry is composed out of mortar and bricks with both different mechanical properties as elaborated in Chapter 2. The computational modeling can be complex due to the different material properties and the interaction between the bricks and the mortar. The three main modeling strategies which can be distinguished from the literature for the computational modeling of masonry structures are:

- Micro modeling: detailed modelling strategy in which a distinction is made between the properties of the bricks and the mortar connected by an interface.
- Macro modeling: bricks and mortar are modelled as a homogeneous material.
- Macro-element modeling: a masonry wall is subdivided into a set of macro-elements based upon the level of damage usually observed in these elements.

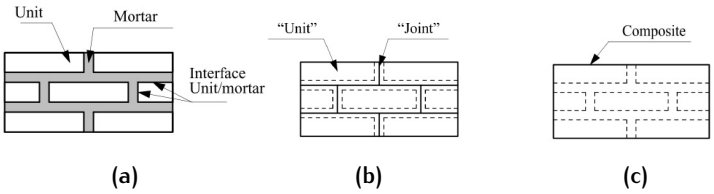

Figure 3.10: Modeling strategies for masonry with: (a) detailed micro-modeling; (b) simplified micro-modeling; (c) macro-modeling.
Source Laurenço et al. (1995)

Micro modeling strategy

In the micro modeling approach a further distinction can be made between detailed and simplified micro modeling. In the detailed micro modeling strategy the bricks and mortar are modelled separately from each other, represented by continuous elements. The elements are connected to each other by the interface, see Figure 3.10a. According to Laurenço et al. (1995) the interface is a representation of the possible crack plane represented as a discontinuous element. For this strategy the properties of both the mortar and the bricks are defined separately.
With the simplified micro-modeling strategy the bricks are extended with half times the thickness of the mortar, see Figure 3.10b. The bricks are connected to each other by the interface which represents the behavior of both the mortar and the interface which connects the bricks and the mortar. With the micro-modeling approach the local failure mechanisms which are typical for masonry can be described, see Figure 3.11. The strategy is applicable to determine the structural behavior of masonry locally. However, due to the large computational effort the use of this strategy is preferred for small structural elements.

Macro modeling strategy

For the macro modelling strategy (Figure 3.10c) no distinction is made between the bricks and the mortar, the material is considered as a an-isotropic material (Laurenço et al., 1995). The behavior

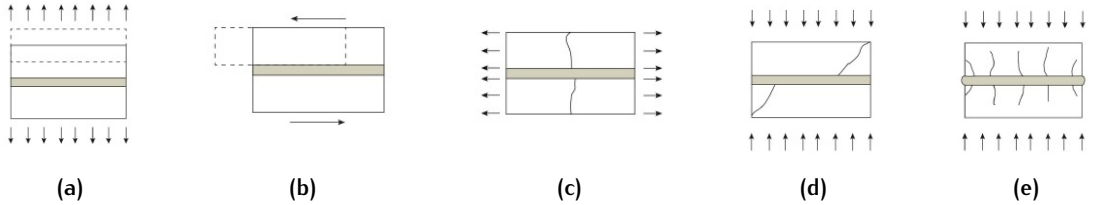

Figure 3.11: Local failure mechanisms: (a) Joint tension cracking; (b) joint slipping; (c) Unit direct tension cracking; (d) Unit diagonal tension cracking; (e) masonry crushing.
Source Laurenço et al. (1995)

of the material is described based upon the average stress and strain relation in which the material properties can be obtained via experiments. Macro-modeling is applicable for masonry structures from which the global behavior is of interest. On the other hand, the strategy is not able to give a detailed result as regards the development of the local failure modes. According to Laurenço et al. (1995) this strategy is particularly applicable for structures with large spanning walls with no openings since the stress distribution is mainly uniform here.

Macro-element modeling strategy

As regards the macro-element modeling strategy the wall is subdivided into a set of macro-elements. The modeling strategy is used in the EFM in which the wall is considered as an idealized frame (Lagomarsino et al., 2013). The method is implemented in the software 3Muri and the further description of the EFM is applicable to the software.
In the method the masonry wall is subdivided into deformable masonry elements which are connected to each other by rigid nodes. The rigid parts are the parts which generally do not experience any damage during an earthquake. In the deformable elements the nonlinear response and deformation is concentrated (Lagomarsino et al., 2013). In Figure 3.12 the schematization of masonry wall into the equivalent frame is visualized. Generally, two type of elements can be distinguished within the deformable elements: the piers and spandrels. Piers are the primary vertical elements, the spandrels are the horizontal elements above openings which connect the piers. The spandrels mainly determine the boundary conditions of the piers, and subsequently the in-plane behavior of the equivalent frame.

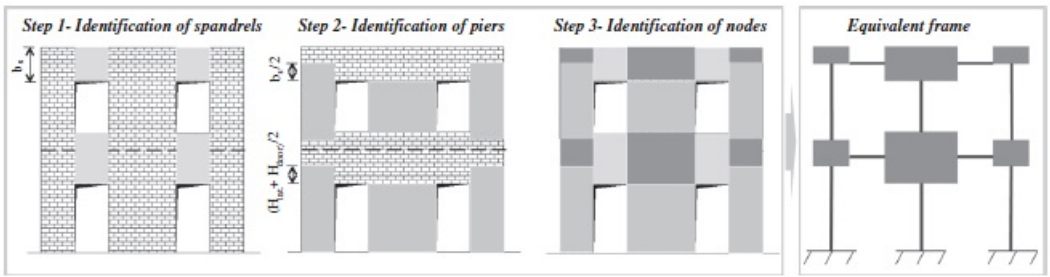

Figure 3.12: Equivalent frame idealization.
Source: Lagomarsino et al. (2013)

3.4.2 Equivalent frame method

The EFM is applicable for the determination of the global behavior of a masonry structure during an earthquake. The capacity of the structure depends upon the in-plane capacity of the elements, it is assumed that the out-of-plane capacity is not governing for the global behavior of the structure. For the determination of the global behavior of the structure a distinction is made between the horizontal and vertical elements within the load bearing structure. The vertical elements (the walls) are the load bearing elements, the horizontal elements, such as the floor, are responsible for the distribution of the lateral loading over the walls. The final assumption which is made in 3Muri, is that the flexural behavior of the horizontal elements is not governing for the global capacity of a structure (Lagomarsino et al., 2013).

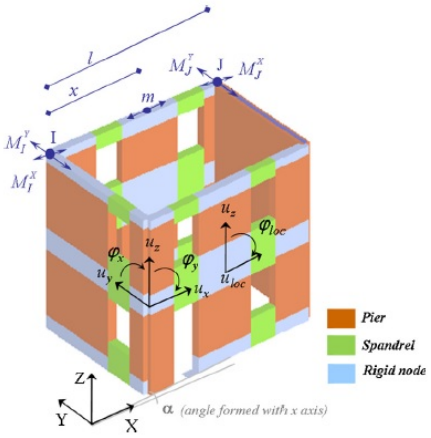

Figure 3.13: Three dimensional model in 3Muri.
Source: Lagomarsino et al. (2013)

In order to create the three dimensional model a global coordinate system (x,y,z) is set, an example is visualized in Figure 3.13. The vertical elements can be determined with the coordinates of one point and the angle which can be made with the global x-axis. With this approach it is possible to model the vertical elements in the local coordinate system as plane frames. Consequently, the intern nodes are two dimensional with three degrees of freedom. The connecting nodes, there where walls meet, are three dimensional with five degrees of freedom (u_x, u_y, u_z, ϕ_x, ϕ_y, ϕ_z). The rotation around the z-axis is neglected in the three dimensional model. The three dimensional nodes are obtained by adding the two two-dimensional rigid nodes of each plane and project the local degrees of freedom along the global axis (Lagomarsino et al., 2013). It is assumed that there is a complete coupling between the intersecting walls.

The global behavior is determined by the capacity of the individual elements. The individual masonry elements (piers and spandrels) are modelled as 2D elements, with three degrees of freedom per node, as visualized in Figure 3.14. As visualized, the loads can only be applied on the nodes and don't work along the element.

The in-plane capacity of the masonry elements is determined by flexural or shear behavior. During the analysis the shear strength in the element varies due to a redistribution of the axial loading in the elements. The element starts to behave non-linear after the strength limit is reached as regards its bending or shear strength. It is assumed that the relation between the shear force and displacement is bi-linear without taken hardening or softening behavior into account, see

Figure 3.14: Macro-element 3Muri.
Source: S.T.A. DATA srl

Figure 3.15. After reaching the strength limit the stiffness in the element decreases further. The stiffness matrix can be expressed as follow Lagomarsino et al. (2013):

$$\begin{Bmatrix} V_i \\ N_i \\ M_i \\ V_j \\ N_j \\ M_j \end{Bmatrix} = \begin{bmatrix} \frac{12EI\eta}{h^3(1+\psi)} & 0 & \frac{-6EI\eta}{h^2(1+\psi)} & \frac{-12EI\eta}{h^3(1+\psi)} & 0 & \frac{-6EI\eta}{h^2(1+\psi)} \\ 0 & \frac{EA}{h} & 0 & 0 & \frac{-EA}{h} & 0 \\ \frac{-12EI\eta}{h^3(1+\psi)} & 0 & \frac{-6EI\eta}{h^2(1+\psi)} & \frac{-12EI\eta}{h^3(1+\psi)} & 0 & \frac{-6EI\eta}{h^2(1+\psi)} \\ 0 & \frac{EA}{h} & 0 & 0 & \frac{-EA}{h} & 0 \\ \frac{-12EI\eta}{h^3(1+\psi)} & 0 & \frac{-6EI\eta}{h^2(1+\psi)} & \frac{-12EI\eta}{h^3(1+\psi)} & 0 & \frac{-6EI\eta}{h^2(1+\psi)} \end{bmatrix} \begin{bmatrix} u_i \\ w_i \\ \phi_i \\ u_j \\ w_j \\ \phi_j \end{bmatrix} \tag{3.26}$$

With:

$$\psi = \frac{1.2El^2}{Gh^2} \tag{3.27}$$

In which η represents the stiffness reduction factor, the factor takes the cracked conditions into account in order to simulate the behavior of an element when it is cracked.
Generally the failure of a masonry element is determined by the maximum drift of the governing failure mechanism, see Figure 3.15. The equations used in 3Muri in order to determine the governing failure mechanism will be elaborated in the next subsection.

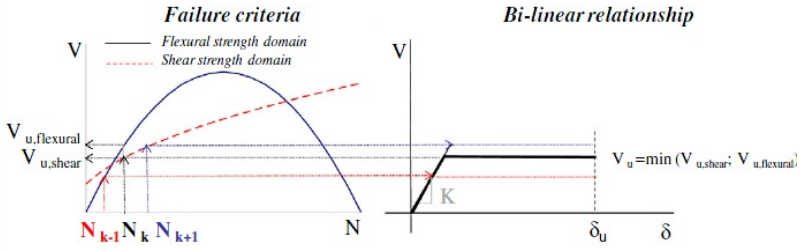

Figure 3.15: Determination failure of the element 3Muri.
Source: Lagomarsino et al. (2013)

3.4.3 Failure modes

As regards the failure mechanisms, the software makes a distinction between shear failure and flexural failure. The governing failure mechanism is dependent upon multiple parameters such as geometry and the boundary conditions. Moreover, the axial loading on top of the element is determinative for the type of failure mechanism. In Figure 3.16 the relation between the axial load in the element and the shear force is given per failure mechanism. The determination of the three failure mechanisms according to the software are elaborated below.

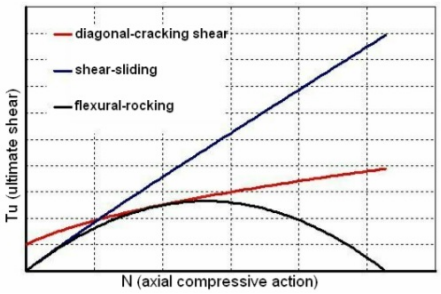

Figure 3.16: Relation shear and axial compressive action.
Source: S.T.A. DATA srl

Bending failure

Bending failure may be associated to the rocking failure mode. The maximum shear force in the element is determined based upon equilibrium as expressed in Equation 2.2. The factor of 0.85 in this equation which relates to the rectangular section is always similar independent of the section.

Shear failure

Within the 3Muri software a choice is required between the Mohr-Coulomb or the Turnsek Cacovic criteria as decisive criteria for shear failure mechanism. 3Muri itself is not able to take both the constitutive laws into account during an analysis, only one of the criteria can be chosen. The Mohr-Coulomb criteria describes the shear sliding failure, this relation is according to S.T.A. DATA srl more suitable for new masonry structures. The Turnsek Cacovic criteria describes diagonal shear failure and is according to S.T.A. DATA srl more suitable for existing masonry structures. The relation between the ultimate shear force in masonry and axial compressive stress is shown in Figure 3.16. For elements with low axial loading the shear sliding mechanism is governing, if the axial load increases the diagonal cracking becomes governing.

The shear failure based upon the Mohr-Coulomb relation is expressed in 3Muri with the following equation S.T.A. DATA srl:

$$V_r = D_{eff} f_{v0} t + \mu N \tag{3.28}$$

A limit is given to D_{eff} which is the effective uncracked length of the section and is determined similar as expressed in Equation 2.1. The limit of the shear strength is expressed as S.T.A. DATA srl:

$$V_{lim} = f_{v,lim} D_{eff} t \tag{3.29}$$

In which $f_{v,lim}$ is defined as in the Eurocode 8 as $0.065 f_b$. The shear strength limit is finally determined by 3Muri as the minimum value of $V_{v,lim}$ and V_r.
The Turnsek Cacovic criteria gives a shear limitation defined with the following equation:

$$V_{Rd,s} = lt \frac{1.5\tau_0}{b} \sqrt{1 + \frac{N_{Ed}}{1.5\tau_0 lt}} \tag{3.30}$$

In which b represents a shape factor: b = h/l, but $1 \leq b \leq 1.5$.

4 BUILDING TYPOLOGIES IN GRONINGEN

In this chapter the building stock of Groningen will be presented based upon the data base which is created by ARUP & NAM (2018). More attention will be on the typology which will be analyzed more extensive during this thesis: the unit typology.

4.1 DATABASE GRONINGEN

In order to determine the seismic risk, the governing failure mechanism needs to be determined for a structure. The critical load paths can be determined and therewith the vulnerabilities of a structure. For the determination of the seismic risk in Groningen the building stock is required. ARUP & NAM (2018) have made a database where the building stock of Groningen is presented and sorted into groups based upon similarities within the geometrical and structural layout and structure materials. Buildings with similarities within this category are a typology. It is expected that buildings within a typology show similarities in their structural performance and governing failure mechanism.
The total building stock is first divided into five categories based upon geometric parameters. A further sub-division is made within the category based upon structural layout and finally a sub-division is made based upon the structural system. Further explanation per category will be given in the following subsections.

4.1.1 Geometric classification

Firstly the total building stock of the database of ARUP & NAM (2018) is classified based upon geometric parameters. Three geometric parameters are used here:

1. The maximum length of a enclosed rectangle
2. The maximum width of a enclosed rectangle
3. The gutter height

The building stock is classified into into five different categories based upon the geometric parameters:

1. Shed: small sized building (32%)
2. Unit: medium sized building (60%)
3. Block: repetition horizontally or vertically of the units (2%)
4. Barn: Buildings with a large span (6%)
5. Tower: tall buildings (0.2%)

The percentages present the percentage contribution of the typology in the building stock. In Figure 4.1 the classification maps for the above mentioned categories are visualized. When

approaching the boundary between different areas, the reliability of a correct classification decreases (ARUP & NAM, 2018). As explained in the Chapter 1, this thesis will focus on the terraced houses. This is also known as the unit typology. Therefore the focus of the rest of the chapter will be on the unit structures.

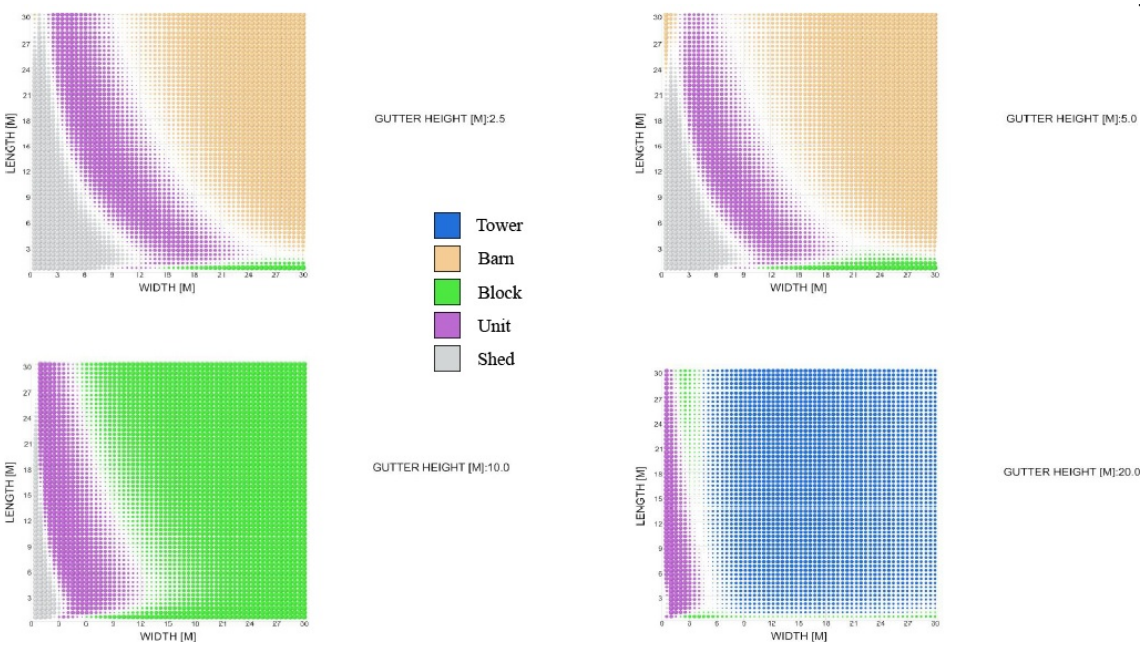

Figure 4.1: Geometry classification map.
Source: ARUP & NAM (2018)

4.1.2 Structural classification

With the structural classification a further subdivision is made within the classification type: unit. The parameters which are used for the sorting of the unit structure are:

1. Adjacency, is the building part of a homogeneous or in-homogeneous block or is the building free standing.
2. What is the amount of addresses in the block, more than one or only one.

After the further subdivision within the unit structures, a distinction is made which results in the following five groups:

1. House: freestanding building, small span.
2. House complex: freestanding building, multiple small spans
3. Block unit single: multiple buildings creating one homogeneous block, one single address.
4. Block unit multiple: multiple buildings creating one homogeneous block, multiple addresses.
5. Aggregated unit: multiple buildings creating one in homogeneous block.

In Figure 4.2 the distribution of the structural layout is visualized within the classification of the typology unit.

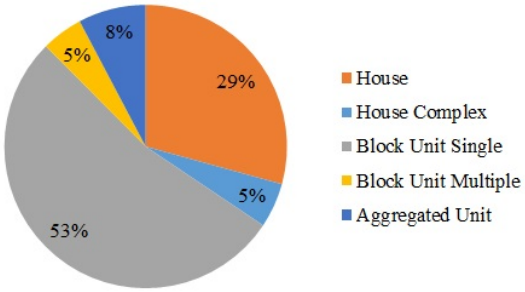

Figure 4.2: Distribution structural layout.

4.1.3 Structural system

For the last classification step a combination of inspections and available data is used to classify the buildings into a structural system and finally in their typology. The parameters which are used are:

1. Structural material of the walls; calcium silicate (CS), clay brick (CB) or concrete (CO)
2. Are there cavity walls; yes (CW) or no (NCW)
3. The floor type; concrete (CF) or timber (TF)

The classification of the building stock into different typologies is done by ARUP & NAM (2018) through a classification algorithm. A learning set was created by adding 376 reference buildings into a database. Based upon the learning set a foundation was created for the classification algorithm. According to ARUP & NAM (2018) 16977 buildings from the database have been checked if they matched their classification class. 86% of this group was correctly classified into the geometric classes and 79% was correctly placed into the structural class by the classification algorithm.

5 VERIFICATION OF THE SEISMIC ANALYSIS METHODS

In this chapter the seismic analysis methods will be introduced by applying these to a case study. The concerning case study represents a typical but idealized Dutch terraced house which was built at the laboratory at the TU Delft. The seismic behavior of the structure was studied in the lab by means of cyclic pushover tests.
Firstly, the case study's characteristics will be described and secondly the SLaMA method will be applied in order to determine the seismic behavior of the structure. The SLaMA method is applied according to the NPR9998-2018. Finally, the case study will be modelled with 3Muri version 12.2.1.4. The results obtained with both SLaMA and 3Muri will be compared to each other.

5.1 CASE-STUDY DESCRIPTION

The case study is a two storey structure constructed with Calcium Silicate (CS) bricks and concrete floors. Only the load-bearing part of the house was constructed in the laboratory, in other words only the inner leaf was built. The structure represents the URM terraced houses which were built in Groningen in the period 1960-1980. Typical for these terraced houses are large openings in combination with slender piers. In Figure 5.1 the structure is visualized. The main characteristics of the structure as constructed in the laboratory are according to Esposito et al. (2018):

- To prevent the structure from any sliding, the first layer of bricks is glued onto the foundation beams.
- The prefabricated concrete slabs consists of two parts, which are connected to each other with cast-in-place reinforced concrete dowels, in order to try to obtain similar behavior as a monolithic floor.
- At the first floor level the piers are connected to the floor with horizontal anchors, three anchors per narrow pier and five anchors per wide pier. The anchors are not able to transfer any vertical loading and are intended to prevent buckling of the pier. The floor spans between the transverse walls
- The second floor is set upon the transverse walls and indirectly the piers.
- The piers and transverse walls are connected to each other with a running bond, causing interlocking between the transverse wall and the piers.

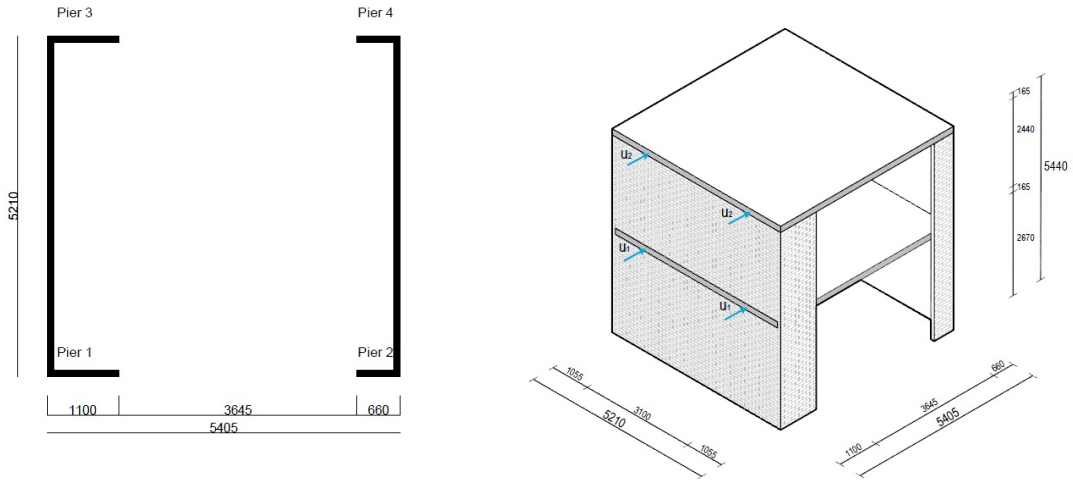

(a) Floorplan **(b)** 3D view building

Figure 5.1: Plan simple case study.
Source: de Groot (2019)

Table 5.1: Material properties case study.
Source: Esposito et al. (2018)

Symbol	Material property	Value
E	Elastic modulus perpendicular to the bed joints	3339 N/mm^2
E_h	Elastic modulus parallel to the bed joints	2081 N/mm^2
G	Shear modulus	2500 N/mm^2
f_m	Compressive strength mortar	7.27 N/mm^2
f_b	Compressive strength masonry unit	13.26 N/mm^2
f'_m	Compressive strength masonry perpendicular to the bed joints	6.01 N/mm^2
$f'_{m,h}$	Compressive strength masonry parallel to the bed joints	7.55 N/mm^2
$f_{x,1}$	Out-of-plane masonry flexural strength parallel to the bed joints	0.21 N/mm^2
$f_{x,2}$	Out-of-plane masonry flexural strength perpendicular to the bed joints	0.76 N/mm^2
f_{v0}	Initial shear strength of the masonry	0.12 N/mm^2
μ	Shear friction coefficient masonry	0.49
f_{vo}	Initial shear strength masonry-concrete	0.09 N/mm^2

As has been mentioned a quasi-static cyclic pushover test has been performed. The test setup and the obtained results of the experiment are presented in Figure 5.2. Two actuators per floor level were applied, the actuators were coupled in order to impose a ratio of 1:1 between the applied forces per floor level. In total 21 cycles have been applied, each cycle consists of 3 identical runs. A run has been defined by Esposito et al. (2018) as the time which is required to reach the maximum positive and negative displacement which starts and ends at zero.

According to Esposito et al. (2018) the first cracks in the structure developed at the joint between the concrete floor and transverse walls. Thereafter, diagonal cracks developed in pier 1 and 3 at the ground floor. During this phase the rest of the construction was nearly not damaged. The development of the cracks is visualized in Figure 5.3. With the further development of the cracks in all the piers, the cross-sectional area reduced and therewith the capacity. Finally, failure was governed by the flexural damage of mainly the wider piers at the ground floor.

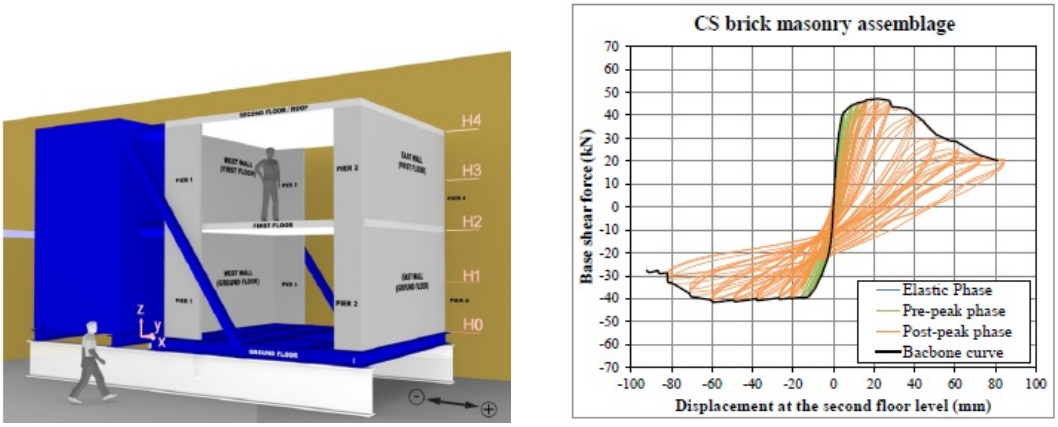

(a) Test set-up **(b)** Capacity curve

Figure 5.2: Experimental information.
Source: Esposito et al. (2018)

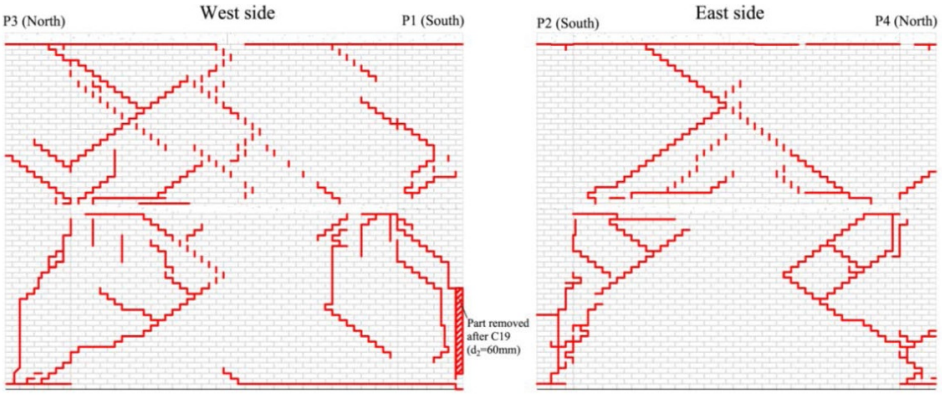

Figure 5.3: Final crack pattern.
Source: Esposito et al. (2018)

5.2 SLAMA METHOD APPLIED

The SLaMA method will now be applied to the case-study as described above. All the steps, as defined by the NPR9998 in Chapter 3, will be applied and the results obtained with the SLaMA method will be compared to the capacity of the structure tested in the lab.

5.2.1 Identifying the main structural elements, potential structural weaknesses and severe structural weaknesses

In Section 5.1 the structural elements are identified and the main features of the case study are summarized. Furthermore, the case study consists out of primary seismic elements only since only the load bearing part of the structure was built. With the relative simple structure and the extensive introduction of the case study, no more attention is given to the first step of SLaMA.

5.2.2 Assessing the connection between the floor and the walls and determine whether the floor is able to fulfil its function properly

For the capacity of the primary lateral load system, the diaphragm working should be considered. In other words, the connection between the floor and the walls should be assessed. Is the floor able to redistribute the loads and transfer these to the load bearing elements.
The floors in this construction are prefabricated concrete slabs which consist of two separate elements. The two floor elements are connected to each other by cast-in-place reinforced concrete dowels with as main goal to create a monolithic floor (Esposito et al., 2018). The diaphragm can be considered as relative stiff, hence its able to redistribute the lateral loads.

First floor level

In Figure 5.4 the connections of the first floor level are visualized. The connection between the pier and the floor (Figure 5.4a) is ensured by anchors. The anchors are masoned in the pier and cast locally in the floor (Esposito et al., 2018). Pier 2 and 4 are connected with three anchors and pier 1 and 3 are connected with five anchors to the concrete floor (Figure 5.1a). As mentioned before, these anchors are not able to transfer vertical load. Only horizontal load can be transferred through these anchors. Buckling is here thus prevented by the anchors. The floor is directly laid upon the transverse wall (Figure 5.4b), a mortar joint connects the concrete floor and the masonry wall. This connection can be considered as relative stiff.
From these details it can be concluded that the floor is supported by the transverse walls.

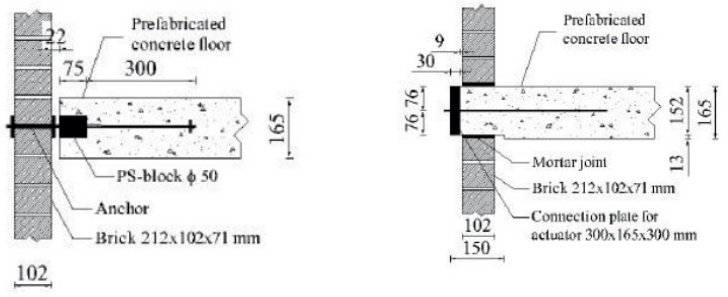

(a) Connection floor, pier **(b)** Connection floor, transverse wall

Figure 5.4: Construction details first floor level.
Source: Esposito et al. (2017)

Second floor level

In Figure 5.5 it is visualized how the second floor level is connected to the pier and transverse wall. Firstly, the floor is set upon the mortar bed joint at the transverse wall. Afterwards, the horizontal joint between the floor and the pier is filled with mortar (Esposito et al., 2018). As a consequence the floor weight is mainly supported by the transverse walls.

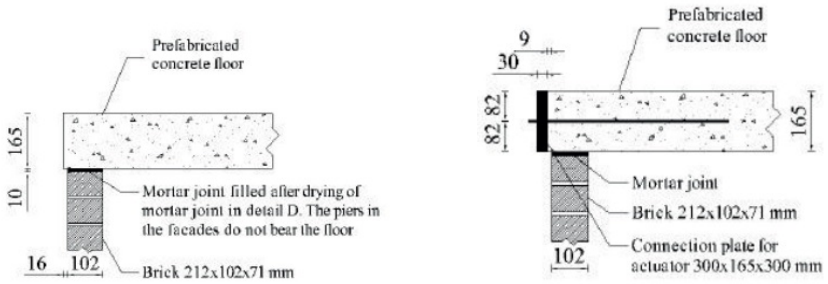

(a) Connection floor, facade **(b)** Connection floor, pier

Figure 5.5: Construction details second floor level.
Source: Esposito et al. (2017)

The shear strength of the mortar connection for the second floor can be determined based upon the Mohr-Coulomb relation:

$$f_{v,lim} = f_{v0,cm} + \mu\sigma_y \tag{5.1}$$

In which $f_{v0,cm}$ is the initial shear strength of the bed joint between the concrete floor and the masonry bricks and μ is the shear friction coefficient in the connection. With the relative low initial shear strength and the low load applied on top of the floor, namely zero, it is assumed that this connection cracks quite early if subjected to seismic loading. Consequently, the floor load is redistributed. It is assumed that part of the floor load is also transferred to the piers now.

5.2.3 Assessment of the out-of-plane behaviour

In this step the out-of-plane capacity of the individual elements is determined according to annex H from the NPR9998. The part of the structure which is loaded out-of-plane can be split into two elements due to the concrete floor which separates the wall. In Figure 5.6 the division in the two elements is visualized.
In the NPR9998 a unity check is advised for URM subjected to seismic loading out-of-plane. The seismic resistance of the element (R_d) ic compared to the seismic load ($S_{a;d}$):

$$E_d = S_{a;d} \leq R_d \tag{5.2}$$

with

$$S_{a;d} = a_{g;d} \cdot \frac{1}{q_a} \cdot \left(\frac{3(1+\frac{Z}{H})}{1+(1-\frac{T_a}{T_1})^2} - \frac{1}{2}\right) \geq a_{g;d} \cdot \frac{1}{q_a} \tag{5.3}$$

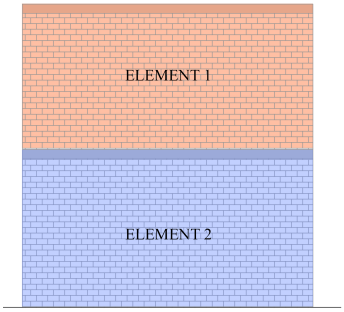

Figure 5.6: Schematization of the transverse wall which is loaded out-of-plane. Two elements can be distinguished.

$a_{g;d}$ = The PGA [g]
q_a = the element factor
Z = the distance between the center of gravity of the element and ground level [m]
H = Height of the building [m]
h = Height of the wall [m]
T_a = the fundamental period of the wall [s]
T_1 = the fundamental period of the wall in the relevant direction based upon the secant stiffness [s]

It is assumed that this case study is located in Loppersum. With the NPR9998 webtool the PGA can be determined for a specific location in Groningen. In Figure 5.7 the corresponding response spectrum for Loppersum is visualized. The out-of-plane capacity and resistance for the elements is visualized in Table 5.2

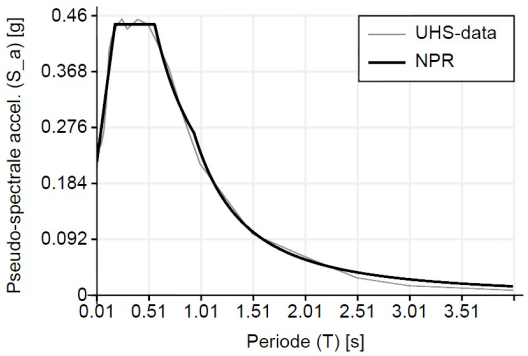

Figure 5.7: Respons spectrum.
Source: NPR9998 webtool

Table 5.2: Out-of-plane capacity inner leaf.

Element	$S_{a;d}$ [g]	R_d [g]
1	0.1037	>1
2	0.310	0.15

In contrast to the expectations, element 2 its seismic resistance is smaller than element 1. According to the NZSEE (2017) the out-of-plane capacity is generally higher at the ground level of the building due to the vertical load which is generally higher at this point. Additionally it can

be derived from the NZSEE (2017) that with a increase of the vertical load with respect to the own weight of the element the basic performance ratio increase, this is the case for element 2. The development of the out-of-plane capacity in the NZSEE (2017) is in contrast to the NPR9998. That being the case and the fact that the transverse walls didn't fail out-of-plane during the experiment, it is assumed that the out-of-plane failure is not governing and not correctly defined in the NPR9998.

5.2.4 Assessment of the in-plane capacity of the individual elements

For the in-plane assessment, the capacity of the individual elements loaded in-plane is required. In this case study the in-plane assessment is only relevant for the piers since there are no spandrels present in the structure. All the failure mechanisms will be calculated in order to determine the governing failure mechanism per element. The determination of the capacity of the different failure mechanisms is elaborated in Section 3.3.2.

Due to the interlocking effect of the bricks between the transverse wall and the pier, it is assumed that the flange is activated. The activation of the flange has a positive influence on the in-plane capacity of the pier. The activation of the flange is taken into account if the axial load is distributed to the pier. However, the location of the flange is of importance with respect to the drift limit of the loaded wall. The flange has a negative effect on the failure mechanism when its in tension. In this case the flange produces extra weight to the mechanism and the stress is increased at the compressed toe. On the other hand, when the flange is in compression, the stress at the compressed corner decreases (Yi et al., 2008). In short, the additional overburden from the flange can increase the stress at the compressed corner and therewith failure of the element occurs in an earlier stage, less high drift limits can be obtained.
According to Russell and Ingham (2010) the flange has a positive effect on the lateral strength capacity of the flexural and sliding mechanisms, but almost no influence on the diagonal cracking failure mode. However, the flange does has a positive effect on the maximum lateral displacement if the diagonal cracking failure mode is governing.
Based upon the experiments by Russell and Ingham (2010) for the calculation of in-plane capacity of the elements, the effect of the flange will be taken into account for the flexural and shear sliding failure modes. For the diagonal cracking failure mode the effect of the flange will be neglected.

The NPR9096-1-1 section 5.5.3 is used as guideline for the determination of the flange weight, see Figure 5.8. The length of the flange generally consists of six times the flange thickness of the transverse wall plus the adjacent area, determined as visualized in Figure 5.8. In the figure also the load schematization of the piers is visualized for the positive and negative direction. It is assumed that the total weight of the second floor level is equally distributed to the piers. For the first floor level the floor is transferred to the pier by the flange and is thus only taken into account when the flange is activated.

An overview of the resistance per element per failure mechanism is given is Table 5.3, the governing failure mechanism for all the piers is the flexural failure mechanism.

Table 5.3: The resistance per element per failure mechanism (kN).

Element	Dir.	Sliding	Splitting	Flexural	Diagonal tension
Pier 1/3	+	45.8	31.9	15.5	29.7
	-	20.5	14.3	7.6	29.7
Pier 2/4	+	18.1	12.6	3.9	25
	-	43.4	30.3	7.9	25

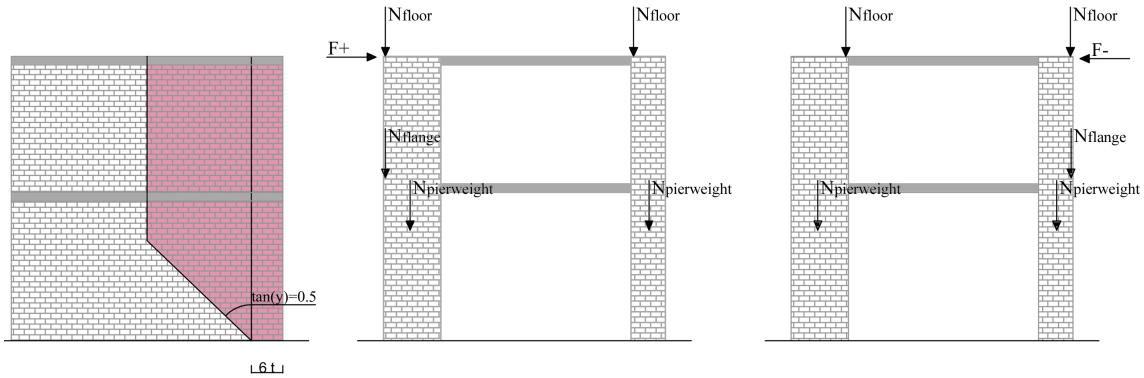

Figure 5.8: Schematization of the loads.

The capacity of each element can be presented in a pushover curve. The pushover curve is characterized by two points, first the curve is linear until the element starts to yield. The yielding point of the structure is determined with forget-me-nots in which the elastic modulus is multiplied with a factor 0.5 in order to take the strength decrease into account. Two types of boundary conditions can be distinguished; cantilever-fixed or fixed-fixed. For the calculation of the maximum displacement at the top of a fixed-fixed pier, the displacement can be calculated halfway the height. By doubling this displacement, the displacement at the top of the pier can be obtained (Petry and Beyer, 2014).

For this case study the pier element is supported halfway and clamped at the top and bottom. The element will be split into two separate parts, for each part the displacement will be calculated. Thus for the pier spanning between ground floor and the first floor level and for the pier spanning between the first and second floor level. This can be expressed with the following equation:

$$u_{top} = \frac{F \cdot l_1^3}{3EI} + \frac{F \cdot l_2^3}{3EI} \tag{5.4}$$

The applied load (F) in the equation is taken as the governing loading per element obtained in Table 5.3. The loading is assumed to be equal at both l_1 as l_2. The ultimate displacement for the flexural failure mechanism is expressed with Equation 3.22. The pushover curve of the individual elements can be determined, the curve is visualized in Figure 5.9

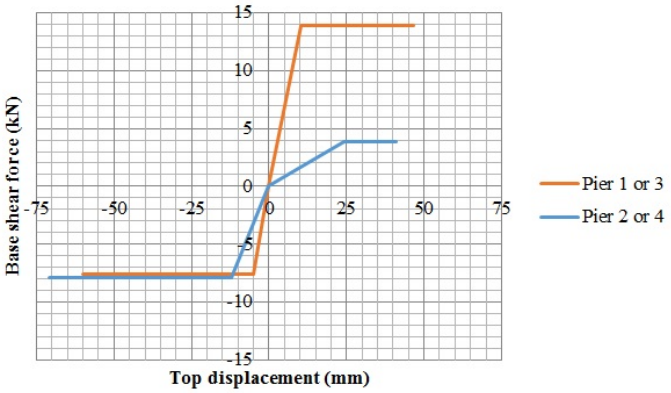

Figure 5.9: Pushover curve of the individual elements obtained with the SLaMA method.

5.2.5 Comparison of the individual behavior of the elements and the assessment of the hierarchy of strength

In this step the capacity of the elements is compared to each order in order to determine the hierarchy of strength per mechanism. By comparing the various sub-systems the governing failure mechanism can be determined. For an URM structure, the capacity of the spandrels and piers are compared to each other in order to determine the governing failure mechanism. However, this step is not relevant for this case study due to the composition of the structure.

5.2.6 Determining the inelastic mechanism of the subsystems, extending the local behavior to global behavior

The governing mechanisms have been identified and therewith the global inelastic mechanism can be determined. In the NPR9998 limits are defined for NC limit state, the limits are defined in Section 3.3.2. It must be noted that the structure is determined here as a structure with one floor level, for the reason that the piers span between the ground and second floor level.
For the global capacity of the case study the base shear force consists of the capacity of pier 1/3 and pier 2/4 and can be doubled due to symmetry. The global pushover curve is shown in Figure 5.10. In the positive direction the drift limit of pier 2/4 is relative low which causes a strength decrease at 40.8 mm. The strength decrease limit of 50% is not reached here. Finally a displacement of 46.5 mm can thus be achieved in the positive direction. In the negative direction pier 1/3 its drift limit is lower than pier 2/4 its drift limit. Similar as in the positive direction, the strength decrease of 50% is not reached after failure of pier 1/3. Finally, a maximum displacement of 70.7 mm is achieved. The NC limit state is reached after failure of both the piers 1/3 and 2/4 in both the positive and negative direction.
The results obtained with the SLaMA method deviate 24.4% with respect to the experiment as regards the base shear force into the positive direction. Into the negative direction the base shear force deviates 22.5% with respect to the experiment. The displacement capacity into the positive direction, taken the 50% strength decrease of the experiment into account, deviates 35.4% with respect to the experiment. The displacement capacity deviates 23.8% into the negative direction from the experiment.

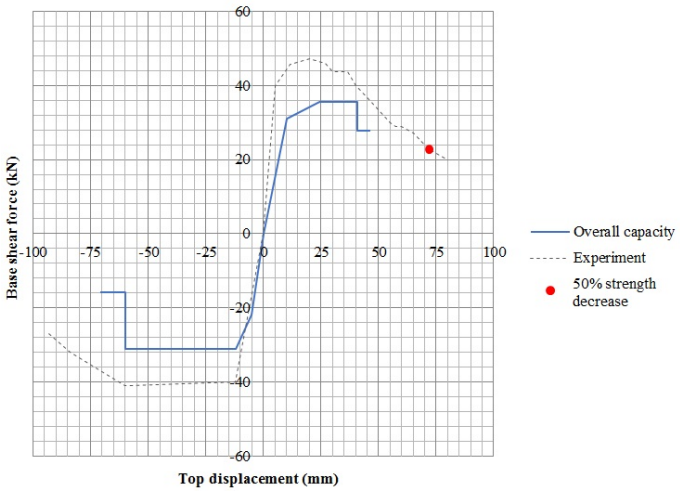

Figure 5.10: Global pushover curve of the experimental case study obtained with the SLaMA method.

5.2.7 Determining the probable governing mechanism, calculating the base shear force and the displacement capacity of the system

Finally, the seismic capacity of the system needs to be determined and compared to the seismic demand according to the spectral displacement method. By converting the structures capacity to it's equivalent SDoF system, the structural capacity can be compared to the seismic demand. In order to convert the structure, the transformation factor is required. According to the NPR9998 the transformation factor may be assumed to be 1 for buildings with a maximum of two storeys. The negative direction is the weakest direction and thus determines the lateral capacity of the system. The seismic elastic demand can be obtained with the values from the NPR9998 webtool, an overview of the parameters is given in Table 5.4.

Table 5.4: Parameters elastic response spectrum.
Source: NPR9998 webtool

$a_{g;S}$	p	T_B	T_C	T_D
0.207 g	2.153	0.183	0.564 s	0.941 s

After the determination of the seismic elastic demand the inelastic seismic demand can be obtained. By converting the elastic seismic demand with the spectral reduction factor. The effective viscous system of the system is:

$$\xi_{sys} = 5 + 15 = 20 \tag{5.5}$$

The spectral reduction factor is:

$$\eta_\xi = \sqrt{\frac{7}{2+20}} = 0.564 \tag{5.6}$$

The inelastic seismic demand spectrum can be obtained and is shown in Figure 5.11. With the intersection of the demand spectrum and the global capacity of the SDoF system, the displacement demand and the inelastic acceleration can be obtained. It can be concluded that the structures capacity is larger than the seismic demand.

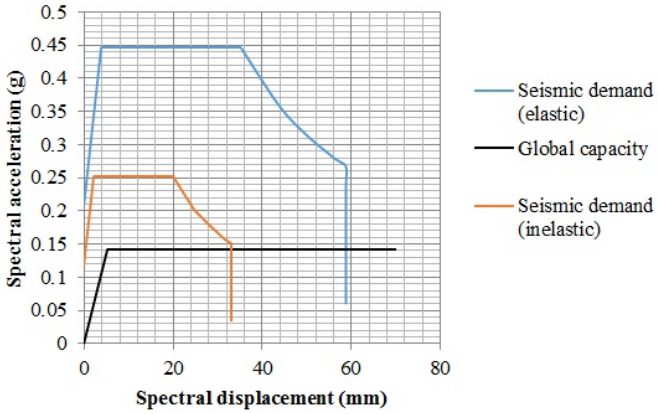

Figure 5.11: Spectral displacement method.

5.3 USE OF THE NZSEE GUIDELINE

In this section the in-plane capacity of the elements is determined according to the NZSEE (2017) guideline as a comparison. In the NZSEE (2017) a distinction is made between the following in-plane mechanisms: rocking, toe-crushing, diagonal tensile failure and shear sliding. In the NPR9998 rocking and toe-crushing are both grouped into the flexural failure mechanism. According to the NZSEE (2017) two types of toe crushing can be distinguished, toe crushing after rocking and toe crushing of the element before any other failure mechanism has occurred. Toe crushing after the rocking mechanism is accompanied with relative large rotations and lower shear forces. In Figure 5.12 the generalized relation between the force and the deformation for rocking piers is visualized.

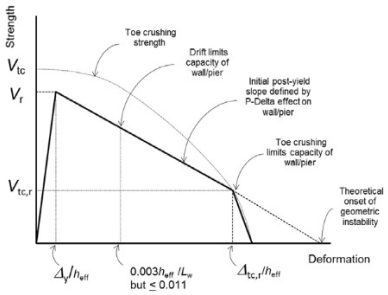

Figure 5.12: Relation between the force-deformation for rocking piers.
Source: NZSEE (2017)

For the determination of the resistance per element, the flange and floor activation is similar as explained in Figure 5.8. In Table 5.5 the in-plane capacity per failure mode is presented.

Table 5.5: The resistance per element per failure mechanism, according to the NZSEE guideline (kN)

Element	Dir	Sliding	Rocking	Toe crushing	Diagonal tension
Pier 1/3	+	56.8	15.4	13.9	29.7
	-	38.9	6.4	6.3	29.7
Pier 2/4	+	28.1	3.6	3.5	25
	-	44.6	9	7	25

The governing failure mechanism is toe crushing for all the elements. For the determination of the global pushover curve the yielding and ultimate displacement is required. The yielding displacement is determined by the NZSEE (2017) as the sum of the flexural and shear displacements of the element. The determination of the yielding displacement may thus be assumed to be similar for each failure mechanism. The following equation is used for the determination of the yielding displacement (Petry and Beyer, 2014).

$$\triangle_y = \frac{5VH}{6G_mA} + \frac{V_rH^3}{2E_mI}(\alpha - \frac{1}{3}) \tag{5.7}$$

In which α is the ratio between H_0 over H_{pier}. According to the NZSEE (2017) in the modulus of elasticity and the shear modulus the cracking should be taken into account. The recommended values are respectively defined as:

$$E_m = 300 \cdot f'_m \qquad G_m = 0.4 \cdot E_m$$

The ultimate rotation for toe crushing is determined according to Priestley et al. (2007), in which the ultimate strain of the compressed fibre is used as a limit. In the NZSEE (2017) the limiting strain is set as 0.0035 at the compressed toe. The limiting angle is expressed as:

$$\theta = \frac{\epsilon_m}{c}\left(\frac{l_p - c}{2}\right) \tag{5.8}$$

In which c is the compression depth, it is assumed that this is 20% of the wall width (Priestley et al., 2007). The global pushover curve can be obtained and is visualized in Figure 5.13.

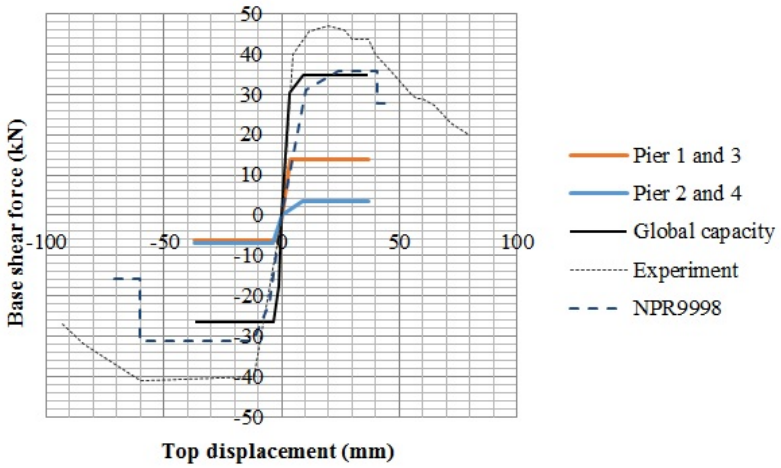

Figure 5.13: Global pushover curve according to the NZSEE as guideline.

The main difference with the structural behavior as estimated with the NPR9998 is the ultimate displacement. The maximum base shear force deviates only 2.2% into the positive direction and only 14.2% into the negative direction with respect to the results obtained with the NPR9998. The obtained ultimate displacement deviates 47.8% in the negative direction and 25.8% in the positive direction with respect to the results obtained with the NPR9998. This is related to the different failure mechanisms which are considered in both the NPR9998 and the NZSEE (2017). Additionally, the limiting angle is quite conservative for the toe crushing mechanism in the NZSEE (2017), it is now assumed to have a compression depth of 20% based upon Priestley et al. (2007).

5.4 EQUIVALENT FRAME METHOD

In this section the case study will be modeled with 3Muri. It is not possible to model the exact design of the case study in 3Muri, therefore two models will be created and analyzed. Subsequently, a sensitivity analysis is performed in order to obtain the model which gives the most accurate results which are comparable to the experiment. The used guideline in 3Muri is the Eurocode 8 since this guideline is better developed in the program than the NPR9998-2018. The results obtained with the NPR9998-2018 were not realistic, the piers remained undamaged during the analysis. Still the seismic capacity was lower than the seismic demand. Therefore, no further attention will be given to the NPR9998-2018 as guideline. The following results are obtained with version 12.2.1.4 of 3Muri.

5.4.1 Modelling process

For the modeling in 3Muri first the geometry of the structure is required. Afterwards the program generates a mesh from the defined walls, these walls consist of the macro-elements: piers, spandrels and rigid portions.
The program does not include the floor in the equivalent frame and since there are no spandrels in this specific model, a connection between the piers is required at the first and second floor level. Additionally, it is not possible in 3Muri to model single masonry walls which span from the ground floor until the second floor level. The program divides the piers into two separate piers spanning between the ground floor and the first floor, and the first floor and second floor.

The thickness of the masonry is 100 mm and the base of the model is fixed. The floors in the case study are modelled as a rigid floor spanning between the transverse walls with a thickness of 165 mm. The material properties are similar as the experiment, see Table 5.1. Additionally, the drift limit of the material is required, which is determined according to the EC 8 for the NC limit state. The drift limit is 0.53% if shear failure is governing and 1.07% if flexural failure is governing. Global failure of the structure is reached after a strength decay of 20%.
For the loading of the model, only the own weight of all the elements is taken into account. Thus only the dead load of the floor (G_k) is taken into account which has a load of: 3.96 kN/m^2, the variable load (Q_k) is here zero.

As explained in Section 3.4.3, software is not able to take both the shear criteria into account, and thus a choice is required between the Mohr-Coulomb and the Turnsek Cacovic criteria. Since the load on top of the piers is relative low, it can be assumed that the shear-sliding mechanism prevails over the diagonal cracking mechanism (NZSEE, 2017). Additionally, the Turnsek Cacovic criteria is according to Calderini et al. (2009) more applicable for materials which are homogeneous and isotropic. These features are more applicable to materials which have an irregular texture. Hence, the Mohr-Coulomb relation will be used for the further analysis.

In the following sections different options will be discussed to simulate the structure. As a starting point it is chosen to model the openings and vary the properties of the connecting element. Two main models will be created with two different connection options. In Figure 5.14 the schematization of the elements in 3Muri is visualized. Hereafter will be referred to this schematization.
The analysis results which are obtained from 3Muri use the legend as visualized in Figure 5.15. During this section the failure mechanism will be described as visualized in this legend.

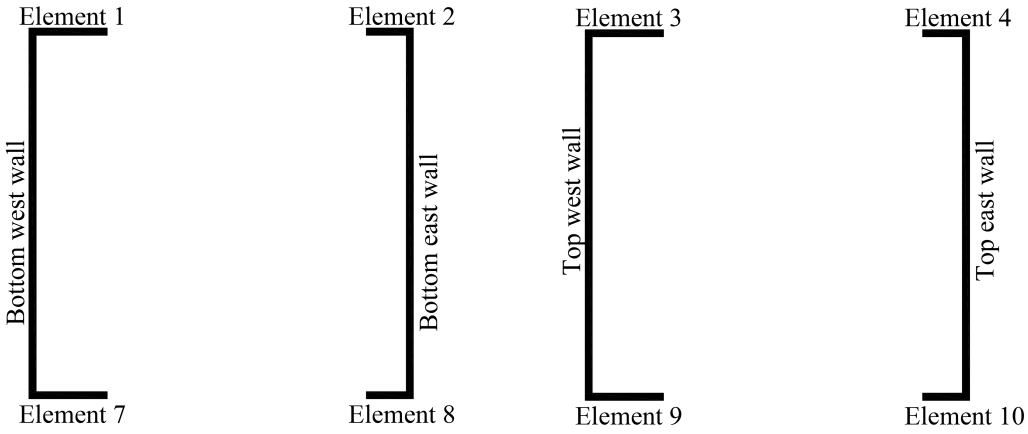

(a) ground floor **(b)** First floor

Figure 5.14: Schematization of the elements in 3Muri.

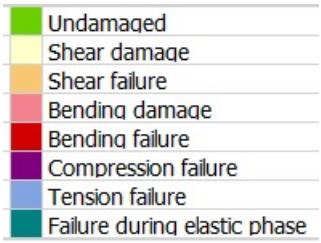

Figure 5.15: Failure or damage legend 3Muri.

5.4.2 Model 1: Reinforced concrete Beams

Since a connection between the piers is required, it is chosen in the first model to create a reinforced concrete beam which connects the piers. The reinforced concrete beam has the same properties as the concrete floor and is created at both the first and the second floor level. The beam has the same thickness as the floor (165 mm) and the same width as the piers (100 mm). The concrete strength class of the reinforced concrete beam is similar as the concrete floor of the case study (C55/67). It is chosen to apply steel bars of 2 ϕ8 (B500) at the top and bottom of the beam. With these properties the main goal is to simulate the rigid floor between the piers. The obtained three dimensional model and the meshing are visualized in Figure 5.16.
The beam is considered as a mesh element in the wall and is thus a part of the wall like the masonry panels. There is a connecting node between the piers and the beam.

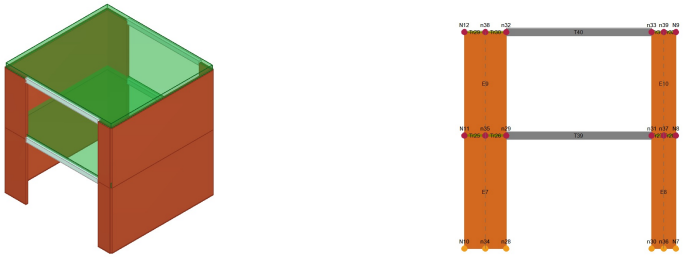

(a) 3D view **(b)** Meshing

Figure 5.16: Model 1 with reinforced concrete beam as connecting element.

The results obtained with this model are visualized in Figure 5.17. From the results it can be observed that the maximum displacement of the structure is relative low compared to the maximum displacement of the experiment and the SLaMA method. Additionally, most of the piers failed due to shear failure which was not observed during the experiment.

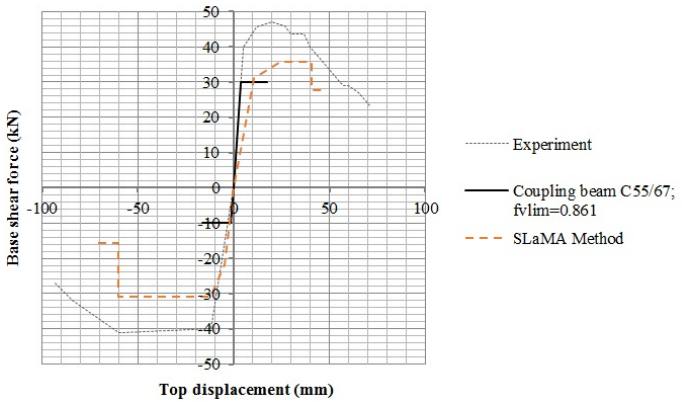

Figure 5.17: Pushover curve with the reinforced concrete beam, with h=165 mm, w=100mm and concrete class C55/67, as connection element.

In the experiment the piers failed due to flexural failure. In the definition of the materials in 3Muri, the only limit which is given is the shear strength limit of the masonry. In the NEN-EN-1996-1-1 the shear strength limit is determined with the following equation:

$$f_{vlim} = 0.065 \cdot f_b \tag{5.9}$$

In which f_b is the compressive strength of the masonry unit, therewith the f_{vlim} is here 0.8619 N/mm^2. S.T.A. DATA srl suggests to use a shear limit of 2.2 N/mm^2. A comparison is made between similar models where only the f_{vlim} is changed. If the f_{vlim} is changed into 2.2 N/mm^2, the displacement capacity is twice as high while the base shear capacity is constant. Additionally, flexural failure/damage is the only observed governing failure mechanism. In Figure 5.18 the failure mechanisms per facade are visualized when changing the f_{vlim}.
Additionally, the limit is defined in the Dutch guideline as $0.1f_b$ which limit is also higher than the Eurocode 8. Since the Dutch guideline maintains a higher upper limit for shear failure and the main goal of the modelling is to approach both the experimental results, the suggested value of 2.2 N/mm^2 will be used for the next models.

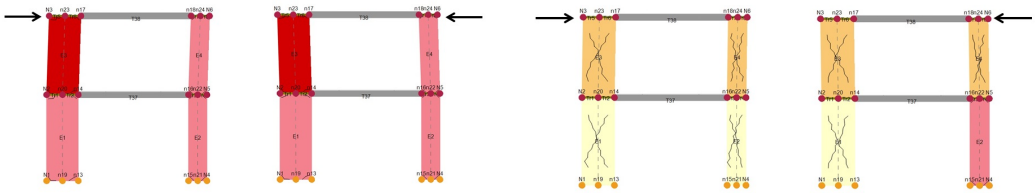

(a) f_{vlim}= 2.2 N/mm^2 **(b)** f_{vlim}= 0.8619 N/mm^2

Figure 5.18: Failure mechanism for a change in the f_{vlim}.

5.4.3 The effect of the load distribution on the seismic capacity of model 1

In the original model as explained in Section 5.4.2, the floor weight is uniform distributed between the transverse walls. However, during an earthquake a redistribution of the floor load is possible, this assumption was also made in the hand calculations. Therefore the load distribution of the floor during the initial static conditions towards the piers is varied and compared to the results obtained with the experiment. Two types of variations have been performed. Firstly, only the the weight of the second floor level is partly distributed to the piers. Secondly, the weight of both the first and the second floor level is partly distributed to the piers.
The properties of the model remain constant with as only variable the load distribution to the piers. The maximum load distribution towards the piers is 50%. If the load distribution is higher the displacements in the structure become too large for the analysis. The results are shown in Figure 5.19.

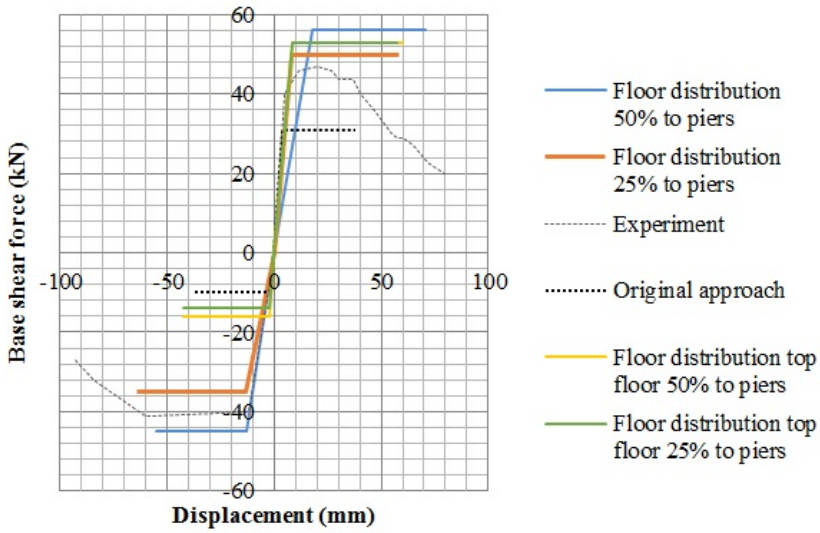

Figure 5.19: Pushover curve of the model with reinforced concrete beam (strength class C55/67, h=165 mm, w=100mm) with a redistribution of the floor loads during the initial static conditions.

From the results it can be observed that an increase of distribution of the floor weight to the piers has a positive influence on the structural capacity into both the positive and negative direction. In the models where only the load of the top floor is partly distributed to the piers, the structural capacity increases mainly into the positive direction. In the negative direction on the other hand the capacity is nearly similar as the original model. The models in which part of the load of both the first and second floor level is distributed to the piers, the structural capacity increases in both the positive and negative direction. In Figure 5.20 the failure mechanism are visualized per element with a change of the load distribution towards the piers. Flexural failure or damage is the governing mechanism in all the piers.
In the experiment failure was mainly concentrated in the bottom wider pier. From the results obtained with 3Muri it can be observed that failure in the negative direction is concentrated in element 1/7. The negative direction is the weakest direction, therefore it is expected that the first damage develops in element 1/7 which is similar as the experiment. In the positive direction failure is mainly concentrated in element 3/9, with as exception the model where the load distribution of the top floor is 50%. Additionally, in the model where the load distribution of both the floors is 50% element 4/8 fails as well. If loaded into the positive direction and the distribution is increased with 50% to the piers, it can be observed that the beam experience bending damage in the positive direction.

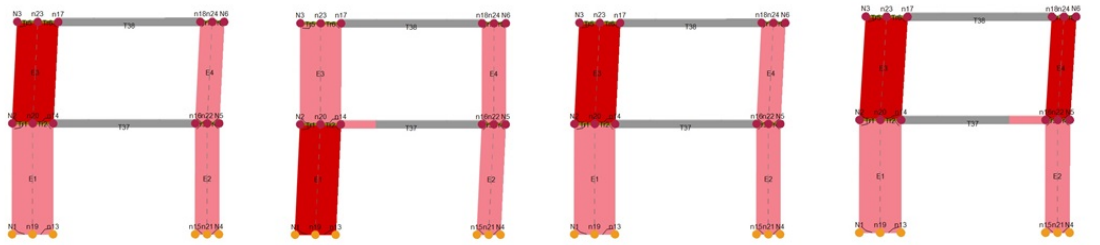

(a) Positive direction

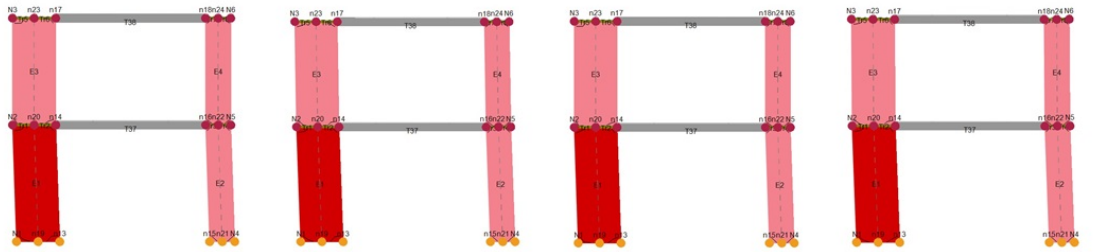

(b) Negative direction

Figure 5.20: Failure mechanism per element if the floor distribution is varied.

Failure of a element in 3Muri is generally determined by the exceedance of the drift limit. The drift limit in 3Muri can be determined with the following equation:

$$\delta = \frac{u_j - u_i}{h} + \frac{\phi_j + \phi_i}{2} \leq \delta_u \tag{5.10}$$

The nodes of the elements at both the top and bottom of the piers undergo small rotations and consequently the element is seen as a cantilevering element by the software, the maximum drift limit per element is determined for flexural failure in Table 5.6.

Table 5.6: Maximum drift limit per element determined according to the EC8.

Element	Drift limit
Element 1/7	2.89%
Element 2/8	4.99%
Element 3/9	2.65%
Element 4/10	4.56%

In Figure 5.21 the drift is visualized per element just before failure, the percentage of load of both the first and second floor level which is transferred to the piers is varied. In the original model, where no load is distributed to the piers, it can be observed that the drift of the piers is nearly equal to each other if located on the same floor level. For the other two models element 4/10 has the highest drift with respect to the other elements, however element 3/9 is governing and results into failure of the structure, see Figure 5.20. The drift not being equal to each other for elements located on the same level, is probably related to the axial load distribution in the elements.

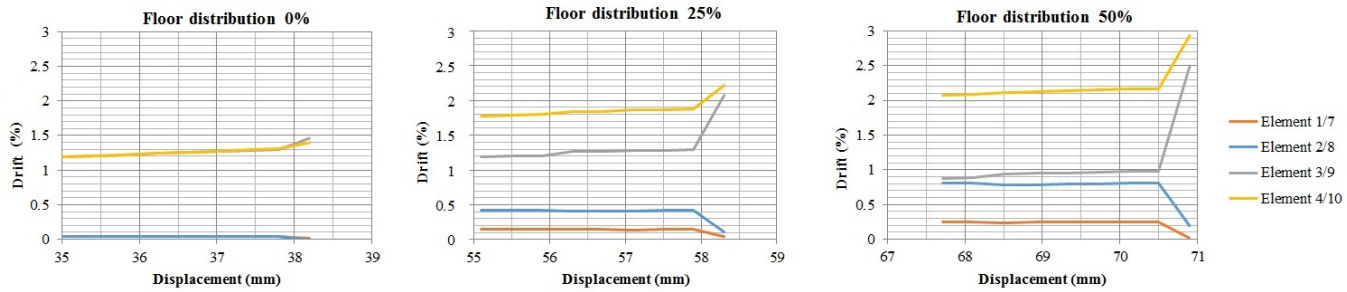

Figure 5.21: Drift of the piers just before failure into the positive direction, the floor distribution of both the first and second floor towards the piers is varied per graph.

In order to create a better understanding of the development of the drift per element, the development of the axial load in the piers per model is compared to each other. The comparison is visualized in Figure 5.22 in which the load distribution is varied for both the first and second floor. In Figure 5.25 the axial load distribution of the original model is visualized. From the original model it can be observed that the axial load in element 1/7 and 3/9 is higher than in element 2/8 and 4/10. This is related to the activation of the flange from which a part of the weight is distributed to the pier. The axial load distribution of the original model is different with respect to the models where the load distribution towards the piers is increased.
In the models with increased floor distribution towards the piers, the activation of the flange is only visible in element 1/7 and not in element 3/9. However, the activation of the flange should also be visible in element 3/9 according to the physics. The axial load decreases in element 3/9 and increases in 2/8 and 4/10 if more load is distributed to the piers.

With the uplift of the floor, a redistribution of the loads is observed. The axial load distribution increases towards the piers around which the structure rotates, in this case element 2/8 and 4/10. Additionally, with an increase of the load distribution towards the piers, the difference between the axial load in the elements 3/9 and 4/10 increases. Still, if we look at the total axial load per floor level in the piers, the total axial load in the piers on the same floor level is nearly similar at the start and end of the analysis.

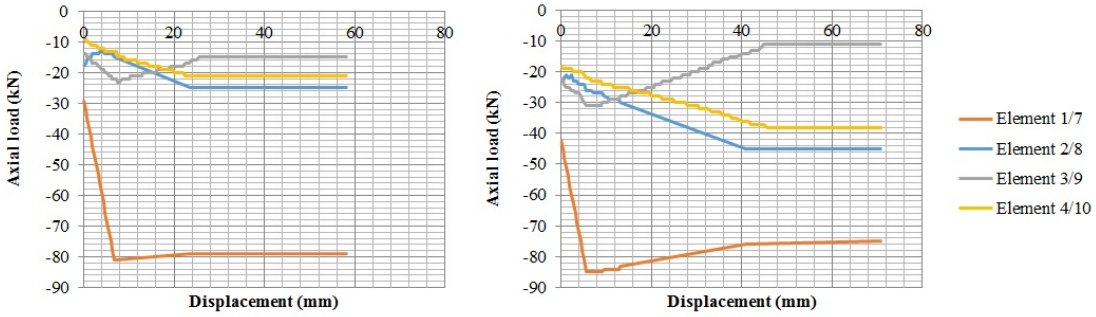

Figure 5.22: Axial load distribution in the piers, left: 25% of the load of both the floors is transferred to the piers and on the right: 50% of the load of both the floors is transferred to the piers.

Finally, in all the models a relative high increase in the drift can be observed for all the elements in the last step of the analysis. In the model with a floor distribution of 25% to the piers for example, the drift increases with 59.8% for element 3/9 in one displacement step and for a floor distribution of 50% to the piers, the drift increases even with 158%. This is probably related with failure of the element.

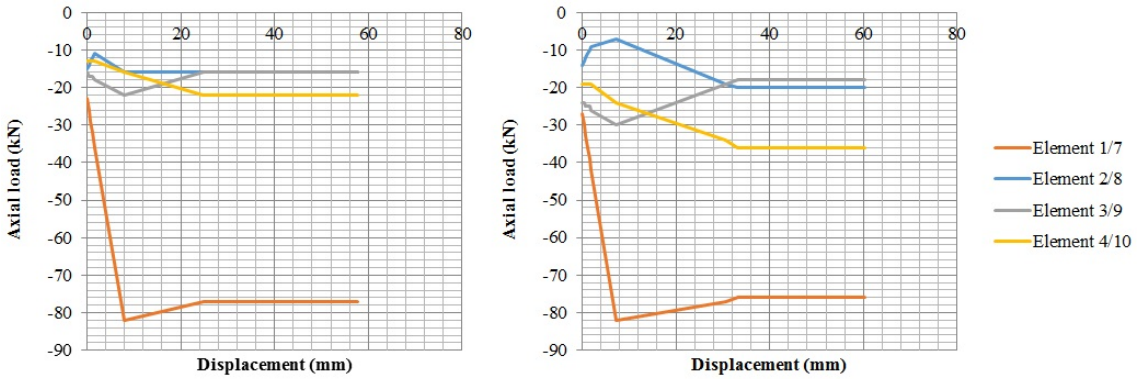

Figure 5.23: Axial load distribution in the piers, left: 25% of the load of the top floor is transferred to the piers and on the right: 50% of the load of the top floor is transferred to the piers.

Similar behavior is observed for the structure where the load of only the top floor level is distributed to the piers. In Figure 5.23 the axial load in the piers is visualized for a variation of the load distribution of the top floor only. From the figure it can be observed that the flange is activated in element 1/7. The initial axial load on top elements 1/7 and 3/9 is similar as the previous model (25% or 50% load distribution of both floors towards the piers), but the development of the axial load distribution is not similar as the previous models for element 3/9. The load distribution of the top floor is similar, but the axial load in element 3/9 at the end of the analysis is higher than the previous models. Additionally, the axial load at the end of the analysis in element 2/8 is lower than the previous models. Since there are no changes in the load distribution of the second floor level, this observation suggests that the load distribution of the floor located underneath an element can influences the axial load of that element. This is in contrast to the physics.

The development of the drift was also similar as for the previous explained model. In the last step of the analysis a rapid increase of the drift was observed for the elements 3/9 and 4/10 if loaded into the positive direction.

5.4.4 The effect of the properties of the connecting beam on the seismic behavior of model 1

In the second model the parameters of the connecting beam are varied. Since the beam is an approach to simulate the behavior of the case study the parameters are varied in order to observe which properties approximate the experimental results the most accurate. First, only the concrete class of the beam is changed and the dimensions of the beam are similar as the initial model. Secondly, the size of the beam is decreased to a height of 100 mm and a width of 100 mm and additionally the concrete class is changed. The results of these variations are visualized in Figure 5.30.
From the results it can be observed that the capacity of the structure increases with a decrease of the size of the beam. However, no significant difference is observed in the loads which are transferred by the connection beam. It can be derived that the beam its main function is to connect the piers. The influence of the concrete class on the structural capacity is not very notable. The decrease of the beam size does significantly effect the seismic capacity. In order to explain the increase of the seismic capacity with the "small" sized beam (the less stiff beam), the axial load distribution in the elements will be analyzed. In Figure 5.25 the axial force distribution in the piers is visualized for both the beam sizes with a concrete strength class C55/67, loaded into the positive direction.

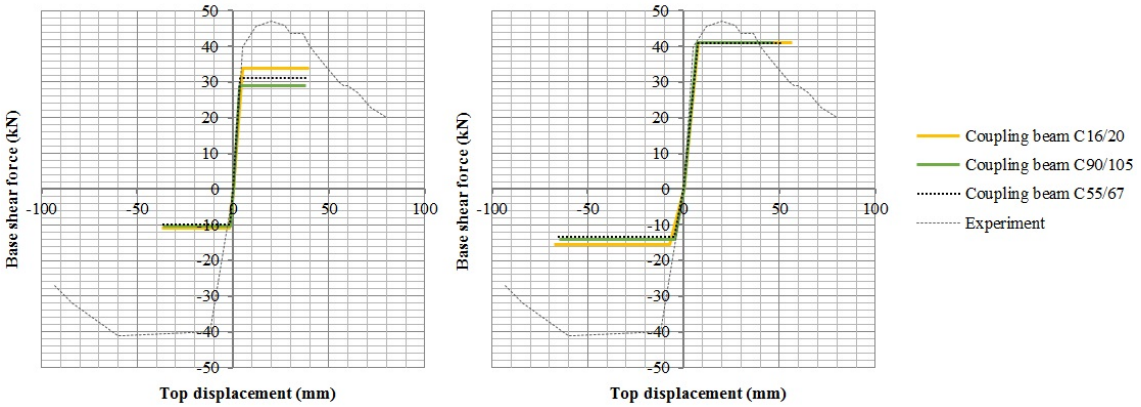

Figure 5.24: Model with changed properties of the reinforced concrete beam, left: beam size; h=165 mm, w=100 mm and on the right: beam size; h=100 mm, w=100 mm.

From the results it can be observed that the axial load in the piers, which are connected to each other with the small sized beam, can be nearly twice as high than the large sized beam. If the structure is loaded in the positive direction the axial load increases significantly in both elements 1/7 and 3/9. This is related with the activation of the flange as explained before.
The additional axial load in the elements originates from the transverse walls. In Figure 5.26 the axial load distribution in the transverse walls is visualized. It can be observed that the axial load decreases significantly in the bottom west wall with an increase of the displacement. If these graphs are compared with the graph of the axial load distribution in the pier (Figure 5.25), it can be observed that while the axial load decreases in the transverse wall at the west side, the axial load increases at the same time in the piers at the west side. With a less stiff connection more weight of the transverse walls is transferred to the piers, consequently the structural capacity of the piers and thus the total structure increases.

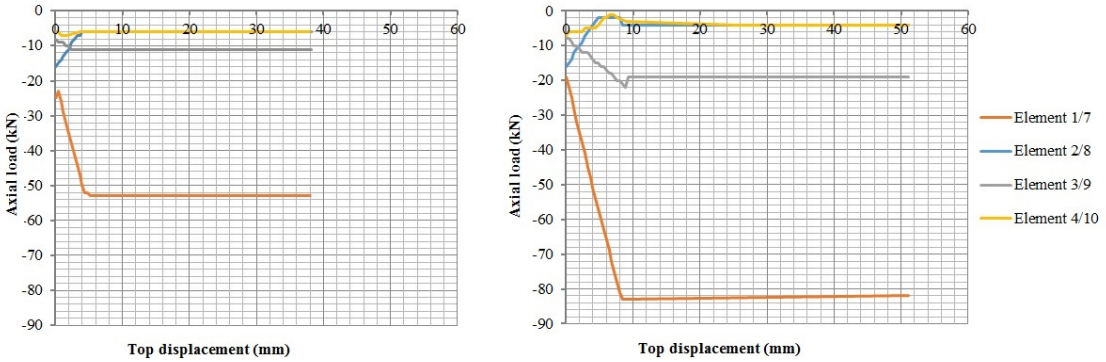

Figure 5.25: Axial load in the piers loaded in the positive direction with on the left: beam size; h=165 mm, w=100 mm and on the right: beam size; h=100 mm, w=100 mm. The concrete class of both the beams is C55/67.

In the model where the large sized beam is applied 44.5% of the load of the bottom west wall is distributed to the pier. In the model with the small sized beam 100% of the load of the bottom west wall is distributed to the piers. The axial load which is transferred from the west wall to the pier stabilizes in the model with the large size beam at a displacement of 4.4 mm and in the model with the small size beam at a displacement of 8.4 mm.
In Figure 5.27 the drift is visualized for the two models in which the geometry of the beam is varied. The concrete class for both the models is C55/67. As mentioned before, the drift is nearly

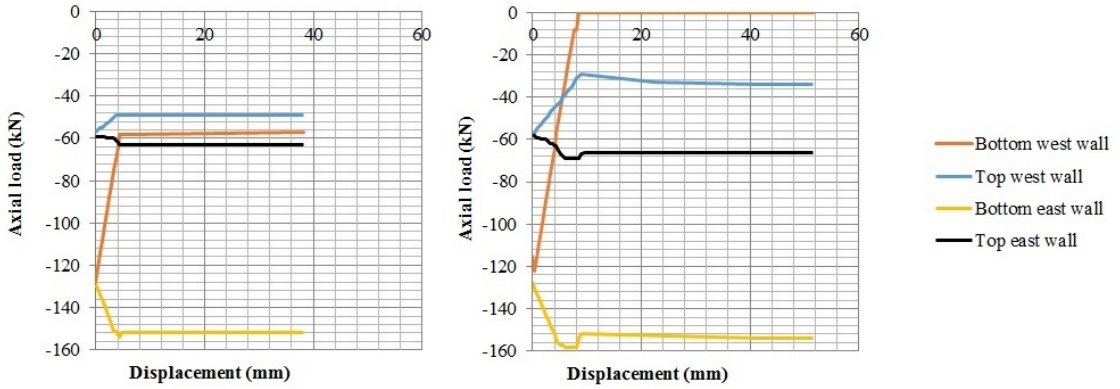

Figure 5.26: Axial load in the transverse walls loaded in the positive direction with on the left: beam size; h=165 mm, w=100 mm and on the right: beam size; h=100 mm, w=100 mm. The concrete class of both the beams is C55/67.

equal for the piers at the same level if the large beam is applied. If the small beam is applied, the drift vary per pier even if located on the same floor level. With the small beam, the connection is less stiff between the piers and the piers freedom of movement is larger.
In the last step of the analysis a relative high increase of the drift can be observed. For the small sized beam an increase of 20.3% can be observed for element 4/10, this increase is even higher for element 3/9 namely 52.1%. For the large sized beam the increase of the drift is relative low in the last step.

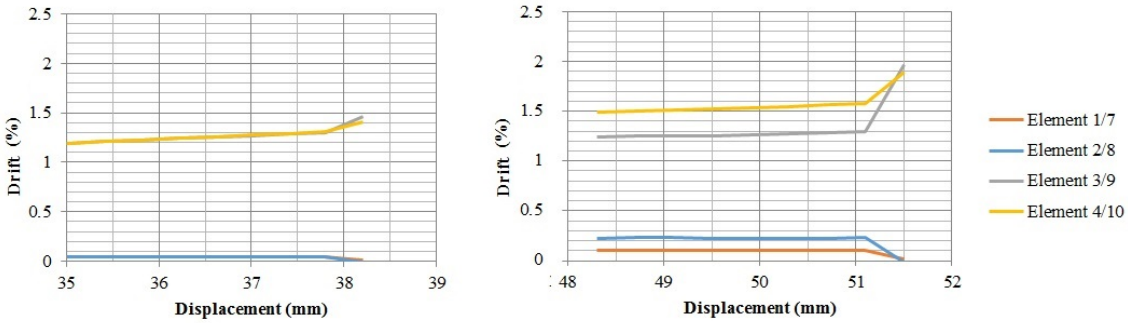

Figure 5.27: Drift of the piers just before failure into the positive direction. With on the left: beam size; h=165 mm, w=100 mm and on the right: beam size; h=100 mm, w=100 mm. The concrete class of both the beams is C55/67.

5.4.5 Model 2: Reinforced concrete lintel

In the second variation model a reinforced concrete lintel, also named as encirclement in 3Muri, is used to create a connection between the piers. An encirclement is according to S.T.A. DATA srl reinforcement which is related to the masonry elements in which the opening is modelled. Similar as the first model the properties of the encirclement are similar as the concrete floor of the case study: with a concrete strength class C55/67, thickness of 165 mm and a width of 100 mm. Additionally, it is chosen to apply steel bars of 2 ϕ8 (B500) at the top and bottom of the lintel. The obtained three dimensional model and the meshing are visualized in Figure 5.28. As regards the mesh of the element, the encirclement is connected to the same node as the pier. In contrast to the first model, there is no intermediate node between the pier and the encirclement.

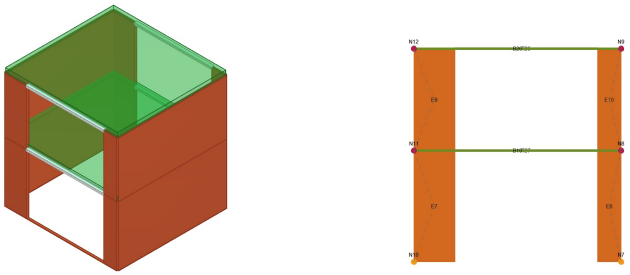

(a) 3D view **(b)** Meshing

Figure 5.28: Model 2 with encirclement as connecting element.

The results obtained with this model are visualized in Figure 5.29. From the results it can be observed that the maximum base shear force of the model is relative low compared to the SLaMA method and the experiment. In the positive direction the deviation of the base shear force is 36.3% and in the negative direction the deviation is 75% from the experiment. In the following section the properties of the encirclement will be changed in order to approach the results. Unfortunately, it is not possible with this model to vary the load distribution, the displacements become too large to obtain results. It must be noted that the $f_{v,lim}$=2.2N/mm^2 for the models as explained in Section 5.4.2.

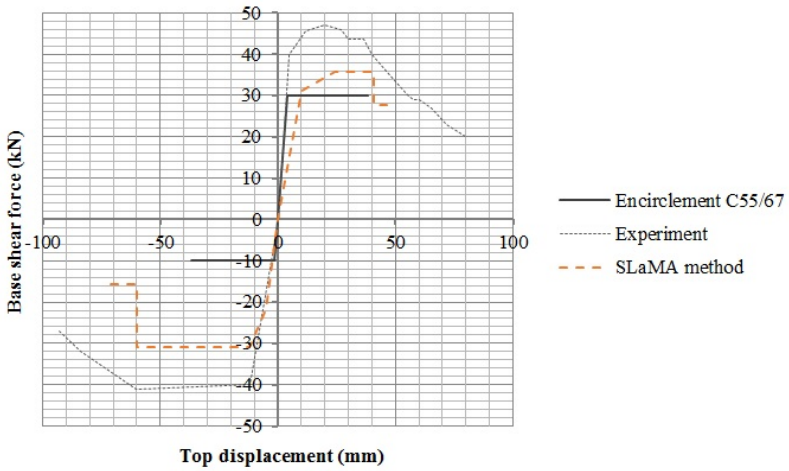

Figure 5.29: Pushover curve encirclement, height=165 mm, width=100 mm and concrete class C55/67.

5.4.6 The effect of the properties of the lintel on the seismic behavior of model 2

For this model the parameters of the encirclement (lintel) are varied. Firstly, only the concrete class of the encirclement is changed and the dimensions of the encirclement are similar as the initial model. Secondly, the size of the encirclement is decreased to a height of 100 mm and a width of 100 mm and additionally the concrete class is changed. The results of these variations are visualized in Figure 5.30.

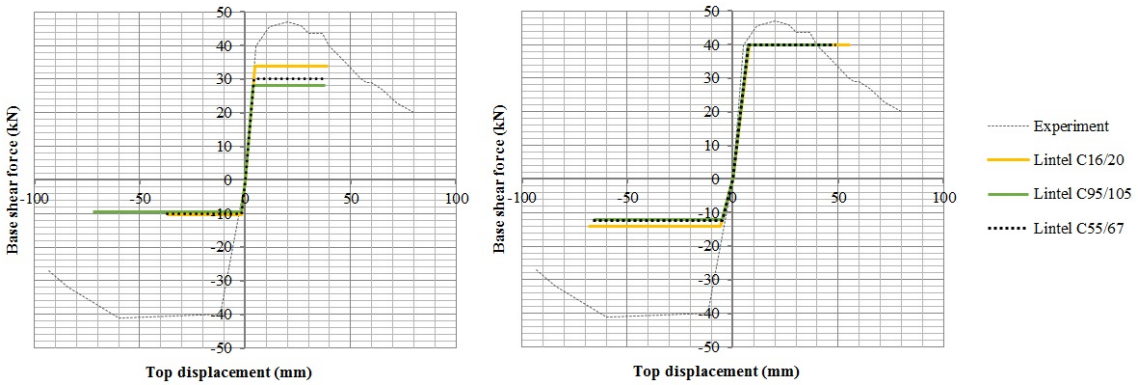

Figure 5.30: Model with change of properties of the encirclement, left: encirclement size; h=165 mm, w=100 mm and on the right: encirclement size; h=100 mm, w=100 mm.

From the results it can be observed that the capacity of the structure increases with a decrease of the size of the encirclement. The structure reacts similar as the model with the reinforced concrete beam as connecting element. In Figure 5.31 the axial load distribution in the transverse walls is visualized. The axial loading decreases in the walls at the west. In Figure 5.32 the load distribution in the piers is visualized. The axial load in the piers on the other hand increase at the west side. The load is transferred from the transverse wall to the pier due to the activation of the flange. With a decrease of the size of the encirclement the axial load transfer originating from the transverse wall increase until it approaches zero.

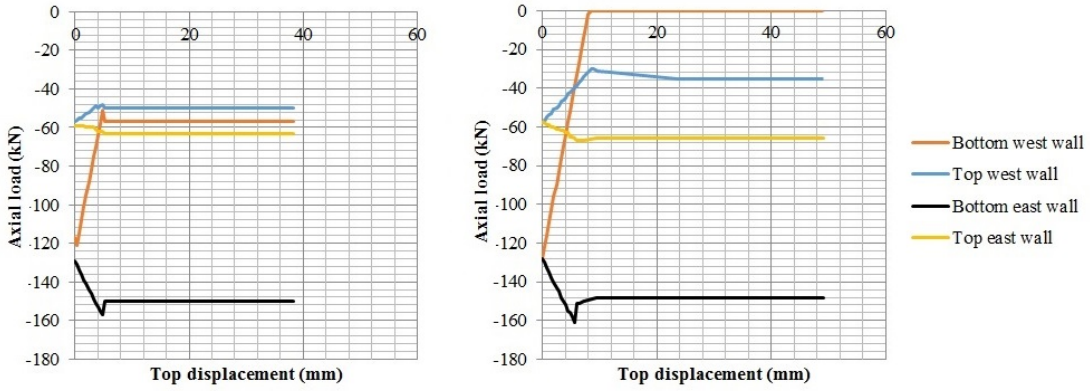

Figure 5.31: Axial load distribution in the transverse walls with changed properties of the encirclement, left: encirclement size; h=165 mm, w=100 mm and on the right: encirclement size; h=100 mm, w=100 mm. The concrete class of both the encirclements is C55/67.

The drift of the encirclement is analyzed by comparing the drift of the models in which the geometry of the encirclement is varied, the concrete class of the encirclement is C55/67. In

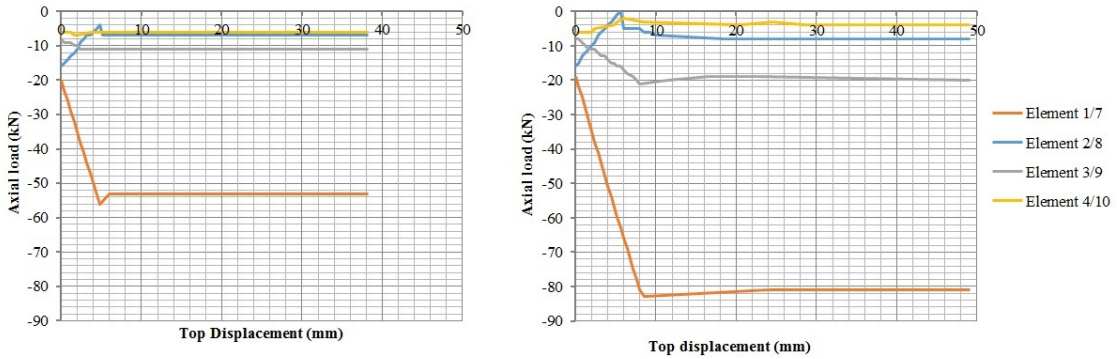

Figure 5.32: Axial load distribution in the piers with changed properties of the encirclement, left: encirclement size; h=165 mm, w=100 mm and on the right: encirclement size; h=100 mm, w=100 mm. The concrete class of both the encirclements is C55/67.

Figure 5.33 the drift is visualized per displacement step in the analysis just before failure. Similar as for the model with the reinforced concrete beam the drift is nearly similar for the piers on the same floor level if the large encirclement size is applied. If the small encirclement size is applied, the drift varies per pier even if the piers are located on the same floor level. The similar phenomena was observed for the model with the reinforced concrete beam as connecting element. The small encirclement is less stiff which enables to piers to behave more independently from each other.

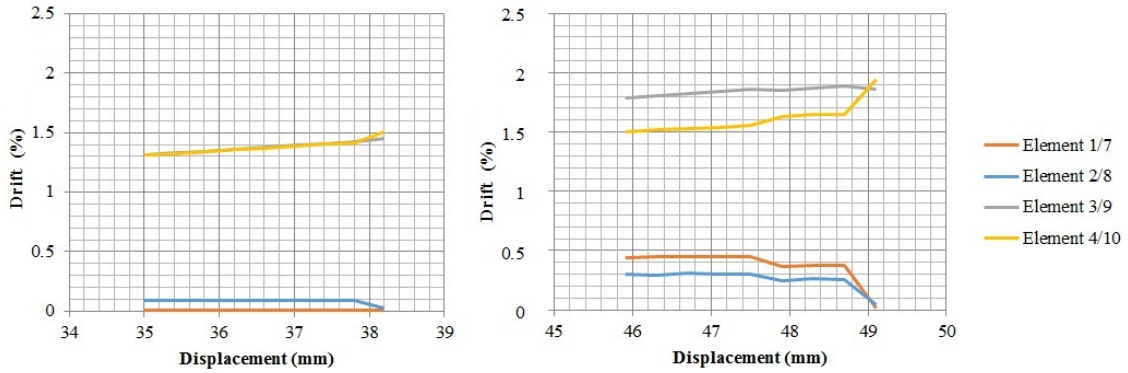

Figure 5.33: Drift of the piers just before failure into the positive direction. With changed properties of the encirclement, left: encirclement size; h=165 mm, w=100 mm and on the right: encirclement size; h=100 mm, w=100 mm. The concrete class of both the encirclements is C55/67.

5.5 COMPARISON RESULTS SLAMA AND 3MURI

In this section the results obtained with the SLaMA method and 3Muri are compared to each other. From the different modelling approaches in 3Muri first the most accurate model has to be selected.

Selection most accurate 3Muri model

The results obtained with either the reinforced concrete beam or the reinforced concrete lintel as connecting element are equivalent in 3Muri. Even if the properties of the connecting element are varied, the results are similar. The main difference between the models is situated in the mesh of the structure. Since this is the main difference between the reinforced concrete beam model and the reinforced concrete lintel model, it is chosen to select the mesh which serves as the better representation of the physical model. It is expected that the behavior of the reinforced concrete beam simulates the behavior of the structure the most accurate. The reinforced concrete beam and pier are connected to the same node, resulting in a mesh in which the beam is part of the wall. This in contrast to the lintel which serves as reinforcement between the adjacent piers.

As regards the variation of the beam properties it was observed that with the original size (h=165mm, w=100mm) and a concrete class C55/67, the drift of all the piers at the same level is equal. This in contrast to the model where the small beam size is used. The piers behave more independently from each other due to the fact that the connecting element has a lower stiffness. In order to make a realistic comparison to the experimental results, the use of the stiffer beam seems more obvious. With the stiff beam as connecting element the piers don't behave independently from each other which was the case in the experiment. In the experiment the floor is imposed at the piers at the second floor level and moreover the piers are interlocked with the transverse walls. If the piers would behave independently from each other large cracks are expected to develop in the floor. Therefore, it is chosen to use the beam with the initial size; height = 165 mm and width = 100 mm.

An additional modelling choice which can be made for the reinforced concrete beam as connecting element is the distribution of the floor load in the initial static conditions towards the piers. With an increase of the distribution of the floor load in the initial static conditions towards the piers, the structural capacity of the model increases and is therewith a better approach for the structural behavior of the experimental structure. However a similar phenomena is observed for this model in which the drift varies per element even if located on the same floor level, if the load distribution is increased towards the piers.
On the other hand, the floor distribution modelling approach gives a more accurate approach for the development of the failure mechanism in the structure. Damage starts to develop at the lower wider pier which is similar as in the experiment. This in contrast to the original model with the large sized beam where failure is concentrated in the element 3/9 which is located at the top of the structure.
To conclude, the most accurate model obtained with 3Muri to simulate the behavior of the structure during the experiment would be the original model. In this model the reinforced concrete beam is used as connecting element, with a height of 165 mm, width of 100 mm and concrete class C55/67. However, the failure mechanism is not properly obtained from this modelling approach. With this approach failure is concentrated in element 3/9 in both the positive and negative direction. This in contrast to the experimental results in which the damage was concentrated into element 1/7.

Comparison results SLaMA and 3Muri

A new analysis is done with 3Muri in which the strength decay of the model previously selected is adjusted. According to the Eurocode 8 the failure is determined by a strength decay of 20%, but in the NPR9998 this decay is 50%. In order to make a fair comparison with the SLaMA method, the NC limit state in 3Muri is reached after a 50% strength decay as well. The overall capacity of both the SLaMA method and 3Muri are presented in Figure 5.34. With a strength decrease of 50% in 3Muri the results only vary into the negative direction in which larger drifts can be obtained. In the positive direction no change is visible in the displacement capacity. After failure of the first elements (element 3/9) into the positive direction, the strength decrease of 50% is already reached. Changing the strength decay value from 20% to 50% thus doesn't result in any changes of the displacement capacity.

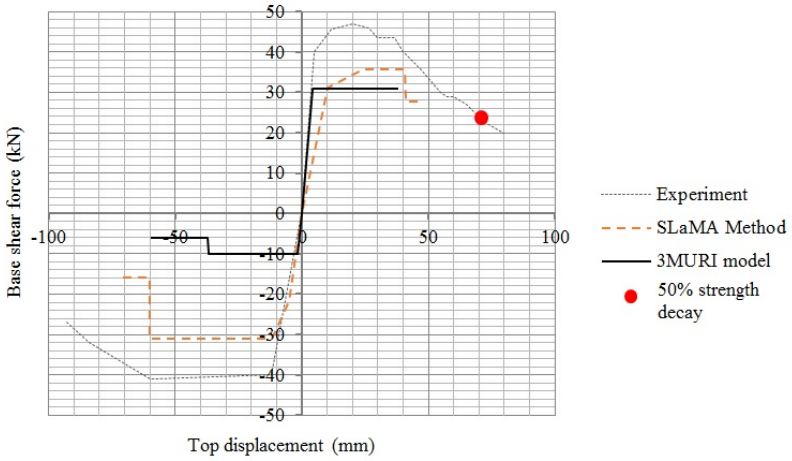

Figure 5.34: Pushover curve obtained with SLaMA and 3Muri.

In Table 5.7 the deviation with respect to the experiment is presented. It can be derived from both the pushover curve and the deviations that the most accurate model obtained with 3Muri still highly underestimates the capacity of the structure as obtained with the experiment. The solution to model a connecting element between the piers, since there is no spandrel present, and the fact that 3Muri is not able to model the piers spanning from the ground floor until the second floor level don't give results which are satisfactory. The current employed version of 3Muri is not able to give a proper approach to model this specific case study.
The results as obtained with the SLaMA method deviate around the 25%, but give a proper approach to the experimental results. Moreover, according to the calculations the negative direction is the weakest direction in which failure of the wider pier in the SLaMA method is governing (pier 1/3). This is equivalent to the governing failure mechanism in the experiment.

Table 5.7: Deviation with respect to the experiment

	Base shear force		**Ultimate displacement**	
	+	-	+	-
SLaMA	-24.4%	-22.5%	-33.6%	-23.8%
3Muri	-34.2%	-75%	-45%	-35.8%

6 CASE STUDY: MARTINI TYPE K.

In this chapter a new case study will be introduced, the Martini type K terraced house. The case study its characteristics will be introduced and afterwards the SLaMA method will be applied to determine the seismic capacity of the building. The NPR9998-2018 is used as guideline for SLaMA. The case study is also analysed with the software 3Muri version 12.2.1.4, the focus is on the use of the Eurocode 8 as guideline. Finally, the results of both the methods will be compared to each other and discussed.

6.1 CHARACTERISTICS OF THE CASE STUDY

The Martini Type K house is located in Loppersum in the province of Groningen and is designed in 1967 by architect J. Martini. The building concerns a two-storey URM building which consists of a block of four connected terraced house. The front facade of the building is shown in Figure 6.1. The Martini type K house can be classified into the typology "block unit multiple" as described in Chapter 4. The buildings within the typology are characterized by a horizontal repetition of units, but still form a homogeneous block with a gutter height of approximately 10 meters.

Figure 6.1: Front facade of the case study Martini type K.

6.1.1 Load bearing structure

The load bearing structure of the building consists out a cavity construction. The inner leaf is constructed from CS bricks and the outer leaf from burnt clay bricks. The houses are separated from each other by CS walls of 200 mm, the party walls within the house are CS walls of 100 mm. The load bearing structure is visualized in Figure 6.2. The CS party walls of 7 mm are neglected here, these walls are oriented into the X-direction. It is assumed that these walls don't have a significant contribution to the seismic capacity of the structure. Additionally, a storage room is located at the back of each house. The storage room is not taken into account for the determination of the seismic capacity. It is considered that the storage room don't contribute to the seismic capacity of the building, failure of the storage room would be addressed as local failure. The original drawings of the Martini type K house can be found in Appendix C.

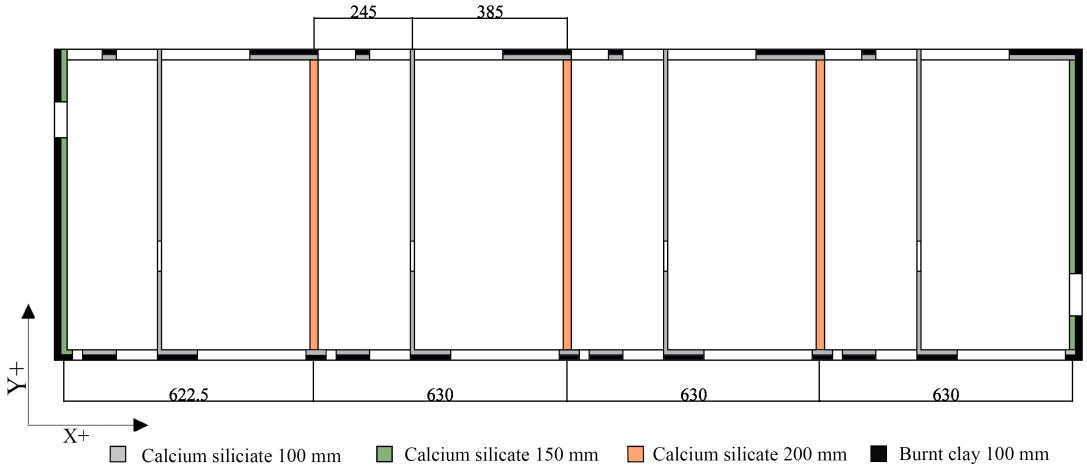

Figure 6.2: Load bearing structure of the Martini type K house.

The floors in the building at the first and second floor level consist of reinforced concrete which spans into the X-direction between the 200 mm CS walls and the 150 mm CS gable walls. The bottom floor is a timber floor. The roof spans in the X-direction as well and is supported by the party walls of 200 and 100 mm and the gable walls of 150 mm. At the party walls of 100 mm the roof is supported by a timber truss which is split into four point loads, two on each side of the party wall. The point load is transferred by the 100 mm CS wall to the foundation. Where the roof meets the gable walls of 150 mm and the party walls of 200 mm, timber purlins are used as a support. In Table 6.1 an overview of the material properties of the masonry are given. The properties are mainly obtained from the NPR9998 in which the average material properties are summarized for URM constructed around 1960.
From the load bearing structure it can be concluded that the seismic capacity in the X-direction is weaker since there is a minority of load bearing walls into this direction. Hence, the seismic capacity will be determined for the X-direction only.

The inner and outer leaf are connected to each other with galvanized cavity anchors. The wind load is transferred to the load bearing structure through these anchors. The main function of the outer leaf is to carry its own weight and serve as a barrier to the outer climate.
Due to the low shear and bending capacity of the cavity anchors, no significant contribution of the outer leaf is expected for load-bearing structure when loaded in-plane. Failure of the outer leaf due to a poor connection, can be be seen as local failure as explained in Section 2.2.2. The additional weight of the outer leaf is taken into account if the gable wall behaves as a flange since the anchors are able to transfer axial loading. Still, there is no information about the condition

Table 6.1: Material properties of the masonry in the Martini type K house.
Source: NPR9998

Symbol	Material property	Value
E	Elastic modulus perpendicular to the bed joints	4000 N/mm^2
G	Shear modulus	1650 N/mm^2
f_{v0}	Initial shear strength masonry	0.25 N/mm^2
f_m	Compressive strength mortar	5 N/mm^2
f_b	Compressive strength masonry unit	12 N/mm^2
f'_m	Compressive strength masonry perpendicular to the bed joints	7 N/mm^2
μ	Shear friction coefficient masonry	0.6
$w_{masonry}$	Density masonry	20 N/mm^3
$w_{concrete}$	Density concrete	25 N/mm^3

of the anchors and it plausible that the anchors are corroded which would result in a decrease of the structural capacity of the element.

6.1.2 Soil conditions

As regards the soil conditions DINOloket was used to obtain the properties of the soil. These are represented in Table 6.2.

Table 6.2: Soil conditions.
Source: DINOloket

Top Layer	Bottom Layer	Soil type
0	-4	Clay
-4	-7	Sand
-7	-9	Clay
-9	-11	Sand
-11	-14.5	Clay
-14.5	-60	Sand
-60	-70	Rough sand

6.1.3 Foundation

For the construction of the terraced house a concrete strip foundation is used. On top of the foundation timber joists are placed with on top of these beams the timber ground floor. It is assumed that the connection between the masonry and the concrete is fixed to a certain extent. It is assumed that this connection is not the governing aspect which would lead to global failure. This is in line with the NPR9998 which describes the fact that the foundation is rarely governing since foundations are able to resist deformations which occur during an earthquake.

6.1.4 Loading

For the case study both the dead and variable load are present and should be taken into account for the determination of the seismic capacity of the structure. The NPR9998 prescribes to take a reduced variable loading into account by means of a combination coefficient which takes the chance into account that the variable loading is present over the total structure during an earthquake. The following loading equation is prescribed to determine the representative calculation load (E_d):

$$E_d = \Sigma\phi \cdot \psi_{2;i} \cdot Q_{k;j} + \Sigma G_{k;j} \tag{6.1}$$

In which $G_{k;j}$ represents the dead load and $Q_{k;j}$ represents the variable load. For the determination of the combination coefficient ($\phi\psi_{2;i}$) the class of the building is required, these classes are classified in the NEN-EN 1991-1-1. The terraced houses are classified as a Class A building with a variable loading of 1.75 kN/m^2. The corresponding combination coefficients are: ϕ = 0.6 and $\psi_{2;i}$ = 0.3. An overview of the loads in the structure is visualized in Table 6.3

Table 6.3: Applied loads on the structure.

Element	**Dead load [kN/m^2]**	**Variable load [kN/m^2]**	**Total Load**
Roof	0.808	-	0.808
Floor	2	0.315	2.315

6.2 OUT-OF-PLANE BEHAVIOR

For the out-of-plane assessment of the walls annex H of the NPR9998 is used. As explained in Section 5.2.3 the resistance of the elements is not correctly defined in the NPR9998. For this reason the guideline of New Zealand will be used as an additional check.
For the assessment of the gable, the worst-case scenario is assumed in which the anchors are fully corroded and the inner and outer leaf are not connected to each other. Consequently, the inner and outer leaf are assumed to work independently from each other, the out-of-plane assessment is thus required for both the inner and outer leaf separately.
For the gable walls it can be assumed that the walls are one-way spanning. The inner leaf, which is part of the load bearing structure, spans vertically over one floor level. Additionally, the wall is interlocked horizontally at the corners with the in-plane walls which results in the inner leaf to span also sideways. However, due to the relative large width between the in-plane walls, the interlocking at the corners is neglected. The inner leaf is considered to span one-way only in the vertical direction. For this reason annex H of the NPR9998 can be used, which describes the method for one-way spanning walls only. This procedure is also applicable for the outer leaf which behaves similar as the inner leaf. The main difference with respect to the inner leaf is the fact that the outer leaf is not part of the load bearing structure and that the leaf spans vertically between the foundation and the second floor level. The mechanisms which develop are visualized in Figure 6.3.

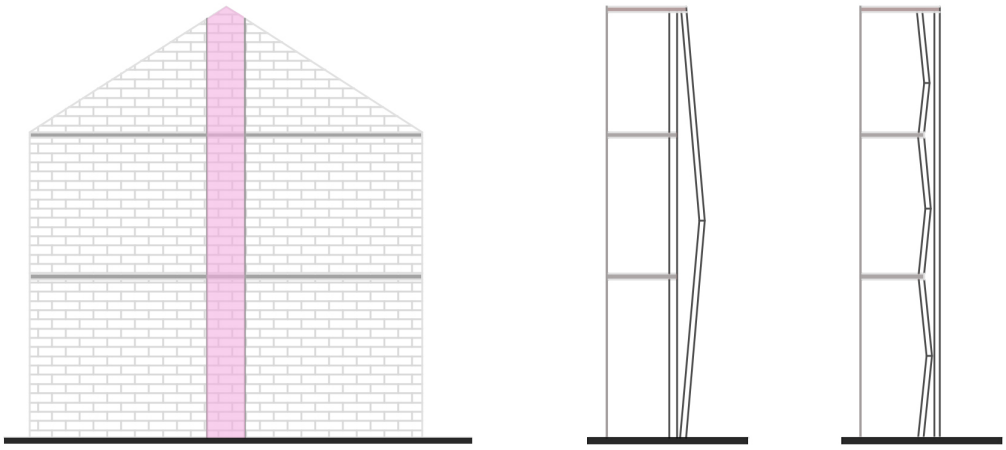

Figure 6.3: Out-of-plane mechanisms which develop for the area marked at the facade. On the left the mechanism which develops for the outer-leaf and on the right the mechanisms which develops for the inner-leaf is visualized.

6.2.1 Inner leaf

The inner leaf is divided into three separate elements which might develop during an earthquake. The resistance (R_d) and the seismic loading ($S_{a;d}$) are determined for each element. The weight of the outer leaf is not taken into account as additional overburden as explained before. The seismic resistance of the elements is summarized in Table 6.4. From the calculations it can be determined that all the elements of the inner leaf satisfy the criteria and are able to withstand

the seismic loading, the seismic loading is lower than the seismic resistance. This despite the fact that the weight of the outer leaf is neglected.

Table 6.4: Out-of-plane capacity inner leaf elements.

Element	Top	Bottom	Sa;d [g]	Rd [g]
1	Roof	2nd Floor level	0.164	0.270
2	2nd Floor level	1st Floor level	0.337	0.780
3	1st Floor level	Foundation	0.307	>1

6.2.2 Outer leaf

The outer leaf is one single element which spans directly between the foundation and the second floor level. In Figure 6.4 the connection between the outer leaf and the top floor is visualized. Based upon this section it can be determined that the outer leaf is connected to the concrete floor by a timber connection element. However, the dead load on top of the outer leaf is still zero since all the load of the roof and the concrete floor is directly transferred to the inner leaf. This results into an element which has a maximum height of 7.9 meters with zero dead load and it can be determined that this element would not withstand any seismic loading.

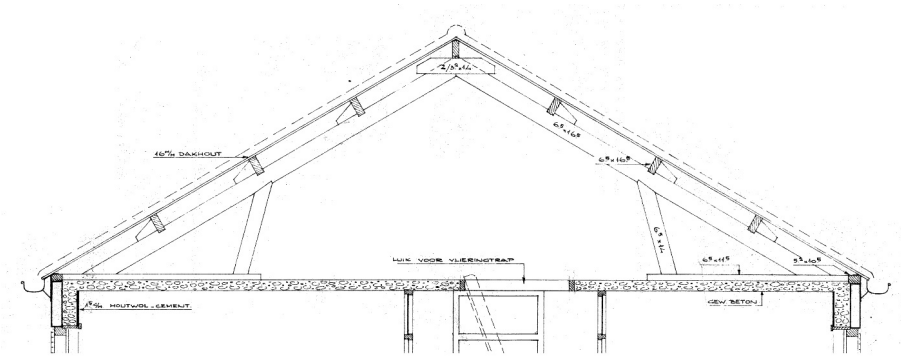

Figure 6.4: Section roof.

6.2.3 Party walls

The capacity of the party walls is essential for the in-plane capacity of the piers since the party walls behave as additional overburden. Two type of party walls can be distinguished with a thickness of 100 or 200 mm. The out-of-plane resistance is determined for the party walls located at the first floor level since the out-of-plane capacity decreases with a decrease of the weight on top of the elements. Consequently, the elements on the first floor level are weaker than the elements located on the ground floor level. The out-of-plane capacity of the elements can be found in Table 6.5. From this table it can be determined that the party walls satisfy the criteria. Since the walls of the first floor level are able to withstand the seismic loading, the party walls on the ground floor level will also be able to withstand the seismic loading.

Table 6.5: Out-of-plane capacity party walls.

Element	Thickness [mm]	Sa;d [g]	Rd [g]
1	100	0.183	0.190
2	200	0.259	0.950

6.3 IN-PLANE BEHAVIOR

For the determination of the in-plane capacity of the piers, the effective height and the boundary conditions are essential in order to have an accurate estimation of the capacity. The activation of the flange is taken into account if the axial load is distributed to the pier. The flange weight as additional overburden is assumed to be present for all the failure mechanisms except for diagonal tensile failure, as explained before. An example for the area which contributes as a flange for the gable wall is visualized in Figure 6.5.

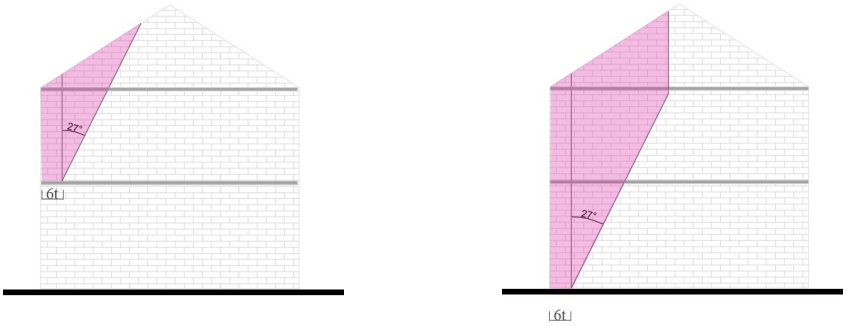

(a) Flange first floor level **(b)** Flange ground floor level

Figure 6.5: Flange weight of the outer piers.

According to the NPR9998 the axial load distribution from the flange to the pier is taken into account when the pier rotates and the neutral axis displaces from the heart of the flange to the edge of the flange. If the flange is in tension the weight of the flange is taken into account as additional overburden for the corresponding pier. However, there are exceptions in the geometry of the floor plan of the case study where the flange is not fully in tension. An example is given in Figure 6.6.

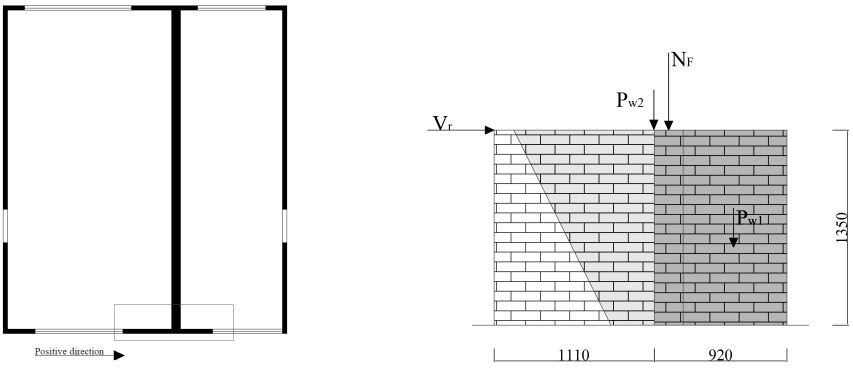

(a) Flange first floor level **(b)** Flange ground floor level

Figure 6.6: Flange effect flange in compression.

It is assumed that the compression strut develops towards the point where the highest loading is located on top of the pier. Since there is no additional load on top of the pier, except the flange, it is assumed that the compression strut develops towards this load. It is chosen to change the geometry of the pier as visualized in Figure 6.6b. The dark grey area represents the new geometry of the pier. Additionally, it is assumed that the "additional pier" (light grey coloured in Figure 6.6b) is also lifted together with the rotation of the pier. Therefore the weight of the

"additional pier" is determined as a regular flange and is added to the overburden of the newly defined pier.

For the determination of the in-plane strength of the elements, the diagonal tensile capacity of the piers is not taken into account. According to the NZSEE (2017) shear sliding failure prevails over diagonal tensile failure in piers with low axial loading in combination with relative low mortar strength with respect to the bricks. Additionally, as mentioned before the weight of the flange as additional overburden is neglected for the diagonal tension failure mechanism. The only axial loading which is thus taken into account for this failure mechanism is the self-weight of the pier. It is therefore assumed that the diagonal tension failure is not a relevant failure mechanism for this case-study.
The schematization of the piers is visualized in Figure 6.7 for the positive direction. For the analysis the opening in pier number 5 and 7 is neglected since the compression strut doesn't intersect with the opening.

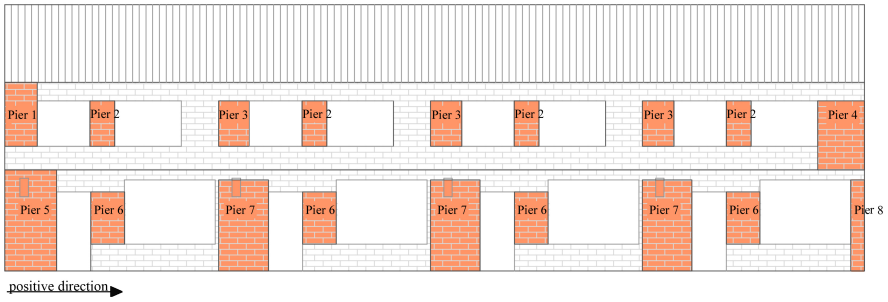

(a) Front facade

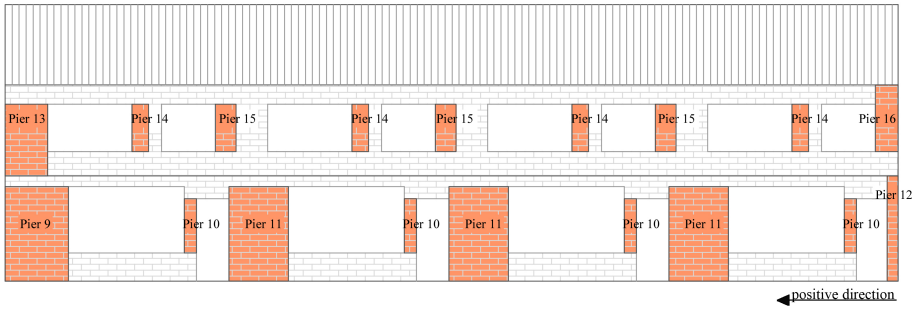

(b) Back facade

Figure 6.7: Schematization of the piers into the positive direction.

The piers are connected to each other by horizontal elements, the spandrels. The main function of the spandrel is to connect the piers and transfer the lateral loading. Similar as for the piers, the strength of the spandrel is determined by either the flexural or the shear strength. The NZSEE (2017) prescribes that if the piers are the governing elements in the analysis, the contribution of the spandrels for the global seismic capacity may be neglected. For this case study it is considered that the piers capacity is governing over the spandrels capacity. This may be derived from the following two reasons: firstly due to the fact that the reinforced concrete floor located at the first floor level intersects at the facade. This results into a spandrel at the first floor level which is continuous over the total length of the building and has a length of 25.57 meters, see Figure 6.8a. Secondly, above the openings wider than 1000 mm a concrete lintel, which is directly connected to the concrete floor acts as spandrel, the detail is visualized in Figure 6.8b. It is likely

to assume that the strength of the piers is governing over the strength of the concrete lintel and the continuous spandrel of 25.57 meter.

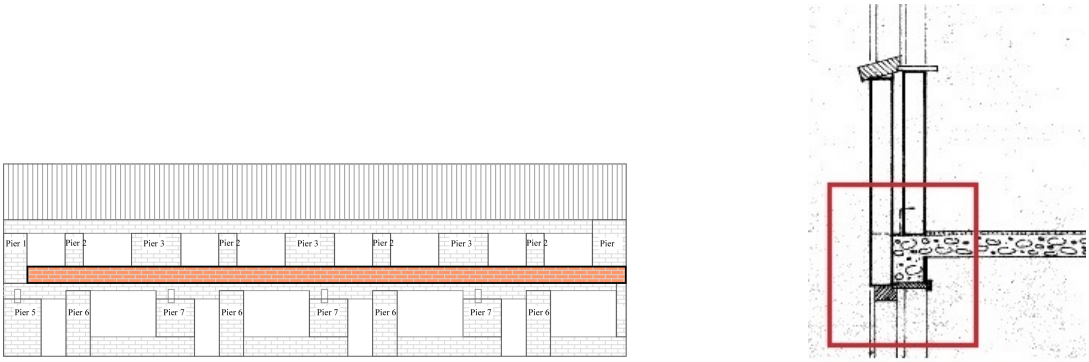

(a) Continuous spandrel

(b) Detail concrete lintel

Figure 6.8: Schematization of the spandrel.

6.3.1 Capacity positive direction

The piers are assumed to develop into the positive direction as visualized in Figure 6.7. The in-plane capacity of the piers on the first floor level is visualized in Figure 6.9 and the capacity of the piers located at the ground level in Figure 6.10. The governing failure mechanism for the piers is either shear splitting failure or flexural failure. The drift limit is defined in the NPR9998 similar for the splitting and flexural failure mechanism from which the obtained drift limits can be quite high with respect to the shear sliding failure mechanism.

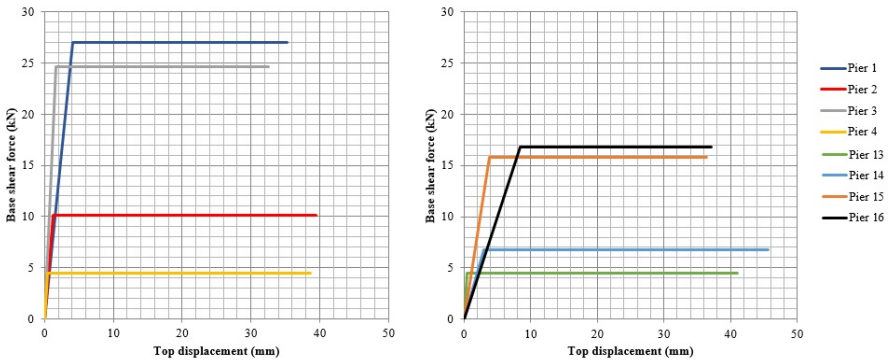

Figure 6.9: Shear capacity of the piers on the first floor level, left: front facade and on the right: the back facade.

The in-plane capacity of piers number 5 and 7 located on the ground level, are quite high with respect to the other piers of the structure. The flange of both pier number 5 and 7 are activated and taken into account as additional overburden. The activated flange supports the floor and a part of the dead load of the first floor level, consequently the axial loading on these piers is relative high and thus the shear capacity. The displacement capacity on the other hand is quite low in comparison to the other piers. As explained in Section 5.2.4, when the flange is in tension the stress increases at the compressed toe which results into failure of the pier in an earlier stage of the seismic loading. In other words, the displacement capacity of the pier decreases.

Furthermore, it can be determined from the graphs that the shear capacity of the front facade on

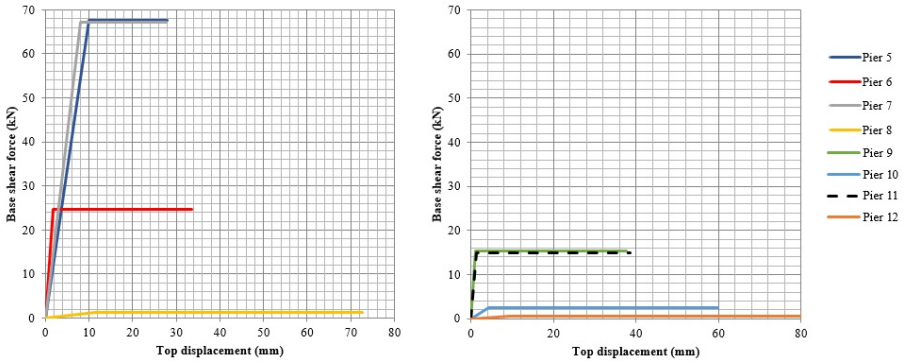

Figure 6.10: Shear capacity of the piers on the ground floor level, left: front facade and on the right: the back facade.

both the ground and first floor level is higher than the back facade. The piers on the front facade take advantage from the fact that the flanges are activated in contrast to the back facade, where no flange activation takes place. Consequently, the axial loading is higher on these piers which has a positive affect on the shear capacity.
Piers number 8, 10 and 12 have a relative low shear capacity with respect to the other piers, namely around the 2 kN. These piers don't have an additional overburden and thus the axial loading on these elements is minimal. Additionally, piers 8 and 12 are very slender, the height over width ratio is 6.6 and 9.7 respectively.
In Figure 6.11 the relation between the axial loading on top of the pier and the shear capacity of the element is visualized on the left. On the right the relation between the top displacement and the slenderness of the piers is visualized. The factor R^2 represents the cohesion between the variables, the value can be in the range from 0 to 100%. The coherence for the axial loading and the shear capacity is 96.5%. From the graph it can be derived that the increase of axial loading results in an increase of shear capacity.
As regards the relation between the slenderness of the pier and the top displacement, an increase of the slenderness results in a higher top displacement. This is related to the fact that an element with a higher slenderness has a lower stiffness which makes the element more flexible. The element is able to achieve higher displacements until failure.

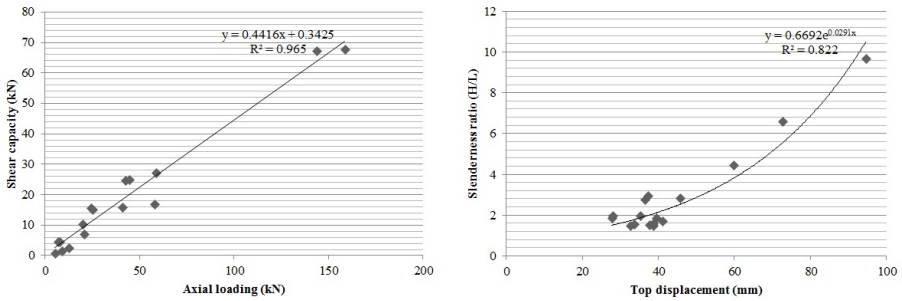

Figure 6.11: Regression analysis in the positive direction with on the left: the relation between the axial load and the shear capacity, and on the right: the relation between the displacement capacity and the slenderness ratio.

Since the piers are the only critical elements in the structure, due to the lack of spandrels, the in-plane capacity of the piers will be reached before the failure of the horizontal elements.
Two type of mechanisms can be distinguished in the case study, the top and bottom mechanism. In Figure 6.12 the total shear capacity is visualized for both the mechanisms. It can be observed that the displacement capacity of the piers is quite similar per mechanism due to the stable

plateau which develops for both the top and bottom mechanism. For the top mechanism the maximum displacement is 36.4 mm until the 50% strength decay is reached. The corresponding maximum base shear force is 241 kN. The maximum displacement of the bottom mechanism is 28 mm until the 50% strength decay is reached, with a maximum base shear force of 439 kN.

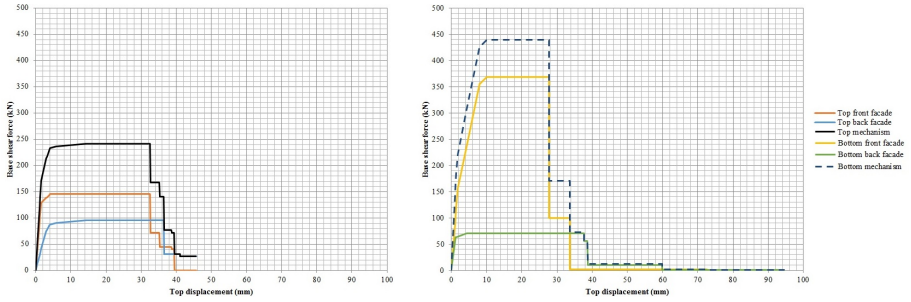

Figure 6.12: Total shear capacity per mechanism into the positive direction.

6.3.2 Capacity negative direction

The in-plane capacity for all the piers will now be determined for the negative loading direction. The schematization of the piers loaded into the negative direction is slightly different than for the positive direction. The development of the piers is visualized in Figure 6.13.

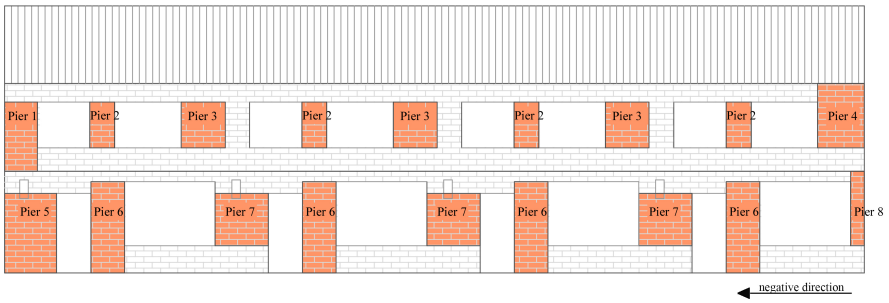

(a) Front facade

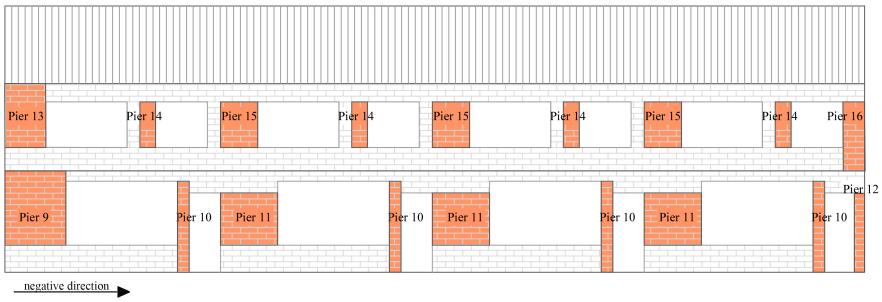

(b) Back facade

Figure 6.13: Schematization of the piers into the negative direction.

The in-plane capacity of the piers on the first floor level is visualized in Figure 6.14 and the capacity of the piers located at the ground level is visualized in Figure 6.15. Pier number 12 was

not taken into account since the overburden is very high with respect the the size of the pier. The pier fails due to the high overburden and its capacity is neglected.
Into the negative direction shear sliding failure is governing in part of the structure. When shear sliding failure is governing the shear capacity decreases due to the loss of cohesion. After the cracking it is assumed that the capacity is dependent upon the frictional component only.

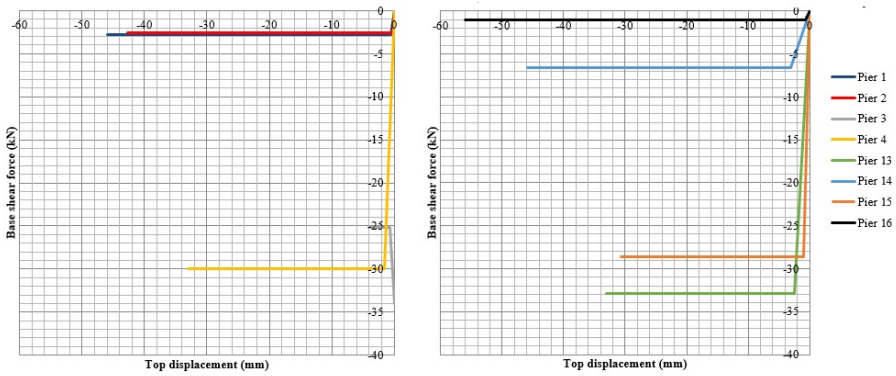

Figure 6.14: Shear capacity of the piers into the negative direction on the first floor level, left: front facade and on the right: the back facade.

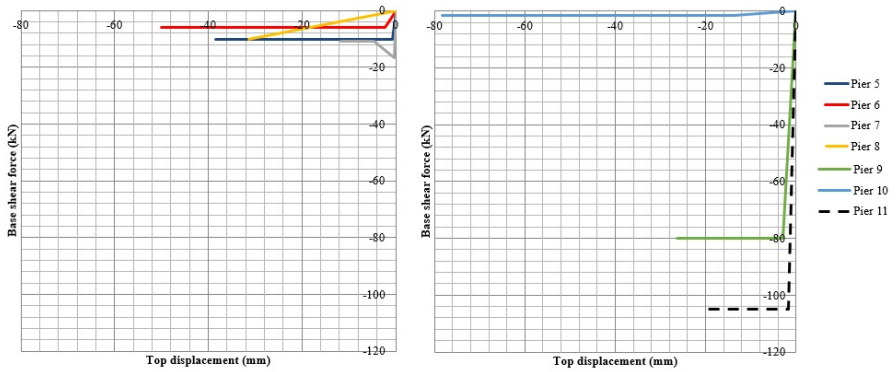

Figure 6.15: Shear capacity of the piers into the negative direction on the ground level, left: front facade and on the right: the back facade.

As regards the in-plane capacity pier number 9 and 11 have a quite high capacity with respect to the other piers. For both the piers the flange is activated into the negative direction which has a positive affect on the shear capacity. The overburden originating from the activated flanges is quite high since it supports the floor and part of the load of the first floor level. The slenderness (H/L) of both the piers is around 1, the piers are both relative squat piers. From the graphs in Figure 6.15 it can be derived that the capacity of the back facade is higher than the front facade. In the positive direction the flanges on the front facade were activated, in the negative direction the flanges on the back facade are activated.
Similar as for the positive direction pier 10 and 12 have a relative low shear capacity due to the high slenderness and low axial load. Pier 8 is also very slender and does not yield before failure due to the high slenderness and high axial loading. The coherence observed in Figure 6.16 are in line with the observed coherence into the positive direction.
In Figure 6.16 the relation between the axial loading on top of the pier and the shear capacity of the element is visualized on the left. On the right the relation between the top displacement and the slenderness of the piers is visualized. The coherence between the axial loading and the shear capacity is 85%. The coherence between the top displacement and the slenderness ratio is 92%.

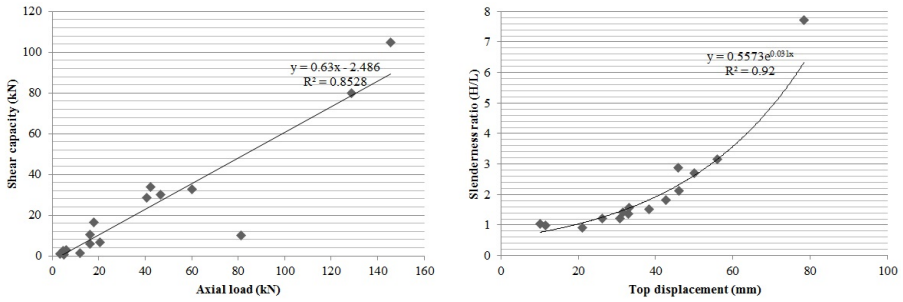

Figure 6.16: Regression analysis in the positive direction with on the left: the relation between the axial load and the shear capacity, and on the right: the relation between the displacement capacity and the slenderness ratio.

One of the outliers which can be observed in the graph is the from pier 8. The pier has quite a high axial load on top of the pier, however the pier is very slender (H/L=10). Due to the high slenderness the pier its capacity is relatively low despite the fact that there is a high axial load on the element.

Finally, the total base shear capacity of the mechanism can be determined this is visualized in Figure 6.17. From these graphs it can be observed that the plateau is not that constant for the top mechanism. This is related to the displacement capacity of the individual piers. Pier 3 has a relative high shear capacity, but low displacement capacity with respect to the other piers. Failure of pier 3 results in a strength decrease of 28% in the top mechanism, hereafter a second stable plateau is reached. The 50% strength decrease is reached at the displacement of 30 mm. After the first strength decrease it is assumed that there is no dynamic instability in the structure. The floor spans between the transverse walls and is still able after failure of pier 3 to redistribute the lateral loading over the piers.
The capacity of the bottom mechanism is relative high with respect to the bottom mechanism. This is related with the flanges which are activated into the negative direction and results in a higher shear capacity of the individual elements which have an activated flange. However, the displacement capacity of the mechanism is relative low. After a displacement 21.1 mm the 50% strength decay is reached. The shear capacity of the mechanism decreases rather quickly after this point.

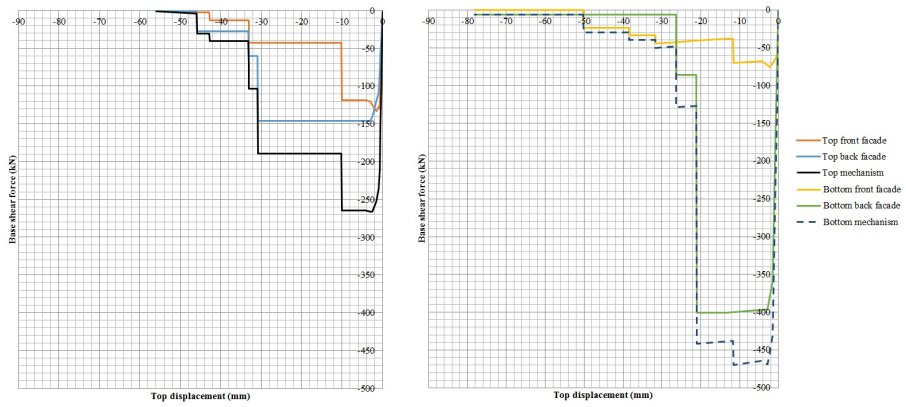

Figure 6.17: Total shear capacity negative direction.

6.3.3 Drift limits

In the NPR9998 global limitations have been defined for the inter-storey drift and the maximum displacement at the effective height. If these drift limits are exceeded, the NC limit state is reached. The drift limits as defined by the NPR9998 are summarized in Table 3.1.

The top mechanism into the positive direction is the governing mechanism for this case study. At the moment of failure, the shear splitting failure mechanism is governing in most of the piers. The splitting failure mechanism is locally determined as a ductile failure mechanism which can obtain relative high drift limits, comparable with the flexural failure mechanism. However, globally the splitting failure mechanism is determined as a brittle mechanism by the NPR9998 which can obtain relative low drift limits. The inter-storey drift limit is 0.6% which would result into a top displacement of only 15.6 mm with the top mechanism as governing mechanism. The maximum displacement at the effective height is determined with a drift limit of 0.4% for brittle failure and results into a displacement of 22.4 mm. Concluding, the top displacement of 15.6 mm is the ultimate displacement of the structure according to the NPR9998, the NC limit state is reached here.

However, this is not consistent with the drift limit which is defined locally for the splitting failure mechanism. Piers in which the splitting failure mechanism is governing can obtain high drift limits, however if the pier fails due to splitting of the bricks, failure is quite brittle. Since the failure mechanism can obtain high drift limits according to the NPR9998 (similar as for a ductile response), it would be a logical consequence that the mechanism its response is determined at global level as a ductile mechanism as well. If the response would be determined ductile at global level an inter-storey drift limit of 1.5% can be obtained, the maximum displacement would be 39 mm. In this case the maximum displacement which is obtained after a 50% strength decay of the top mechanism is governing (36.4mm).

Another critical point is that the global drift limits as described above are not initially intended for the use of the SLaMA method or EFM. The global drift limits are intended for the use of Finite Element Modelling (FEM) analysis. In FEM the drift limit can't be implemented at local level for each element, and therefore the global drift limits are intended. However, it is prescribed by the NPR9998 that the global drift limits should be taken into account for the SLaMA method and EFM as well.

Due to the inconsistent definition by the NPR9998 a final calculation will be made in which the shear splitting mechanism is also locally determined as brittle failure mechanism. The drift limit is locally set at 0.75% which is similar as the drift limit of the shear sliding mechanism. In Table 6.6 an overview is given for the determination of the displacement capacity of the top mechanism locally and globally. In Figure 6.18 the top mechanism is visualized if the splitting failure is locally determined as a brittle failure mechanism. After a strength degradation of 47% a new plateau can be observed in the base shear force. With the high strength degradation and failure of the corresponding piers the NC limit state is probably reached at this point concluding from an engineering point of view. Model 3 is not taken into account in the target displacement method since the results vary not that much from model 2.

Table 6.6: Failure response local and global per model.

	Model 1		*Model 2*		*Model 3*	
	Local	**Global**	**Local**	**Global**	**Local**	**Global**
Ductile	✓	✓	✓			
Brittle				✓	✓	✓

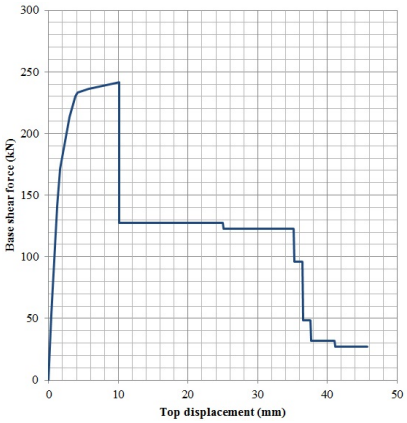

Figure 6.18: Top mechanism if the splitting is locally determined as brittle mechanism.

6.3.4 Capacity spectrum method

In the final step the capacity of each mechanism is compared to the seismic inelastic demand with the target displacement method. The mechanism with the lowest lateral shear capacity is governing which is the top mechanism loaded into the positive direction. Failure will thus be concentrated at the top floor level. The base shear force for this mechanism is 243 kN after the bilinearization.
As mentioned in the previous subsection the predominant failure mode at the moment of failure is splitting failure which response is inconsistently defined in the NPR9998. In Figure 6.19 both the responses are visualized. The difference between both the responses is quite significant.
For the mechanism where a ductile response is assumed (model 1) at both local and global level, the displacement capacity is larger than the displacement demand. The structure satisfies the criteria as defined by the NPR9998. The maximum lateral displacement of the mechanism is 36.4 mm. This in contrast to the model where a brittle response is assumed for the mechanism at global level (model 2), the maximum lateral displacement would be limited until 15.6 mm. The displacement demand is larger than the capacity and therewith the structure would not satisfy the criteria.

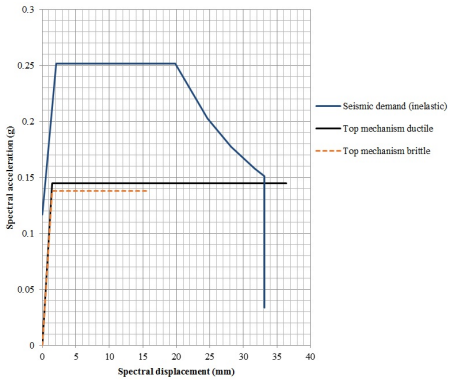

Figure 6.19: Determination of the target displacement.

6.4 EQUIVALENT FRAME METHOD

In 3Muri a model is created in which a NLPO analysis is executed in order to describe the seismic behavior of the structure based upon the EFM. The setup of the 3Muri model and the limitations of the model will be explained here. Due to the limitations discovered in Section 5.4 it is chosen to focus on the Eurocode 8 as leading guideline. The results obtained with this guideline will be discussed more extensively. Finally the model will also be created with the NPR9998-2018 as guideline, the focus for this model is mainly on the global results. The following results are obtained with version 12.2.1.4 of 3Muri.

Walls

For the models which are created in 3Muri, decisions have been made as regards the modelling process. It is not possible in 3Muri to create cavity walls, however as described before the outer leaf doesn't contribute to the in-plane capacity of the structure. It is therefore chosen for the model in 3Muri to neglect the outer leafs.
Secondly, to be consequent with the SLaMA model, only the walls which are relevant as a flange for the in-plane loaded walls will be modelled, this corresponds to the plan as visualized in Figure 6.2. The party walls of 70 mm which have no significant contribution to the in-plane strength of the structure are neglected. Finally, the storage room is not modelled since the contribution to the load bearing capacity with respect to the terraced house can be neglected. The choices which are made, are all consistent with the choices made in the SLaMA

Lintels

A second limitation in 3Muri is that is not possible to create the lintels above the openings which are present in the terraced house above each opening which has a larger span than 1000 mm. As explained before the lintel and the pier are connected to the same node and the lintel can be seen as some kind of reinforcement. Due to the large openings in combination with the irregularity in the facade, 3Muri can not link the lintel to the similar node as the pier, see Figure 6.20. In this figure it is visualized that the lintel (T153) cannot connect with the pier (E34). Therefore it is chosen to exclude the lintel so that the openings can be modelled accurate.

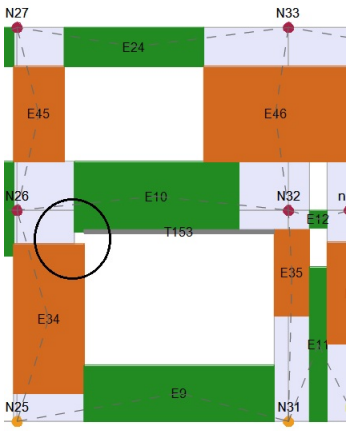

Figure 6.20: Missing connection in the mesh.

Loads

As regards the roof, this is modeled as a surface and no distinction is made between the line and point loads. The surface load is in the total model seen as a line load which is supported by the party walls and the facade walls. The applied surface loads are similar as was applied for the SLaMA method which are presented in Table 6.3.

Constitutive law

Since the Eurocode 8 is used as guideline in the 3Muri model, a choice is required between the Mohr-Coulomb and the Turnsek Cacovic criteria to be used during the modelling process. It is chosen to use the Mohr-Coulomb relation with as a limitation of the shear strength limit:

$$f_{vlim} = 0.1 \cdot f_b \tag{6.2}$$

The shear strength limit in this case is thus 1.2 N/mm^2. It is chosen to use the Mohr-Coulomb criteria over the Turnsek Cacovic criteria since the latter is more applicable to irregular patterns which is not applicable for this case study as explained in Section 5.4.1.

The meshing options

During the modelling process the identification of the individual elements into the belonging equivalent frame model influences the overall behavior and capacity of the structure. For the schematizing of the facade into the individual components it is chosen to create two models. For the first model the structure is modelled exactly similar as the case study. This is visualized in Figure 6.21a, it can be observed that the meshing around the smaller opening is quite irregular which can result in a significant difference in the base shear capacity. Hence, a second model will be created as comparison in which the smaller window in the front facade is neglected, similar as was done in the SLaMA method. In Figure 6.21 the schematization of the two different models is visualized. Finally, it is chosen to change the strength decay limit of 20% to 50% in order to have a more fair comparison with the NPR9998.

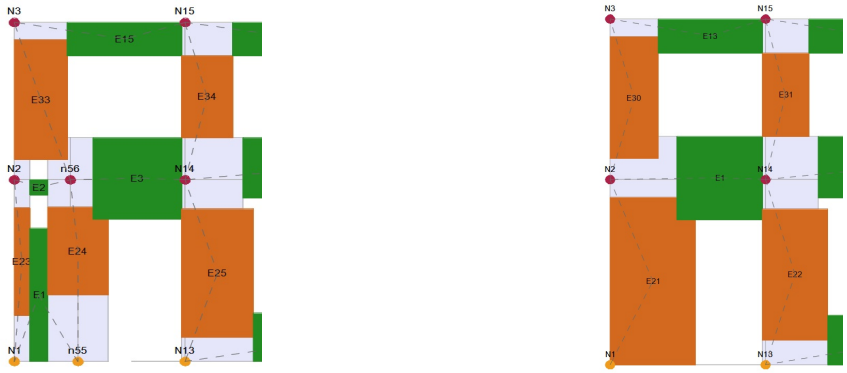

(a) Model 1: window included in the mesh

(b) Model 2: window neglected in the mesh

Figure 6.21: Equivalent frame schematization.

6.4.1 Model 1: window included in the mesh (EC8)

Capacity positive direction

The pushover curve for the capacity of the structure in the positive direction is visualized in Figure 6.22. The maximum displacement which can be obtained is 22.4 mm with a base shear force in the positive direction of 156 kN. From 14.4 mm a strength decrease is visible in the pushover curve which is due to shear failure of the piers mainly concentrated at the ground floor level.

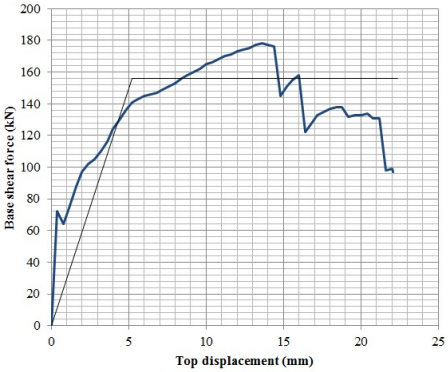

Figure 6.22: Pushover curve model 1 into the positive direction.

In Figure 6.23 the governing failure mechanisms at failure of the structure are visualized, in Figure 5.15 the legend is visualized. Shear failure in combination with shear damage is the governing failure mechanism for most of the piers. Most of the piers on the first floor level remain undamaged in contrast to the piers at the ground floor level which all experience either flexural damage or shear failure. All the spandrels experience flexural damage.

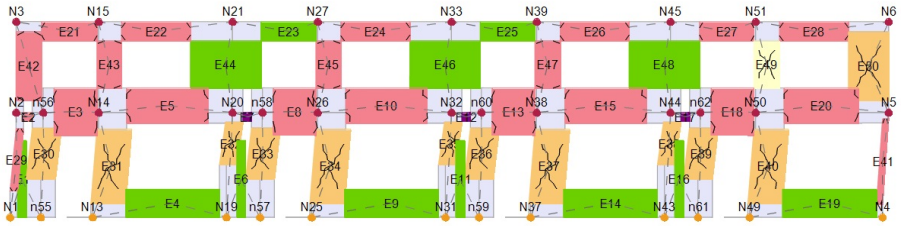

(a) Front facade

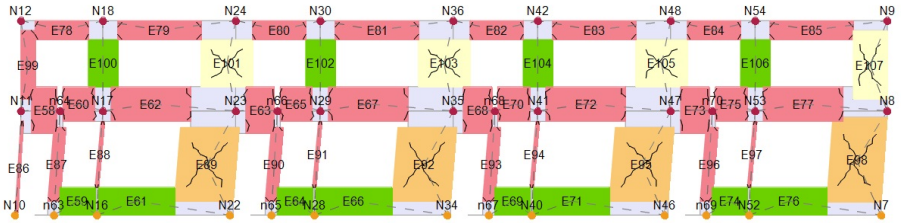

(b) Back facade

Figure 6.23: Failure mechanisms model 1 into the positive direction.

To create a better understanding of the behavior of the individual elements, the axial load distribution of the piers which experience damage or failed during the analysis are analyzed. In Figure 6.24 the axial load distribution is shown for these elements and in Table 6.7 the damage and geometry of the pier is visualized. From the graph it can be derived that Element 89 and

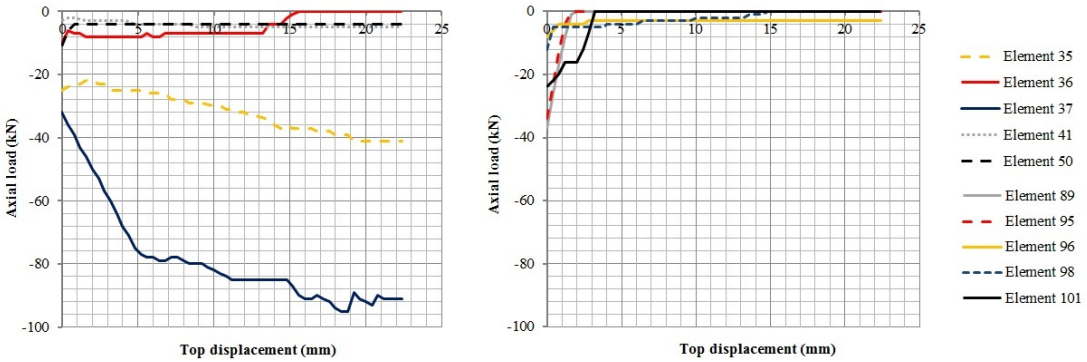

Figure 6.24: Axial load distribution per element for the positive direction.

Table 6.7: Damage level per pier.

Element	Failure	H/L
35	Shear failure	2.45
36	Shear failure	1.74
37	Shear failure	2.13
41	Flexure damage	14
50	Shear failure	1.71
89	Shear failure	1.25
95	Shear failure	1.25
96	Flexure damage	6.07
98	Shear failure	1.55
101	Shear damage	0.90

Element 95, which are both located at the back ground facade, behave quite brittle. After the first cracks in the pier, the axial load distribution in the pier decreases rather quickly to 0 kN. The quick decrease of axial load distribution also applies for Element 101, located at the back facade at the first floor level. The other elements which also experience shear damage or failure, are still quite constant in their axial load distribution after cracking.
For the determination of the ultimate displacement capacity of a single element in 3Muri, it is checked whether the NC limit state is reached. The ultimate displacement of an element is expressed as drift limit. In the NEN-EN 1998-3 it is recommended in the informative annex C to use the following drift limits:

$$\theta_{nc;flexure} = \frac{4}{3} \cdot 0.008 \cdot \frac{H_0}{l_w} \tag{6.3}$$

$$\theta_{nc;shear} = \frac{4}{3} \cdot 0.004 \tag{6.4}$$

The drift limit in 3Muri can be determined with Equation 5.10.
As regards the drift limitation of the piers, in most of the piers the shear failure was the governing failure mechanism. The belonging drift limit is 0.53% for these elements. If the drift limit or ultimate strength of an element is exceeded, no more shear forces can be transferred through the element. The element can be considered as a strut with no shear or bending strength, however the axial loading can still be transferred through the element (Lagomarsino et al., 2013).
In Figure 6.25 the relation between the shear force and drift limit of element 35 and 89 is visualized. In both the elements shear failure was governing, it is expected that the elements fail after

exceeding the drift limit of 0.53%. However, element 35 fails at a drift limit of 0.73% which is higher than the limit as defined in the program. Element 89 on the other hand fails at a drift limit of 0.053% which is ten times lower than the defined limitation.

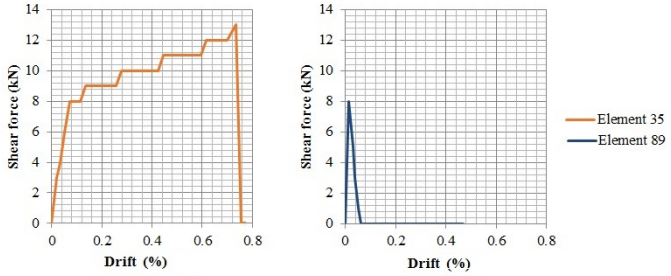

Figure 6.25: Relation between the shear force and the drift limit for Element 35 and 89.

Generally failure of the element is determined by the drift limit (Lagomarsino et al., 2013). However, part of the elements exceed the drift limit as illustrated in Figure 6.25. This can be related to the modelling approach of 3Muri which is focused on macro level.
Additionally, the geometry of the elements also affect the drift limit of the piers. The example which was given for element 89 illustrates the brittle behavior which is related to the fact that the element is quite squat (H/L=1.25). This behavior can be observed for more elements which have a squat geometry.

Capacity in the negative direction

The pushover curve for the capacity of the structure in the negative direction is visualized in Figure 6.26. A maximum displacement of 22.5 mm can be obtained with a base shear force capacity of 382 kN.

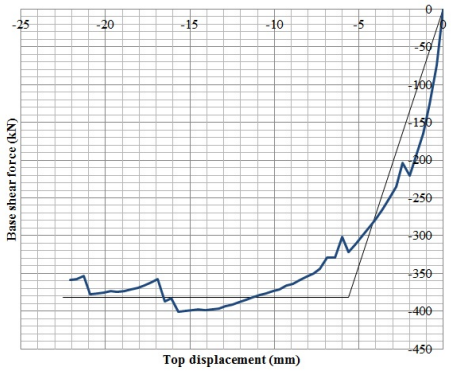

Figure 6.26: Pushover curve model 1 into the negative direction.

In Figure 6.27 the failure mechanisms at the end of the analysis per element are visualized. Similar as for the positive direction, shear failure in combination with shear damage is governing for most of the piers, but where in the positive direction 15.9% of the piers remained undamaged, in the negative direction only 6.8% was undamaged. Additionally where in the positive direction 36% failed due to shear failure, in the negative direction 45.5% failed due to this mechanism. Most of the piers which failed are located at the front facade at both the ground and first floor level. The higher percentage of elements which experience failure is related to the development of the in-plane capacity which is twice as high in the negative direction than in the positive

direction. The higher base shear force capacity into the negative direction can be an indication of a higher percentage of flanges which are activated into this direction.

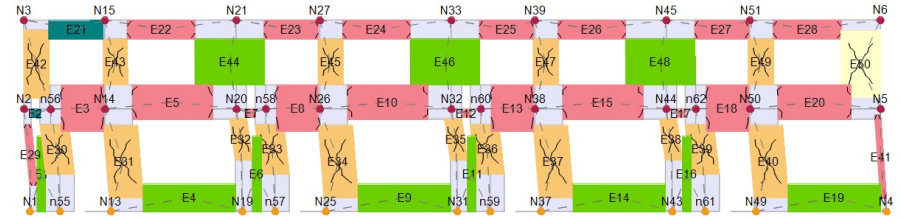

(a) Front facade

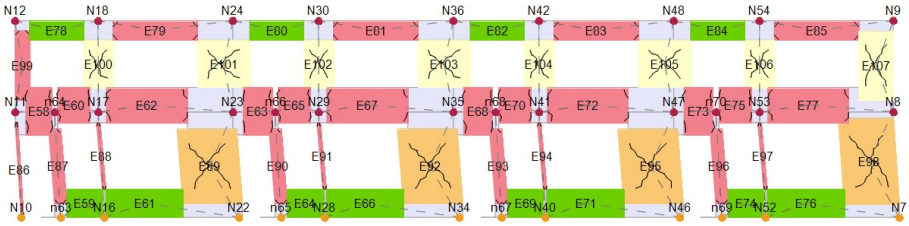

(b) Back facade

Figure 6.27: Failure mechanisms model 1 into the negative direction.

In order to verify if the activation of the flange is taken into account the axial load distribution of element 31 and 47 is analyzed. If the structure is loaded into the positive direction, element 47 only experience bending damage and element 31 shear failure. Both the elements fails due to shear failure in the negative direction. In Figure 6.28 the axial load distribution of these elements is visualized. It can be derived from these graphs that the axial loading increases when these elements are loaded into the positive direction in contrast to the negative direction where the axial load decreases. Both the elements have a flange which is activated into the positive direction and thus works as additional overburden. When loaded into the negative direction the flange is not taken into account. The activation of the flange is thus taken into account.

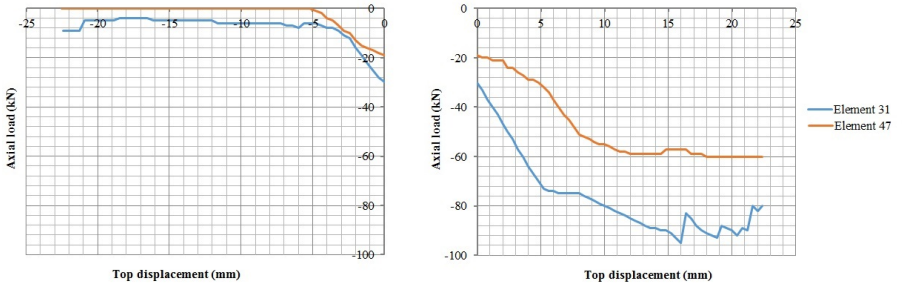

Figure 6.28: Activation of the flange into the positive direction.

In Figure 6.29 the relation between the shear force and the drift limit for element 31 and 47 is visualized. Element 31 fails at a drift limit of -0.581% which is higher as the limit defined in the program. Element 47 fails at a drift limit of -0.34% which is lower than the defined limit. The height over width ratio is not as squat, namely around the 2 for both the elements. The elements don't behave as brittle as the elements visualized in Figure 6.25.

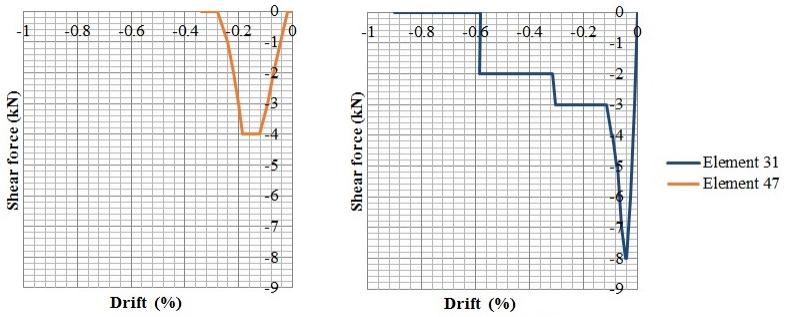

Figure 6.29: Relation between the shear force and the drift limit for Element 31 and 47.

6.4.2 Model 2: window neglected in the mesh (EC8)

In the second model the small window in the facade is neglected. Due to the neglection of the window, one single pier is found by 3Muri, as was visualized in Figure 6.21b.

Capacity positive direction

The pushover curve of the model in the positive direction is visualized in Figure 6.30. The base shear force of the model is 326 kN and is 55.8% higher with respect to the first model. The ultimate top displacement is 35.4 mm and is 13 mm higher than model 1.

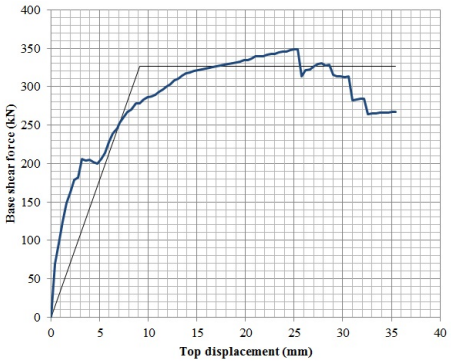

Figure 6.30: Pushover curve positive direction.

From Figure 6.31 the damage to the elements can be observed at failure of the structure.
If we compare the failure mechanism of this model with the previous model, it can be observed that more elements are damaged or failed after the analysis in comparison to model 1. In this model the piers are able to develop their in-plane capacity further before the 50% strength decay is reached. Another development which can be observed is that most of the spandrels has failed due to flexural failure in this model. This is also in contrast to model 1 in which only flexural damage was observed.
In order to create a better understanding about the load distribution between the spandrels and the piers, the load distribution of these elements is analyzed. In Figure 6.32 the relation between the shear force, axial loading and the displacement for adjacent elements in the front facade is visualized. From the graphs it can be observed that after elements 14 and 16 fail and the load distribution in these elements is zero, element 15 is "activated". After the activation, load distribution can be observed in the element until failure. The spandrels do not contribute significantly to the shear capacity of the structure, but it can be observed that its main function is to transfer the lateral load. Additionally, it can be observed that part of the spandrels has failed

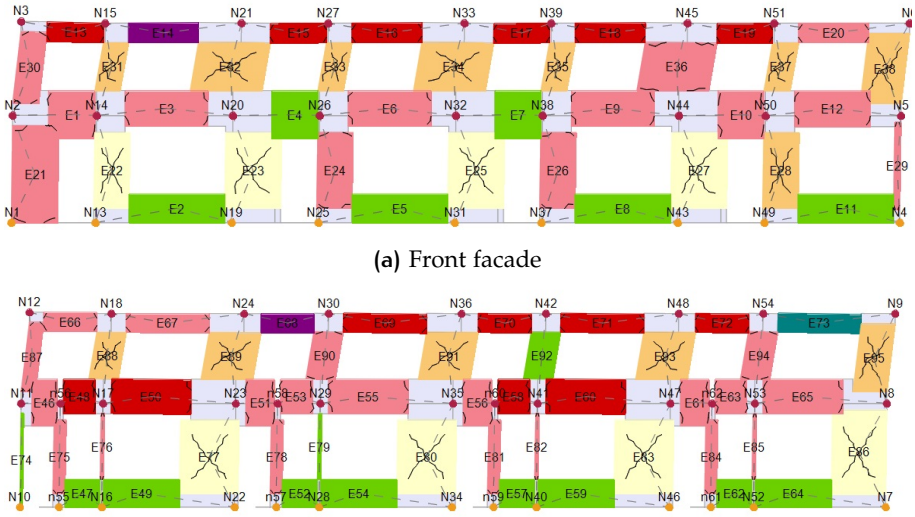

(a) Front facade

(b) Back facade

Figure 6.31: Failure mechanisms positive direction.

before global failure. However, the structure was still able to withstand the seismic load. This suggests that the failure of the spandrels don't have a significant affect on the global capacity. Additionally, it indicates that the floors itself is still able to redistribute the lateral load.

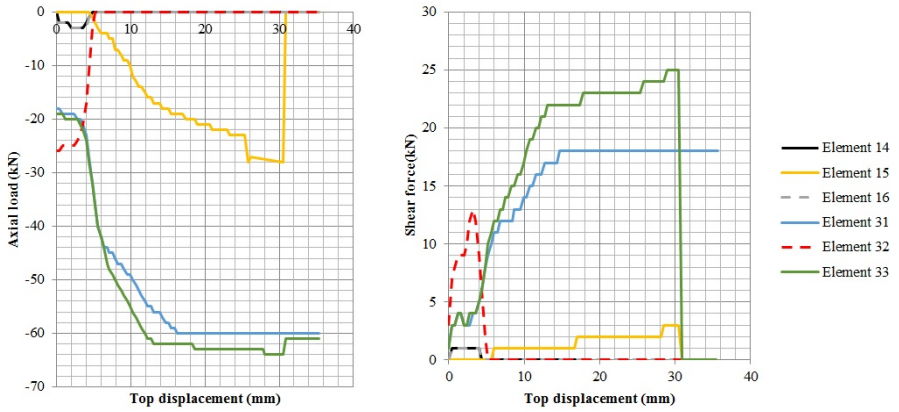

Figure 6.32: Relation between the shear force, axial loading and the displacement.

A final interesting point it the difference of the overall capacity of this model in which the small window is neglected with respect to model 1 in which the small window is taken into account. This is related to the development of the shear force capacity in the adjacent piers. If we compare the shear capacity of element 32 and 33 from model 1 as visualized in Figure 6.23a with element 23 from model 2 visualized in Figure 6.31a the difference is quite significant. The capacity of element 32 and 33 in model 1 is 78% lower with respect to element 23 in model 2.

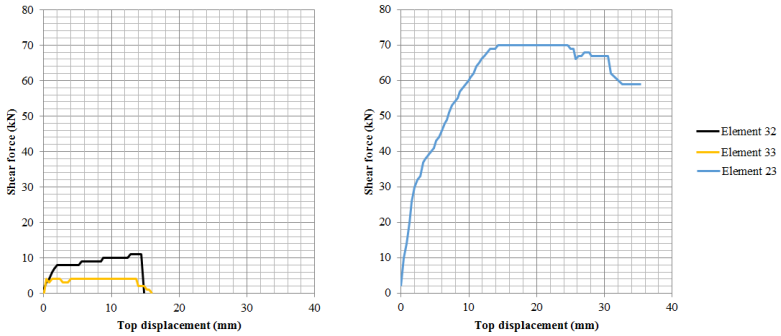

Figure 6.33: Comparison of the development of the shear force, left: development of element 32 and 33 in model 1 and on the right: development of element 23 in model 2.

Capacity negative direction

The pushover curve of the model in the negative direction is visualized in Figure 6.34. The base shear force is -318 kN and is 16.7% lower than the first model. The ultimate top displacement of the model is 22.3 mm, and is nearly similar as the first model. In Figure 6.35 the failure mechanisms per facade in the negative direction are visualized at the end of the analysis.

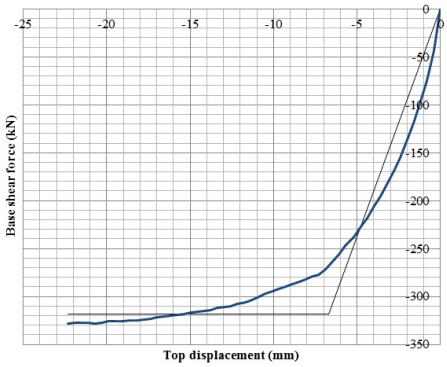

Figure 6.34: Pushover curve negative direction.

From Figure 6.35 it can be observed that the damage is mainly concentrated at the ground floor level. Most of these piers failed due to shear failure. In the front facade also flexural failure can be observed.

The lower base shear capacity of this model is not as expected. With the increased width of the elements from which the small window is neglected (E21, E23, E25 and E27), it would be expected that the shear capacity would increase. The elements its base shear capacity did increase into the positive direction as visualized in Figure 6.33. The flange is not activated into the negative direction, however a similar difference between the models would be expected.

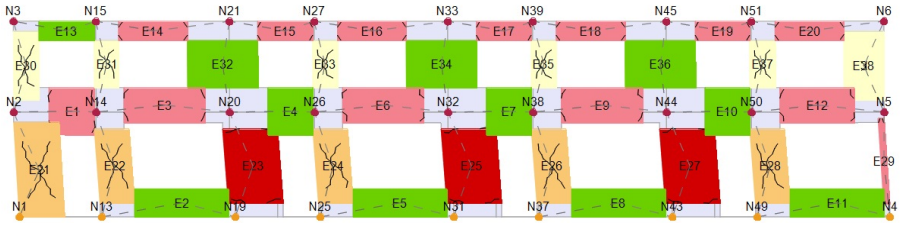

(a) Front facade

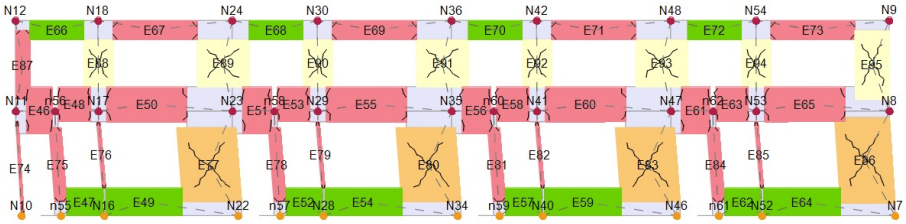

(b) Back facade

Figure 6.35: Failure mechanisms negative direction.

6.4.3 Model 3: window neglected in the mesh (NPR9998-2018)

As introduced in the begin of this section the model will also be made in 3Muri according to the NPR9998-2018 as guideline. The results are presented here briefly. In Figure 6.36a the pushover curve obtained with the NPR9998 is visualized for both the positive and negative direction. An interesting point is the development of the base shear capacity and the corresponding failure mechanisms. The structure didn't reach the 50% strength decay after a displacement of 80 mm in both the positive and negative direction.

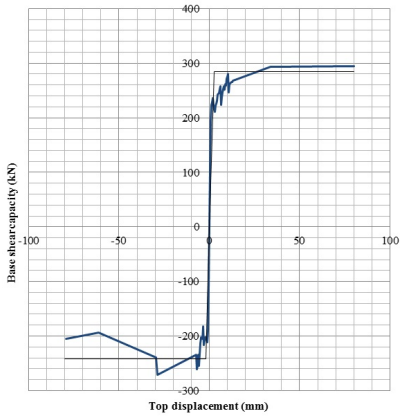

(a) Pushover curve 3Muri-NPR9998-2018

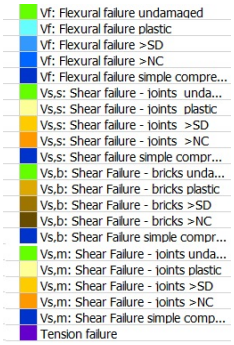

(b) failure chart of 3Muri NPR9998-2018

Figure 6.36: 3Muri model with NPR9998-2018 as guideline.

In Figure 6.37 the failure mechanisms at the end of the analysis are visualized into the positive direction (the structure has not failed at this point according to the software).
In the pushover curve a very small strength decay can be observed at a relative early stage of the analysis, part of the structure fails here due to diagonal tension failure. As explained in Section 6.3, diagonal tension failure should not be governing over the shear sliding failure mech-

anism. The strength of the bricks is higher than the mortar which results in shear sliding to prevail over diagonal tensile failure.

Based upon the development of the failure mechanisms and the pushover curve it is questionable if the results obtained with this guideline are reliable. At the end of the analysis 61% of the back facade has failed due to diagonal tensile failure. Additionally, 88% of the bottom back facade has failed. It is seems very unlikely that even though such a large percentage of the piers has failed that the structure is still dynamically stable. Moreover, due to the fact that the diagonal tensile failure mechanism is a brittle failure mechanism which causes a quick decrease of both the strength and stiffness in an element (NZSEE, 2017).

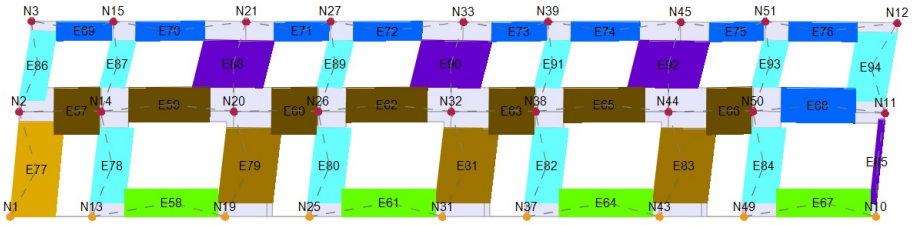

(a) Front facade

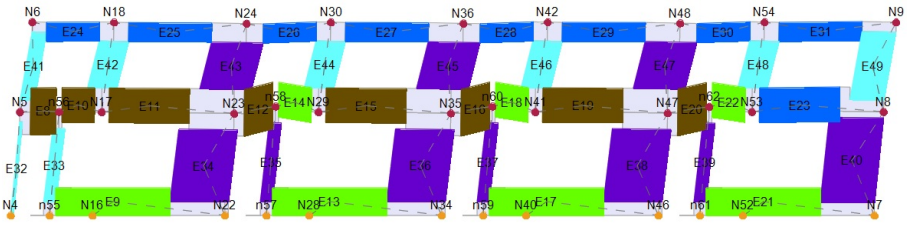

(b) Back facade

Figure 6.37: Failure mechanisms positive direction obtained with the NPR9998-2018 as guideline.

6.5 COMPARISON OF THE RESULTS

In this section the outcomes of the SLaMA method are compared with those of the three 3Muri models which are obtained in the previous sections. The choice is made to neglect model 1 created with 3Muri (EC8) in which the small toilet window is taken into account. The reason for this is that the mesh of model 1, in which the window is taken into account, doesn't seem correct since the compression strut doesn't intersect with the window. Model 2, in which the window is excluded, is a more accurate representation of the case study. The meshes are visualized in Figure 6.21. Additionally the 3Muri model with the NPR9998-2018 as guideline will also be taken into account for the comparison. It should be noted that the reliability of this model is questionable as explained in Section 6.4.3.
An additional comparison is made with DIANA FEM which is obtained by Deniz Dalgic et al. (2017). It must be noted that limitations during the modelling process resulted into a low displacement capacity. The results obtained with FEM suggests that the ground storey is the weakest storey (soft storey) (Deniz Dalgic et al., 2017). In Figure 6.38 the pushover curve obtained with the different models is visualized. It must be noted that the global drift limitations for the NC limit state given by the NPR9998 are not taken into account. In Table 6.8 the obtained outcomes are summarized.

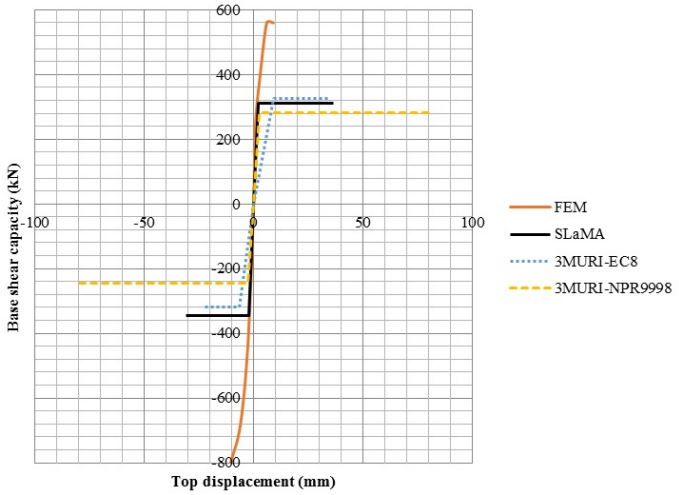

Figure 6.38: Pushover curve obtained with SLaMA, FEM, 3Muri-EC8 and 3Muri-NPR9998 for the Martini type K assessment.

Table 6.8: Obtained outcomes with SLaMA, FEM, 3Muri-EC8 and 3Muri-NPR9998 for the Martini type K assessment.

	Dir.	SLaMA	3Muri-EC8	3Muri-NPR9998	FEM
Base shear (kN)	+	312	326	283	560
	-	-346	-318	-244	-800
Displacement (mm)	+	36.4	35.4	81.1	9
	-	-31	-22.3	-79.5	-10.5

What is interesting in this figure is the difference between the initial stiffness of the SLaMA approach and 3Muri-NPR9998 and on the other hand the 3Muri-EC8 model. The initial stiffness of the 3Muri-NPR9998 model and the SLaMA approach are considerably higher than the 3Muri-EC8 model. This indicates that the 3Muri-NPR9998 and SLaMA model which use the NPR9998 as guideline are stiffer than the 3Muri-EC8 model. This can also be derived from the period of the equivalent SDoF system (T^*) which differs. The main difference between the 3Muri models are

the material properties. In the EC8 model the drift limits are required for the shear and flexural failure mechanism, in contrast to the NPR9998 in which no drift limits can be defined. On the other hand in the NPR9998 the shear friction coefficient is required, however this coefficient is not included in the EC8.

In Table 6.9 the reaction forces in the vertical direction are presented for both the models at the begin and end of the analysis in 3Muri. The tabel shows that the distribution of the gravity load in both the models is nearly equal. This suggests that the stiffness of both the front and back facade is equivalent for both the models. However, the 3Muri-NPR9998 model reacts stiffer during the analysis. According to Lagomarsino et al. (2013) the elastic stage of an element in 3Muri is determined by both the shear and flexural stiffness. The stiffness dependents upon the geometry and the mechanical properties of an element. A possible explanation for the different stiffness's is related with the governing failure mechanisms in both the models. In the 3Muri-NPR9998 model, the diagonal tensile failure mechanism is governing. A part of the structure fails in this model in a relative early stage of the analysis, as explained in Section 6.4.3. Consequently, the inelastic stage is earlier reached in this model, this in contrast to the 3Muri-EC8 model.

Table 6.9: Reaction forces in the facades (kN).

	Wall	3Muri-EC8	3Muri-NPR9998
Begin analysis	Back	1164	1196
	Mid	929	950
	Front	809	827
End analysis	Back	1010	1072
	Mid	659	659
	Front	1243	1248

An interesting aspect of the internal force distribution in 3Muri is observed if the openings in the transverse wall are deleted. By neglecting these openings an additional node is added by the software to these walls as visualized in Figure 6.39. In Table 6.10 the reaction forces are presented of the new models with the new mesh. It is noteworthy that the reaction forces at the front facade are significantly higher in the 3Muri-NPR9998 model than the 3Muri-EC8 model at the end of the analysis. This indicates the decrease of both the strength and stiffness in the elements located at the back facade due to the diagonal tension failure mechanism. However the influence of the redistribution of the internal vertical reaction force is barely visible in the global seismic capacity. The base shear capacity increases with approximately 10% for both the 3Muri-EC8 and the 3Muri-NPR9998 models with respect to the original model.

(a) Original mesh, with openings **(b)** New mesh, without openings

Figure 6.39: Mesh of the transverse walls in the model, by deleting the windows 3Muri generates an additional node.

Finally the pushover curves obtained in Figure 6.38 are compared to each other. It must be noted that if the global drift limits, as defined by the NPR9998 are taken into account, the displacement

Table 6.10: Reaction forces if neglecting openings (kN).

	Wall	3Muri-EC8	3Muri-NPR9998
Begin analysis	Back	237	242
	Mid	2410	2468
	Front	307	310
End analysis	Back	123	97
	Mid	2471	1818
	Front	346	1115

capacity of SLaMA would be limited at 15.6 mm (inter-storey drift of 0.6%). The displacement capacity of the 3Muri-NPR9998 model would be limited at 22.4 mm (drift limit of 0.4% at h_{eff}). However, as explained in Section 6.3.3 these global drift limits are initially intended for the use of FEM and not for SLaMA and the EFM. Therefore it is chosen to neglect the global drift limits here.

The results obtained with SLaMA and 3Muri-EC8 into the positive direction are nearly similar as regards the displacement and base shear capacity.
The displacement capacity of the 3Muri-EC8 model into the negative direction has a deviation of 28% with respect to SLaMA. This is related to the drifts which can be obtained with the shear failure mechanism as defined in the Eurocode 8. In the NPR9998 a distinction is made between the shear splitting failure mechanism and the shear sliding mechanism. As explained before, with the splitting mechanism relative high drifts can be obtained which are similar to the flexural failure mechanism. The splitting failure mechanism was predominantly governing in the SLaMA method, resulting into a relative high global displacement capacity. In the 3Muri-EC8 model only the shear sliding failure mechanism is taken into account. With this mechanism relative low drifts can be obtained with respect to the splitting mechanism. This explains the large deviation as regards the displacement capacity.
The 3Muri-NPR9998 model its displacement capacity is significantly higher than the other approaches, however as explained before the reliability of this model is questionable. It is not clear if the drift limits are correct implemented into the software if the NPR9998-2018 is used.

The base shear capacity is nearly similar for the 3Muri-EC8 approach and the SLaMA method into the positive direction. The base shear capacity into the negative direction of 3Muri-EC8 deviates 8% with respect to SLaMA. With the 3Muri-NPR9998 model the base shear capacity deviates 29% into the negative direction with respect to SLaMA. Into the positive direction the difference is smaller, namely a deviation of 9% with respect to SLaMA.

A final interesting point is the difference in both the displacement capacity and the base shear capacity of the DIANA model with respect to the 3Muri models and the SLaMA method. The base shear capacity of FEM is significantly higher which can be related to the out-of-plane behavior which is neglected in the 3Muri models. Additionally, in the SLaMA model it is only verified if the transverse walls have sufficient out-of-plane capacity to withstand the seismic load. Another point is the load distribution in the DIANA model which may be more accurate since FEM uses micro-modelling as modelling approach. In 3Muri the macro-modelling approach is used.
The displacement capacity of the DIANA model is highly underestimated due to limitations in the model as explained before. The displacement capacity can not be compared to the results obtained with SLaMA and 3Muri due to these limitations.

7 VARIATION STUDY

As introduced in Chapter 4 the building stock of Groningen is classified into different typologies. An overview of the classification process into the typology which is relevant for the case study Martini type K is visualized in Figure 7.1. Within the typology "block unit multiple" a further subdivision is made as regards the structural system, this part is not visualized in the figure.
In the classification process the geometrical aspects of the piers and spandrels are not taken into account, while these elements are essential for the seismic capacity of a structure. Moreover, the seismic behavior of the structure is characterized by the response of the individual elements. With a ductile response for example the structure is able to obtain larger displacements in contrast to a brittle response. Additionally, the concept of the capacity spectrum method is based upon the assumption that the lateral displacement capacity is definable for the seismic response of a structure.

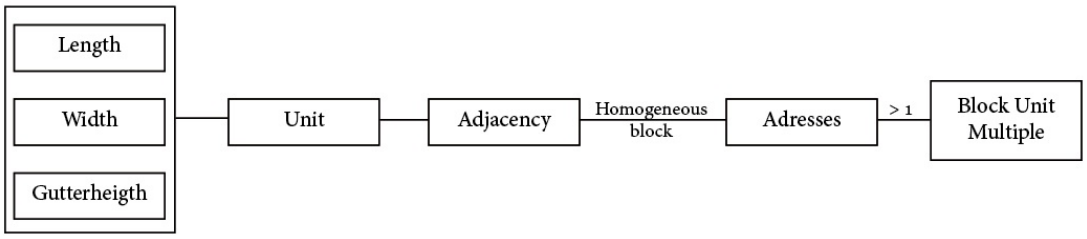

Figure 7.1: Classification process into the typology: "block unit multiple".

The focus of the variation study will be on the geometry of the piers within the facade. The geometry of the piers will be varied by changing the geometry of the openings of the facade. Firstly, the influence of the geometry of the piers on the seismic behavior will be analyzed. Secondly, a final improved proposal for the design of the Martini type K. structure will be made.

7.1 INFLUENCE OF THE GEOMETRY OF THE FACADE ON THE SEISMIC BEHAVIOR

For this part of the variation study only the top mechanism will be taken into account since this was the weakest mechanism of the structure. Additionally the structure will be loaded into the positive direction only since this was the weakest direction.
A reference model is first created which is visualized in Figure 7.2a. The dimensions of the piers visualized in the facade, pier 1 to 3, are equal in the variation study. The geometrical aspects of the fixed piers are presented in Table 7.1. The grey area in Figure 7.2a, is the area in which the geometrical aspects of the new "variable piers" will be varied. Three designs are made in

which the total area of openings is 30m^2 per model. Additionally, the party walls of 100 mm are not taken into account for this variation. This results in the variable piers which are modelled all don't have a flange, therewith a fair comparison can be made between the three models. In Figure 7.2 the facades are visualized for the three different models which are created. It is chosen to vary the size and the amount of the piers in order to verify what the influence of these geometrical aspects will be on the seismic capacity of the structure. In the following sections the affect of the parameters will be discussed based upon the results obtained with SLaMA and 3Muri. The NPR9998-2018 will be used as guideline for the SLaMA method and for part of the 3Muri models, hereafter referred to as 3Muri-NPR9998. Additionally the Eurocode 8 will be used as guideline for 3Muri, hereafter referred to as 3Muri-EC8. The geometrical aspects of the variable pier are summarized in Table 7.2.

(a) Reference model

(b) Facade 1

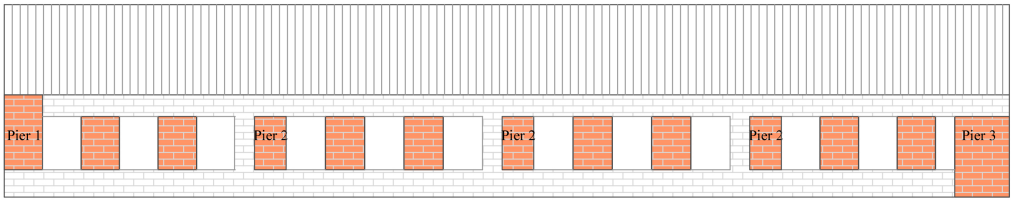

(c) Facade 2

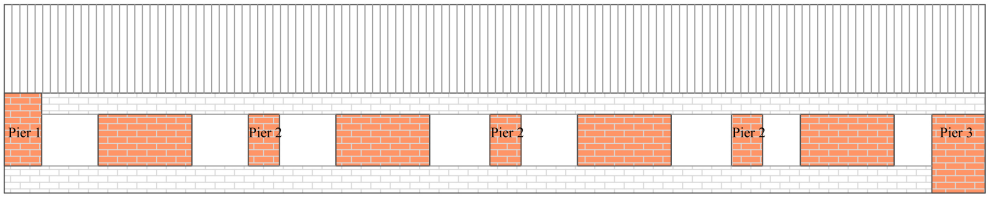

(d) Facade 3

Figure 7.2: Facades for the different models in which the amount of openings is varied.

Table 7.1: Geometrical aspects of the fixed piers.

	Width [mm]	Flange	Amount of piers
Pier 1	970	Yes	2
Pier 2	810	Yes	6
Pier 3	1390	No	2

Table 7.2: Geometrical aspects of the variable pier per facade.

	Width [mm]	Height [mm]	Amount of piers
Facade 1	499	1350	38
Facade 2	998	1350	16
Facade 3	2450	1350	8

7.1.1 The effect of the width of the pier on the displacement capacity of the structure

The geometry of the pier affects the displacement capacity of the structure, and thus the seismic behavior. It would be expected that with the increase of the width of the piers, the stiffness of the piers increase and consequently the displacement capacity decreases. In order to verify the influence of the width of the pier on the displacement capacity of the structure, the width of the piers is varied as visualized in Figure 7.2. In Figure 7.3 the pushover curves obtained with the different approaches of the different facades are visualized.

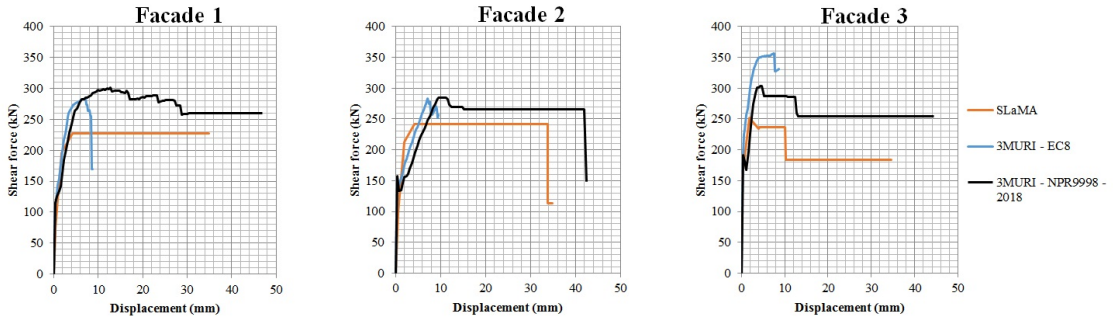

Figure 7.3: The pushover curve of the three facades with the original height of the piers of 1350 mm. Increasing the width of the variable pier doesn't result into an increase of the displacement capacity of the structure.

The effect of the changed width of the pier is not notable in the displacement capacity of the structure. The affect is only slightly visible in the capacity obtained with the 3Muri-NPR9998 model. For this model a higher displacement capacity can be observed of facade 1, still the displacement capacity is only 4 mm higher with respect to facade 2 and 3.

A point of interest is that the displacement capacity obtained with 3Muri-EC8 is highly underestimated with respect to the SLaMA method and 3Muri-NPR9998 model. The displacement capacity is approximately 9 mm for all the 3Muri -EC8 models which corresponds to the drift limit of 0.53% if shear failure is governing. In the 3Muri - EC8 models shear failure is indeed predominantly governing in all the models. In the Eurocode 8 no distinction is made between the shear sliding mechanism and the shear splitting mechanism, as is done in the NPR9998. Only the shear sliding failure mechanism is taken into account in the Eurocode 8. As explained before, in the piers in which splitting failure is governing relative high drift limits can be obtained which are comparable to the flexural failure mechanism. The splitting failure mechanism

is predominantly governing in facade 1 to 3 according to the SLaMA method and 3Muri-NPR9998 model. This explains the difference in the obtained displacement capacity between the NPR9998 and the EC8.

7.1.2 The effect of the width of the pier on the base shear capacity of the structure

The affect of the change of the width on the base shear capacity is investigated in this section. It would be expected that the base shear capacity of the structure increases with the increase of the width of the piers. The stiffness of the pier increases and consequently the shear capacity. The compression strut which develops in the pier is less steep and consequently the lateral resistance increases.

In Figure 7.4 the pushover curve of the facades are grouped per method in order to observe the differences in the obtained capacity more closely per approach.
The influence of the increased width of the piers on the base shear capacity obtained with the SLaMA method is mainly visible in the development of the base shear capacity of facade 3, as visualized in Figure 7.4a. In facade 1 and 2 splitting and flexural failure is predominantly governing, quite large drift limits can be obtained with these mechanisms. This in contrast to facade 3 in which a strength decrease is visible at a displacement of 10 mm which is caused by the failure of the variable pier due to shear sliding failure. The drift limits which can be obtained with this failure mechanism are relative low with respect to the splitting and flexural failure mechanism. The strength decrease of 50% is not reached here and additionally it is assumed that failure of these piers don't cause any dynamic instability. In other words, the NC limit state is not reached here.

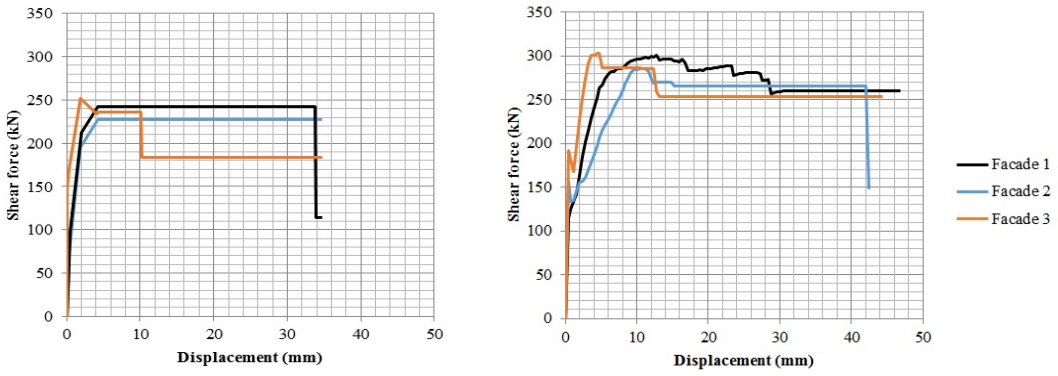

(a) SLaMA **(b)** 3Muri-NPR9998

Figure 7.4: The pushover curve of the three facades with the original height of the piers of 1350 mm. Increasing the width of the variable pier mainly affects the development of the base shear capacity of the structure.

The effect of the increased width of the piers is also for the 3Muri-NPR9998 mainly visible in how the base shear capacity develops over the displacement. In both the facades 2 and 3 a strength decrease can be observed which is due the shear sliding failure mechanism which is governing in part of the facade. The base shear capacity obtained after bilinearization of the 3Muri-NPR9998 models is given in Table 7.3 to give a more clear comparison. The table shows that increasing the width of the piers does not have a large affect on the base shear capacity.
In Figure 7.5 the pushover curve of the 3Muri-EC8 model per facade is visualized. The effect of the increased width of the pier is clearly visible in facade 3 in which the variable pier is the widest. The deviation of the base shear capacity of facade 3 with respect to facade 1 and 2 is

Table 7.3: Base shear capacity of the bilinearized pushover curve with the original height of the piers of 1350 mm obtained with 3Muri-NPR9998.

	Facade 1	**Facade 2**	**Facade 3**
Base shear capacity	277 kN	270 kN	259 kN

25%. The increase of base shear capacity is remarkable since the capacity of facade 1 and 2 is almost similar. This suggests that the geometrical properties have quite some influence on the base shear capacity of the models in 3Muri with the Eurocode 8 as guideline.

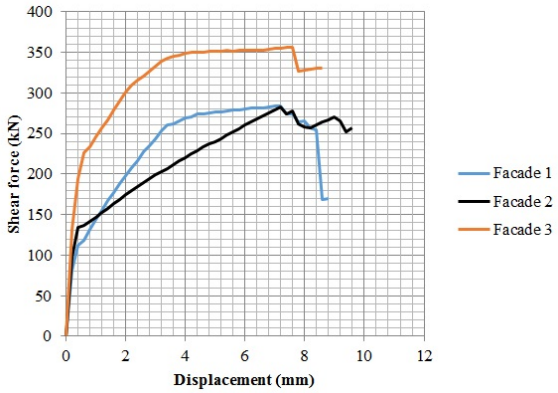

Figure 7.5: Pushover curve of the 3Muri-EC8 model for the different facades with the height of the piers of 1350 mm. Noteworthy is the increased base shear capacity of facade 3 with respect to facade 1 and 2.

7.1.3 The effect of the failure mechanism on the seismic capacity

Section 7.1.2 showed that the type of failure mechanism can be quite definable for the seismic capacity of the structure. The drift limit which can be obtained with the shear sliding mechanism is relative low with respect to the splitting and flexural failure mechanism. Failure of the piers due to shear sliding in an early stage of the earthquake can result into dynamic instability of the structure and consequently failure. Additionally, the seismic capacity is expressed in terms of displacement capacity. A higher displacement capacity results into more optimal behavior of a structure during an earthquake. In Figure 7.6 the relation between the height and the width of the piers is visualized and the corresponding failure mechanism. The relation is obtained by using the equations which are defined in the NPR9998 for the determination of the failure mechanism. In order to give a better understanding of the failure mechanism which is governing, the relation between the height and width is of the variable pier per facade is marked in the figure. The axial load is fixed at 5kN.

The focus of the variation study is mainly on the geometry of the piers. In this case the axial load on top of the variable piers is around the 5kN, but an interesting point would be what the increase of the axial load means for the governing failure mechanism. In Figure 7.7 the relation between the axial load and the height for the variable piers is given. From the figure it can be observed that the axial load is also of importance for the determination of the governing failure mechanism. However, from the figure it can be observed that if a flange would be present in the variable pier of facade 1 and 2, the governing failure mechanism would be similar if the height remains constant (1350 mm). If the height of the piers would be adjusted to 2000 mm for example, the flange effect would be of interest of the variable pier in facade 2. A decrease of the height of the piers will result into another failure mechanism to be governing. It must be noted

that the shear sliding mechanism is for 100% governing for the variable pier in facade 3 within a height range of 200-2000 mm and an axial load range of 0-150 kN.

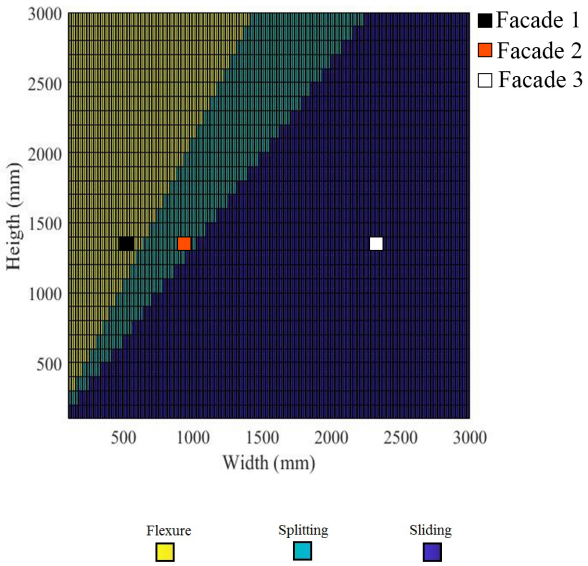

Figure 7.6: Relation between the height and width for an axial load of 5 kN for the variable pier per facade.

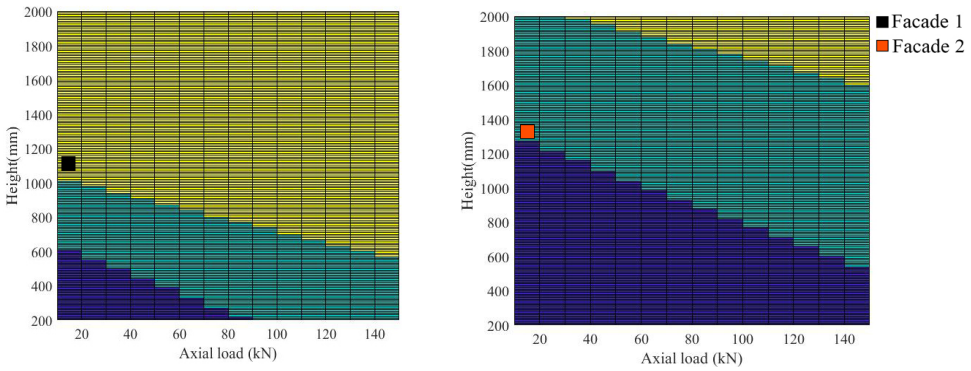

(a) Variable pier of facade 1, width = 499 mm and height = 1350 mm

(b) Variable pier of facade 2, width = 998 mm and height = 1350 mm

Figure 7.7: Relation between the axial load on top of the piers and height of the variable piers. Additional overburden due to the flange effect would not affect the governing failure mechanism of these piers.

7.1.4 The effect of the height of the piers on the displacement capacity of the structure

As explained in the previous sections, the geometry of the pier affects the displacement capacity of the structure. The height of the windows is varied in order to verify the influence of the height on the displacement capacity. The height of all the windows is first increased with 200 mm on both sides, thus 400 mm in total, to a height of 1750 mm. Secondly, the height of the windows is decreased with 200 mm on both sides, thus 400 mm in total, to a height of 950 mm.

In Figure 7.8 the pushover curve determined by the three approaches for the different height variances is visualized.

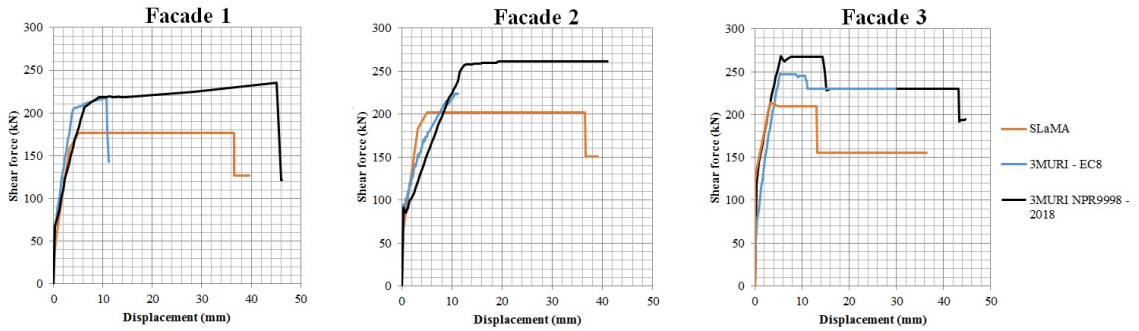

(a) Height of the piers = 1750mm

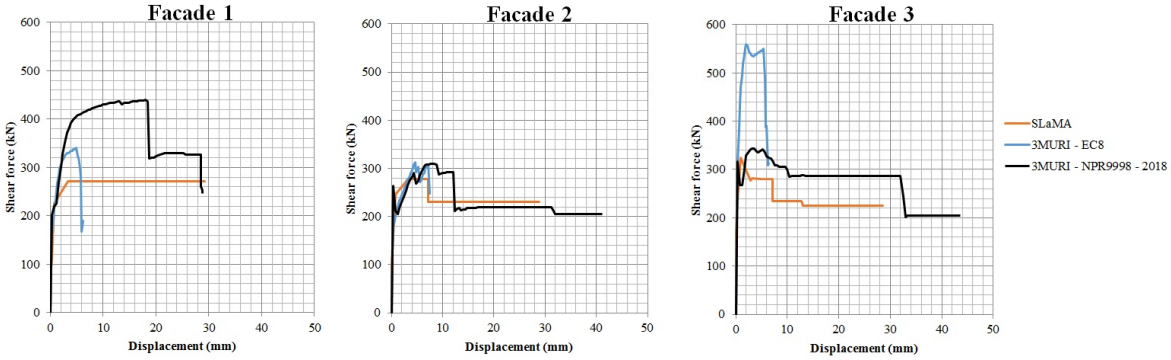

(b) Height of the piers = 950 mm

Figure 7.8: The pushover curve of the three facades with the increased and decreased height of the piers.

In Figure 7.9 the relation between the increased height of the piers and the displacement capacity is visualized per facade. Both SLaMA and 3Muri-NPR9998 show different results as regards the displacement capacity of the structure. The SLaMA method shows that with the increase of the height of the piers, the displacement capacity of the structure increases as well. This in contrast to the 3Muri-NPR9998 model in which the displacement capacity remains nearly similar if the height of the piers is changed. The most notable aspect here is the displacement capacity of facade 1 in which the height of the piers is 950 mm which is 38% lower with respect to facade 2 and 3 with a pier height of 950 mm. It must be noted that the results obtained for facade 1 with a pier height of 950 mm are questionable, the model had some difficulties in showing the results.
One would expect that the displacement capacity of the structure develops as the results show of the SLaMA method. With the increase of the height, the slenderness of the pier increases (H/L) and therewith the displacement capacity increases. This is in contrast to the results as obtained by the 3Muri-NPR9998 model. The fact that the displacement capacity doesn't change with the change of the height of all the piers suggest that the maximum drift limit is not correctly implemented in the software.

In order to verify this assumption, facade 3 with the height of the piers of 950 mm is analyzed more closely. In Figure 7.10 the pushover curve of the 3Muri-NPR9998 model is visualized. After a displacement of 32.4 mm a strength decrease can be observed. After this point only pier 1 and pier 2 have not failed. Both the piers fail at a displacement of 43.6 mm due to flexural and splitting failure. However, if the displacement capacity of these elements is determined accord-

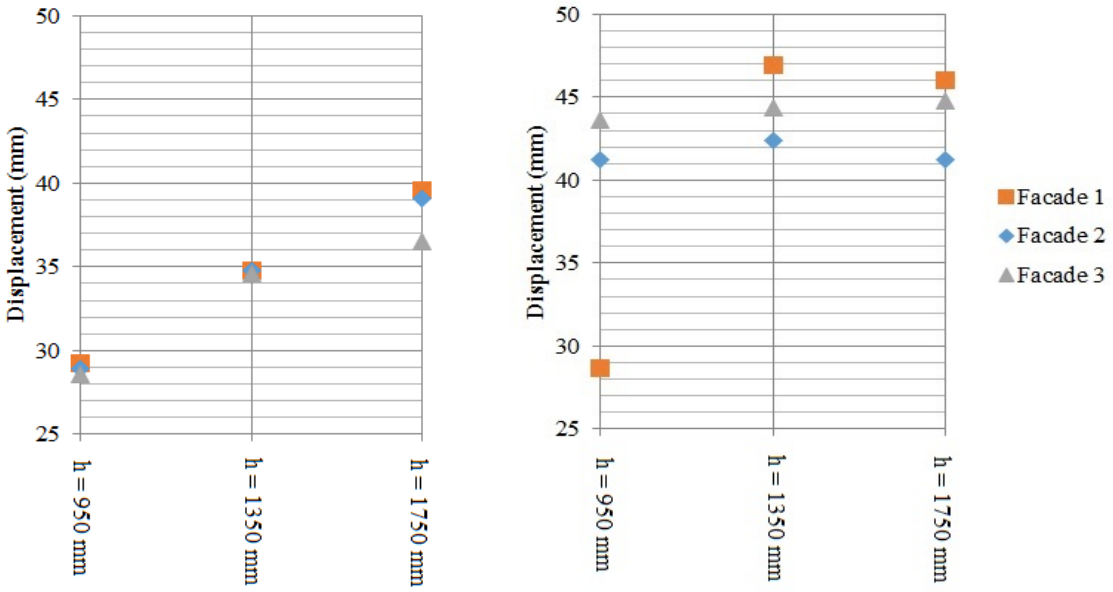

(a) SLaMA method **(b)** 3Muri-NPR9998 model

Figure 7.9: Relation between the increase of the height of the piers and the displacement capacity of the structure. Changing the height of the piers is clearly visible in the displacement capacity obtained with SLaMA. The changed height does not influence the displacement capacity in the 3Muri-NPR9998 model, this suggests that the drift limit is not implemented into the software of 3Muri-NPR9998.

ing to the equations as defined in the NPR9998 (based upon the load working on the element at a displacement of 32.4 mm), pier 2 has already exceeded its drift limit. The data from the 3Muri-NPR9998 model at that point is summarized in Table 7.4. The exceedance of the drift limit is also noticed in the other 3Muri-NPR9998 models, it is not clear from the software how this ultimate displacement is computed and why the piers are able to exceed the drift limits.

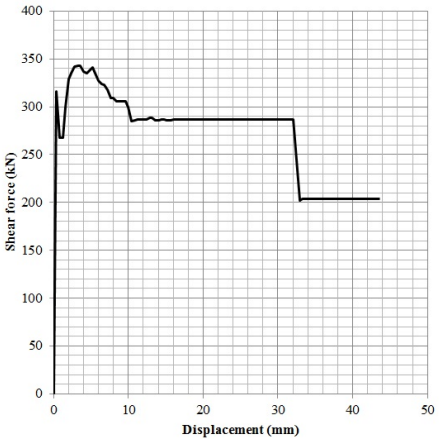

Figure 7.10: Pushover curve of the 3Muri-NPR9998 model for the pier height variance of 950 mm of facade 3. After a displacement of 32.4 mm only pier 1 and 2 didn't fail, however the drift limit of both the piers has already been exceeded.

A final interesting point is the development of the displacement capacity obtained with the 3Muri-EC8 models. In Figure 7.11a the relation between the displacement capacity for the dif-

Table 7.4: Data for the piers in the 3Muri-NPR9998 model facade 3, with a pier height of 950 mm to verify if the piers exceeds the drift limit.

	Width [mm]	Height [mm]	Axial load [kN]	Drift limit	Ultimate displacement [mm]
Pier 1	735	1775	59	1.99%	35.3
Pier 2	810	950	110	1.83%	17.4

ferent pier heights per facade are visualized. The figure shows that with the increase of the height of the piers, the displacement capacity increases as well. The increase of the displacement capacity is relative small with the increase of the height, but interesting is the high displacement capacity of facade 3 with a pier height of 1750 mm. This is related to the development of the base shear capacity of this variant. In Figure 7.11b the pushover curve of facade 3 with the different pier heights is visualized. Both the facades with a pier height of 950 mm and 1350 mm fail at a displacement around the 10 mm. In these height variances shear failure is governing in all the elements, consequently the drift limit is only 0.53%. In the height variance of 1750 mm the displacement capacity is 255% higher with respect to the height variance of 1350 mm. In the height variance of 1750 the variable pier fails at a displacement of 10.8 mm which is visible in the pushover curve by the strength decrease, however the strength decay is now only 12%. This is related to the governing failure mechanism in the other elements. In the height variances of 950 and 1350 mm, the shear failure mechanism was governing in all the elements. However in the height variance of 1750 mm the flexural failure mechanism is governing in 44% of the structure. After the failure of the piers due to shear, a residual global shear force capacity remains resulting in the strength decay of 50% which is not reached.

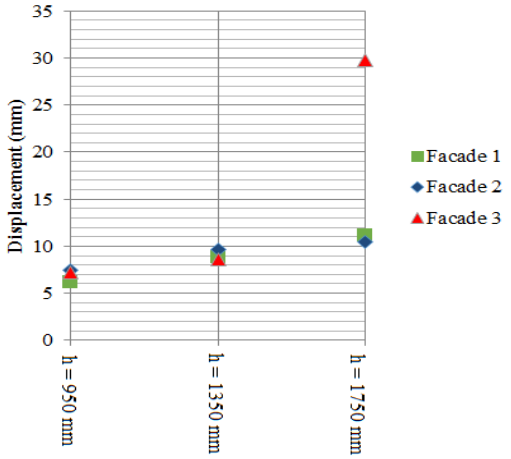

(a) Relation between the displacement capacity of the 3Muri-EC8 model and the height of the piers.

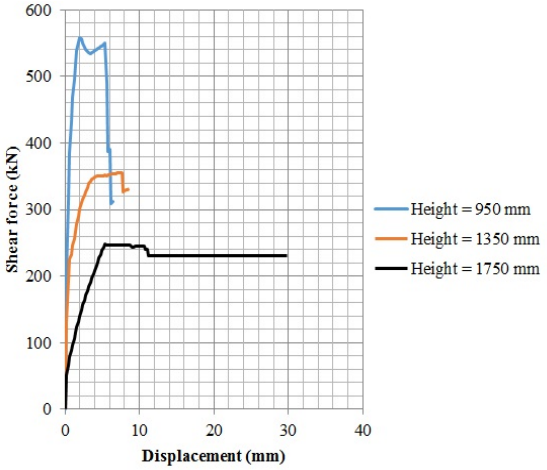

(b) Pushover curve for facade 3 with the different pier heights.

Figure 7.11: Results obtained for the 3Muri-EC8 model. The high displacement capacity of facade 3 with a pier height of 1750 mm is noteworthy, this is related to the development of the base shear capacity of the structure.

It it noteworthy that the displacement capacity only increases significantly of facade 3 and not of facade 1 and 2 of the pier height variance of 1750 mm. This is related to the axial load distribution in the piers. In facade 3 the variable pier fails at an early stage of the analysis due to shear failure, resulting in a redistribution of the axial load. The axial load increases in pier 2 which results into flexural damage and as explained before, with flexural damage/failure high

drift limits can be obtained. However, at a displacement of 30 mm shear failure prevails over flexural damage in pier 2 and subsequently the structure fails.
In facade 1 and 2 the axial load in pier 2 is only 1 kN lower, which results into pier 2 to fail due to shear failure in a relative early stage of the earthquake. Therewith the 50% strength decay is already reached and lower displacements can be obtained in facade 1 and 2. The differences in the displacement capacity are however significant.

7.1.5 The effect of the pier height on the base shear capacity on the structure

It is expected that the height of the piers influence the base shear capacity of a structure. With the increase of the height the compression strut through the pier is steeper and consequently the lateral resistance is expected to be lower. With the decrease of the height of the pier on the other hand, the lateral resistance is expected to increase. The relation between the height of the piers and the base shear capacity is visualized in Figure 7.12.

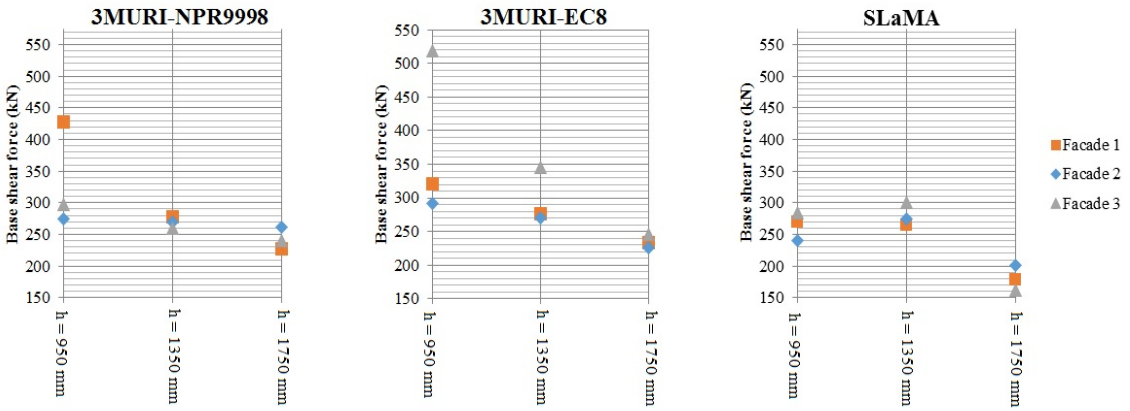

Figure 7.12: Relation between the base shear capacity and the pier height grouped per model for the different facades. Variation of the height is clearly visible in the obtained base shear capacity.

For the SLaMA approach the influence of the increased pier height is clearly visible. An interesting point is that for the piers with a height of 950 mm, the base shear capacity of the structure has slightly decreased with respect to the height variance of 1350 mm. One would expect that with the decrease of the height the lateral resistance increases. This can be explained by the development of the failure mechanisms. As mentioned before the base shear capacity as visualized in Figure 7.12 shows the base shear capacity of the bilinearized curve. In facades 2 and 3 with the height variance of 950 mm, the shear sliding mechanism is governing in a part of the structure. This results into a strength decrease after the drift limit of 0.75% is exceeded. The strength decrease is taken into account for the bilinearization of the pushover curve, consequently the base shear capacity is lower after the bilinearization. This explains the decreased base shear capacity. The peak base shear capacity of both facade 2 and facade 3 for the height variance of 950 mm are higher with respect to the height variances of 1350 and 1750 mm, see Figure 7.8.

A similar development of the base shear capacity with the variation of the pier height can be observed for the 3Muri-NPR9998 model. The increased base shear capacity of facade 1 with a height of 950 mm is noteworthy. However as explained in Section 7.1.4 the results of this model are questionable.

A final interesting point is the increase of the base shear capacity of the 3Muri-EC8 model of facade 3 with the decrease of the pier height. This is probably related to the influence of the ge-

ometry of the piers in facade 3 which are quite squat, the slenderness of the piers is presented in Table 7.5. In Figure 7.13 the shear capacity of the variable pier in facade 3 is visualized obtained with 3Muri-EC8. The shear force capacity increases significantly with the decrease of the height of the piers. The shear force capacity of the adjacent piers is almost similar for the different height variances.

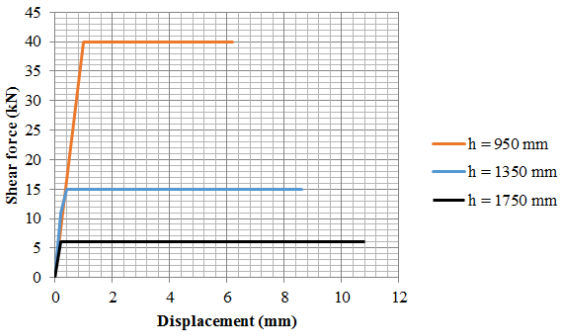

Figure 7.13: Shear capacity of the variable pier in facade 3 per height variance obtained with 3Muri-EC8. Decreasing the height has significant affect on the shear capacity of the pier.

Table 7.5: Slenderness of the variable piers in facade 3.

	h = 950 mm	**h = 1350 mm**	**h = 1750 mm**
Slenderness [H/L]	0.38	0.55	0.71

7.1.6 Seismic capacity per method

The results which are obtained with the three modelling approaches: SLaMA, 3Muri-EC8 and 3Muri-NPR9998 differ in some models significantly from each other. The capacity obtained with 3Muri-NPR9998 and SLaMA are quite comparable to each other, probably due to the fact the NPR9998 is used as leading guideline for both the approaches. In Figure 7.14 the base shear capacity of the different modelling approaches are compared to each other.

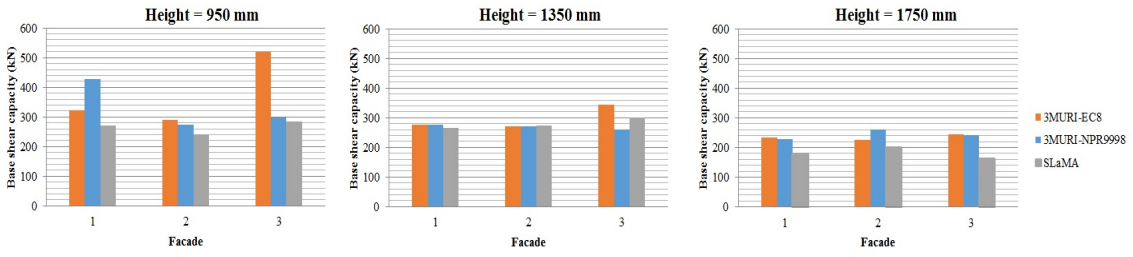

Figure 7.14: Comparison of the obtained base shear capacity with the different modelling approaches.

From the figure it can be observed that the base shear capacity obtained with the three different modelling approaches are quite similar for the pier height variance of 1350 mm and 1750 mm. For the pier height variance of 950 mm more outliers can be observed. For example the base shear capacity obtained with the 3Muri-EC8 model with the height variance of 950 mm for facade 3 is 78% higher with respect to the SLaMA model.
The base shear capacity obtained with SLaMA is generally lower than the base shear capacity obtained with the 3Muri software. It is expected that this is related with the redistribution of

loads which takes place in the 3Muri software in contrast to the SLaMA approach. In the SLaMA approach the load on top of the pier is determined at the start of the analysis and not updated during the analysis if an adjacent element fails. Additionally, the governing failure mechanism in the facade can differ with respect to the 3Muri software due to the redistribution. A change in the load distribution in the 3Muri software can result in another failure mechanism of the 3Muri model with respect to the SLaMA approach.

In Figure 7.15 the displacement capacity obtained with the different approaches for the facades with different pier heights is visualized. The figure shows that the difference in the ultimate displacement capacity determined per method is quite large. Firstly, the displacement obtained with 3Muri-EC8 is significantly lower than the 3Muri-NPR9998 and SLaMA model. As explained in Section 7.1.1 this is due to the fact that in the Eurocode 8 no distinction is made within the shear failure mechanism between splitting and shear sliding as is done in the NPR9998.

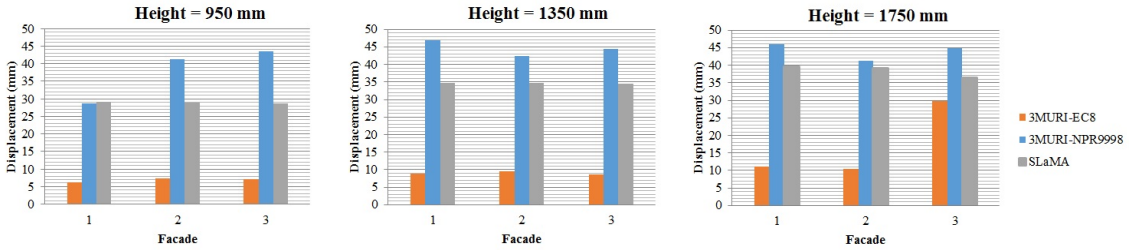

Figure 7.15: Comparison of the obtained displacement capacity with the different modelling approaches.

The obtained displacement capacity of the 3Muri-NPR9998 model is higher for all the facade types with respect to the SLaMA method. However, as explained in Section 7.1.4 it is questionable if the 3Muri-NPR9998 model has defined the drift limits properly. The elements in the 3Muri-NPR9998 model are able to exceed the drift limits.

7.1.7 Spectral displacement method

The seismic capacity of the different structures is now compared to the seismic demand. Only the top mechanism it thus taken into account and converted to its equivalent SDoF system. The focus will be on the results obtained with the SLaMA method since the results are governing over the results of the 3Muri-NPR9998 model. The results obtained with the 3Muri-EC8 model are not taken into account since the displacement capacity is very low and not relevant to analyze further.

In Figure 7.16 the spectral displacement method is visualized for the different facades with different heights. It is marked in the graphs with a red dot if the splitting failure mechanism is predominantly governing in the structure. According to the NPR9998 a maximum drift of 0.6% is governing at global level for this mechanism if splitting is predominant. Secondly, the point where a critical strength decrease occurs in a structure is marked with an orange cross in the graphs. For the SLaMA method it is not as straight forward to conclude that a structure is dynamic unstable after failure of part of the elements without the 50% strength decay being reached. However, in this case the main function of the facade is to carry its own weight. The floor spans into the opposite direction of the facade, between the transverse walls, with as main goal during a seismic event to redistribute the lateral load. From an engineering point of view it is concluded that the NC limit state is probably not reached at this point since the floor is still able to fulfill its function.

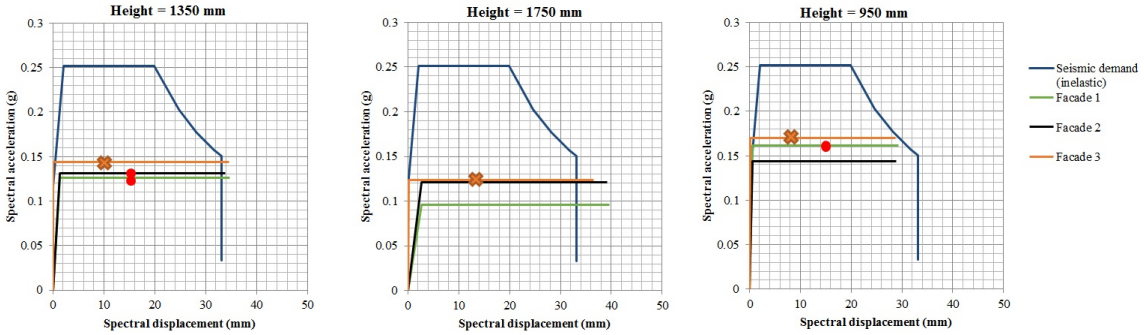

Figure 7.16: Spectral displacement method for the SLaMA approach.

7.2 PROPOSED IMPROVED DESIGN OF THE MARTINI TYPE K. STRUCTURE

Section 7.1 showed that the influence of the geometry and the corresponding failure mechanisms is of high importance for the seismic behavior of a structure. In this section a final proposal for an improved design of the Martini type K. structure is made. A proposal for an improved geometry of the facade is made. It must be noted that the proposed improvement is based upon the in-plane capacity of the individual elements and it that this is not the common way to design a structure. However, the geometrical properties of the individual elements could be taken into account for the design of the facade in the future if a structure is subjected to seismic loading.
The new calculations are only made for the structure loaded into the positive direction since this was the weakest direction.

From the previous section it became clear that the failure mechanism is of high importance for the seismic behavior of a structure. In Section 7.1 it was shown that the shear sliding mechanism is not in favor for the seismic behavior of a structure. The drift limits are very low with respect to the other mechanisms and can result in a strength decrease at an early stage of the earthquake. Additionally the behavior of the shear splitting failure mechanism is inconsistently defined in the NPR9998. The response of the mechanism is locally determined as a ductile mechanism, but on global level the mechanism is determined as a brittle mechanism. The maximum inter-storey drift is only 0.6%.

The improved design is focused on the changed width of the piers in such a way that the flexural failure mechanism is governing. The flexural failure mechanism is a stable failure mode which can obtain relative high displacements without a significant decrease of the strength (Priestley et al., 2007). Small changes in the width of the pier are made so that flexural failure is the governing failure mechanism.
In Figure 7.17 the relation between the axial loading and the width of the element is visualized. The relation is obtained with the equations as prescribed in the NPR9998. Per figure the changes which are made per pier are visualized. The height is varied in the graphs in order to map all the piers from the case study.
The percentage of openings is for the top mechanism 35% and the bottom mechanism of 46.1%. In Figure 7.18 the geometry of the renewed facade is shown.

7.2.1 Comparison of the results

The results obtained with the SLaMA, 3Muri-EC8 and 3Muri-NPR9998 approaches are bilinearized and visualized in Figure 7.19. The base shear capacity obtained with the SLaMA approach represents both the top and bottom mechanism in order to make a fair comparison with the 3Muri models. It must be noted that the limitations defined by the NPR9998 about the NC limit state are taken into account. Since the splitting failure was predominantly governing in the original case study for the outcomes obtained with SLaMA and 3Muri-NPR9998, the structure is determined as a structure with brittle response. For the 3Muri-EC8 model only the 50% strength decay is used as limitation. The improvements of the new design are discussed per approach.

SLaMA

The changed geometry has a positive influence on the seismic behavior from the results obtained with the SLaMA approach. The flexural failure mechanism is governing which response is ductile which results into an increase of the global displacement capacity. The base shear capacity decreases, however as mentioned before the base shear capacity is less relevant for the seismic design of a structure.

3Muri-EC8

The results of the changed geometry obtained with the 3Muri-EC8 model are not as expected. The displacement capacity of the changed geometry is lower than the displacement capacity of the original case study. Shear failure was still governing in a large part of the structure. As explained in Section 7.1.1 the Eurocode only makes a distinction between shear sliding and flexural failure. The drift limits which can be obtained with shear sliding are relative low (0.53%) which results in failure of the structure at an early stage of the analysis.

3Muri-NPR9998

The results of 3Muri-NPR9998 for the changed geometry are mainly visible in the base shear capacity which decreases. The displacement capacity is almost similar, however since diagonal tension failure is still predominantly governing, the response is determined as brittle at global level according to the NPR9998. Without the limitations the displacement of the original model is 80.3 mm and for the improved design 80.5 mm.
However the reliability of the model is questionable as explained in Section 6.4.3.

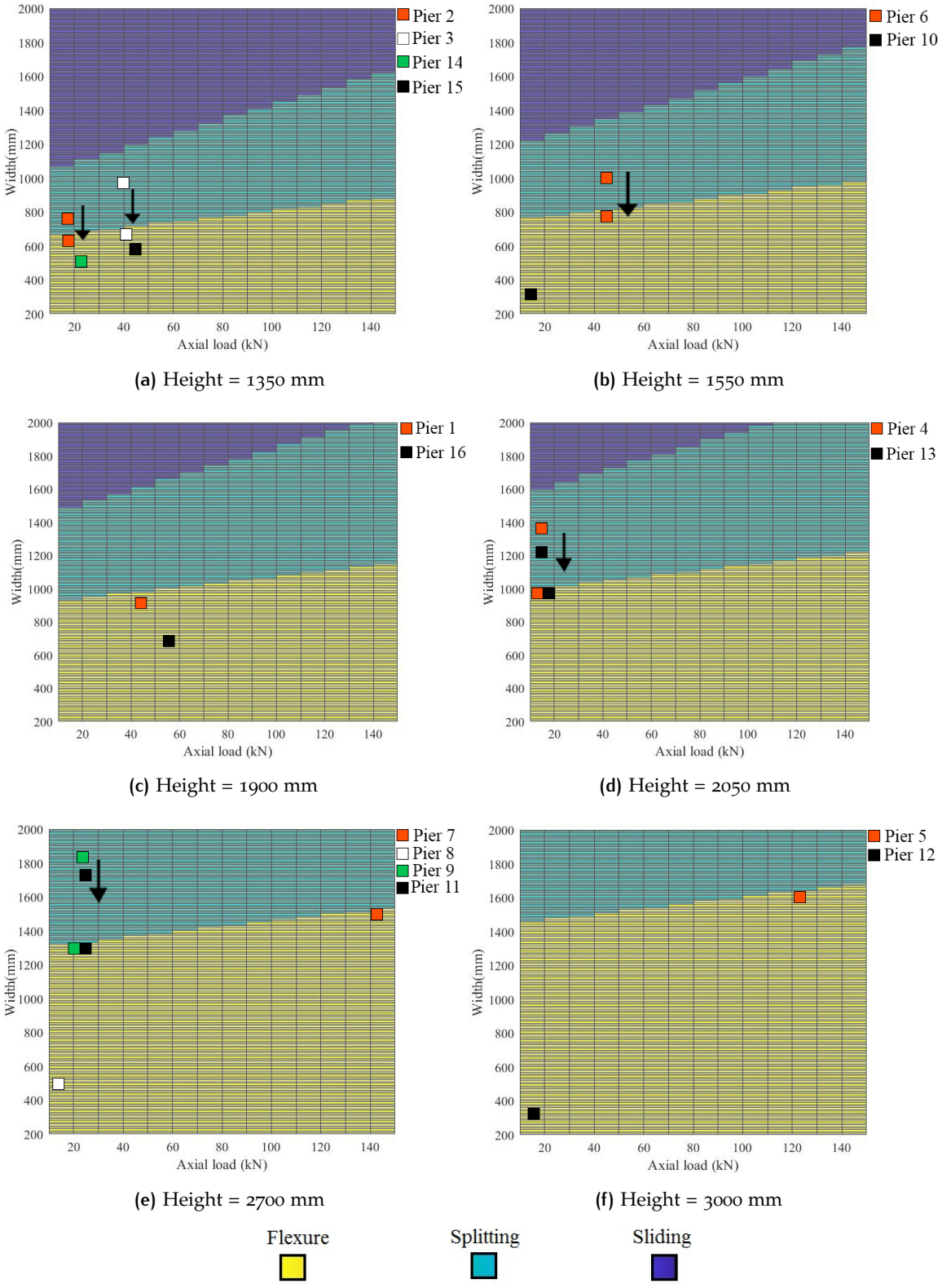

(a) Height = 1350 mm

(b) Height = 1550 mm

(c) Height = 1900 mm

(d) Height = 2050 mm

(e) Height = 2700 mm

(f) Height = 3000 mm

Figure 7.17: Relation between the axial loading and width of the piers and its governing failure mechanism into the positive direction. The transformation is visualized for the piers which geometry is changed.

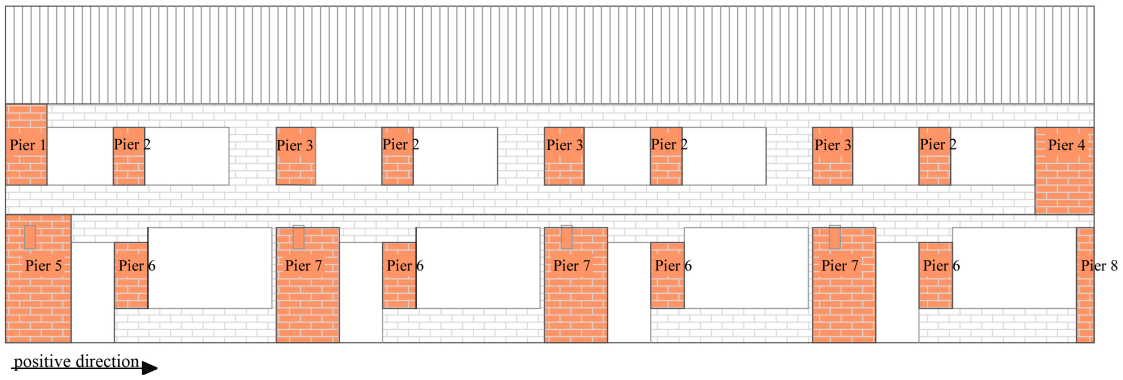

(a) Front facade

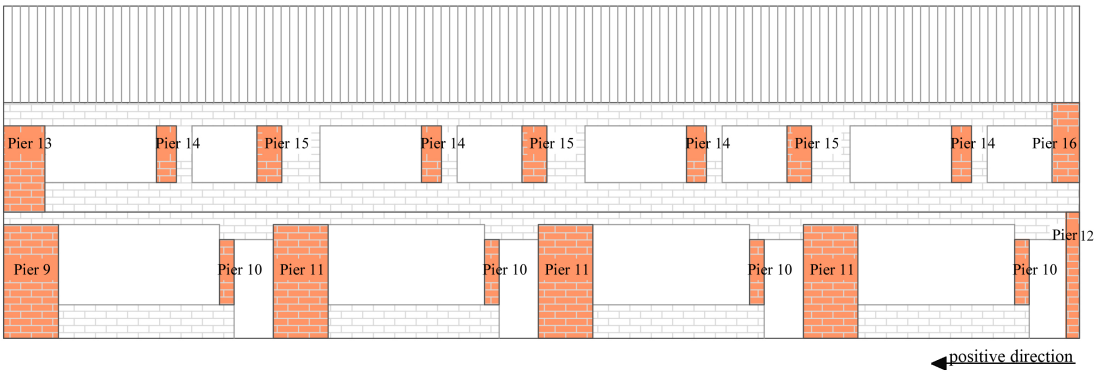

(b) Back facade

Figure 7.18: Geometry of the facade for the improved design of the Martini type K house.

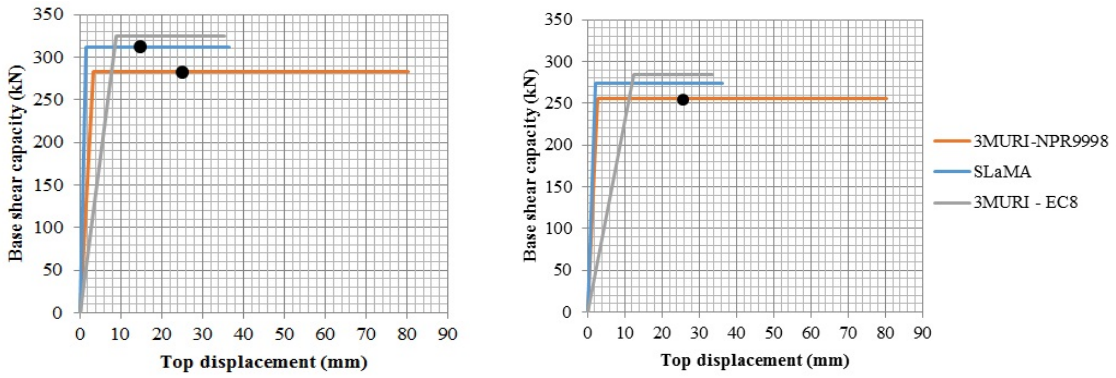

(a) Original case study **(b)** Proposed improvement

Figure 7.19: Bilinearized curves of the Martini type K. Structure obtained with the different modelling approaches. The black dot represents the global drift limit according to the NPR9998.

8 CONCLUSION AND RECOMMENDATIONS

8.1 CONCLUSION

In this section an answer will be given to the two main research questions:

1. To what extent are the SLaMA method and the equivalent frame approach as implemented in the software package 3Muri able to describe the seismic behavior of an URM terraced house in Groningen?
2. To what extent is the seismic behavior of an URM terraced house case study in Groningen influenced by the variation of the geometry of the facades?

An answer is given to these research questions by analyzing two case studies. The first case study represents a typical but idealized URM structure of a terraced house from which the seismic capacity was determined in the TU Delft lab by cyclic pushover tests. The second case study concerns a specific two-storey URM terraced house located in Groningen. The case studies are characterized by large daylight openings, slender piers and a low lateral capacity into the x-direction. Both the case studies were analyzed with the SLaMA method and the equivalent frame approach as implemented in the 3Muri software. It must be noted that 3Muri version 12.2.1.4 is used here and that the following conclusions as regards 3Muri are related to the used software.

8.1.1 Definition of the seismic capacity of the two case studies by applying the SLaMA method and 3Muri

Based upon the case studies the following conclusions can be made about the application of the SLaMA method and 3Muri to an URM terraced house:

- Based on the results obtained for the first case study, the SLaMA method according to the NPR9998-2018 gives a valid indication about the seismic behavior of an URM terraced house structure. The SLaMA method underestimates both the base shear and the displacement capacity with respect to the experimental results. The base shear capacity is underestimated with 22.5% into the positive direction and 24.4% in the negative direction. The displacement capacity is underestimated with 33.6% into the positive direction and 23.8% into the negative direction. Besides a proper indication about the seismic capacity, the user is able to determine the governing failure mechanism with the method. To conclude, the SLaMA method is suitable to determine the seismic behavior of the terraced house structure, however it must be noted that the outcome is conservative. The conservative results are as expected since SLaMA is a simplified method.
- The equivalent 3Muri model has some notable modeling limitations related with the large openings and the lack of spandrels in the first case study. An element which connects the piers was required since the software does not include the floor in the mesh. A sensitivity study has been performed and it was concluded that the reinforced concrete beam as connecting element was the most suitable representation of the physical model. However, the results obtained with this model still highly underestimate the seismic capacity of the structure. Additionally it must be noted that the Eurocode 8 was used as guideline since

the results obtained with the NPR9998-2018 as guideline were limited. It can be concluded that due to the limitations in the software, the current employed version of 3Muri is not suitable to determine the seismic behavior of the typical structure of the terraced house without spandrels properly.

- The outcome of the seismic behavior of the second case study, the Martini type K house, is similar according to the SLaMA method and the software 3Muri. The NPR9998-2018 was used as guideline for the SLaMA method and the Eurocode 8 as guideline for the 3Muri model. Both the approaches used in this case study show similar results for the expected seismic behavior at global level into the positive direction. In the negative direction the base shear capacity of the 3Muri-EC8 model deviates 8% and the displacement capacity deviates 28% with respect to SLaMA. The large deviation as regards the displacement capacity is related to the used guideline. The drift limits which can be obtained with the shear failure mechanism as defined in the Eurocode 8 are significantly lower than the shear failure mechanism as defined in the NPR9998. However, this is related to the used guideline and not the 3Muri software.
- The reliability of the NPR9998-2018 as guideline in the software 3Muri remains questionable for complex structures. The diagonal tensile failure mechanism is not correctly implemented into the software. In the second case study no strength decay was observed even though a significant percentage of the elements has failed due to diagonal tensile failure. After failure of an element due to diagonal tension, the strength and stiffness of the elements remain constant and don't affect the global behavior.
- The drift limit as implemented into the software 3Muri is not accurate at local level. The drift limit of several elements exceeded the limit that should be implemented by the software for the corresponding failure modes, resulting into elements which are able to exceed its drift limits.
- It is important that the user of 3Muri pays attention to the automatic mesh which is created by the software. The modelling choices are visible in the mesh and influence the outcomes. The loads act upon the nodes and by changing the mesh the internal load distribution changes significantly. Additionally, the seismic capacity of the structure is very sensitive for small changes in the mesh.

To conclude, the seismic capacity determined with both the approaches is conservative but gives a valid indication about the seismic capacity of the URM terraced house in Groningen. This does not apply to the EFM as implemented into the software 3Muri if there are no spandrels present in the structure. Additionally it must be noted that the assumptions which were made in both the SLaMA method and 3Muri as regards the Martini type K house are similar, however it is possible that these assumptions influenced the outcome of the seismic behavior and are not an accurate representation of the seismic behavior. It is difficult to assess the outcome since there are no results for a benchmark. More research is required so that the outcome of the SLaMA method and the EFM as implemented into the software 3Muri can be verified. This could be realized by experimental or numerical research with more advanced modelling strategies.

8.1.2 Influence of the geometry of the facade

The variation study of the facade was focused on the influence of the geometry of the piers on the seismic behavior. The following conclusions can be made as regards the influence of the geometry on the seismic behavior:

- The increased width of the pier affects the the governing failure mechanism and consequently the displacement capacity of the pier. If the shear sliding mechanism is governing,

relative low drifts can be obtained, resulting in a strength decrease in a relative early stage of an earthquake. This can result into a structure reaching the NC limit state with a relative low global displacement capacity. Additionally the splitting failure mechanism is determined by the NPR9998 as brittle at global level, resulting in a low global displacement capacity.

- By increasing the height of the pier the displacement capacity of the piers increases as well. Higher drifts can be obtained which is in favor of the seismic capacity.
- The geometry of the pier affects the base shear capacity of the structure. With the decrease of the height, the base shear capacity increases. The influence of the width of the pier is not clearly notable in this study. However, the base shear capacity does not have a high influence on the seismic behavior of the structure.

In conclusion, the seismic behavior of an URM terraced house is mainly affected by the governing failure mechanisms of the individual elements and thus by the geometry of the facade. A variation in the geometry of the individual elements can result into differences in the seismic behavior of an URM terraced house at global level. It is therefore important to verify the capacity of the individual elements.

8.2 RECOMMENDATIONS

In this section the recommendations will be summed for further research.

- The seismic behavior of an URM structure is analyzed in this thesis by two case studies, however more research is required in order to verify whether the results obtained with SLaMA and 3Muri are a correct indication. Results obtained by either numerical or experimental research is required in order to have a valid benchmark. For the numerical research the focus should lie on validated FEM software packages.
- From the research it became clear that the reliability of the EFM as implemented into the software 3Muri is questionable with the use of the NPR9998-2018 as guideline, especially for more complex structures. More research into the use of this guideline with the software 3Muri is required.
- The drift limits are exceeded at local level with both the NPR9998-2018 and the Eurocode 8 as guideline. Further research into the drift limits and why these can be exceeded in 3Muri would be interesting.
- This study was focused on the in-plane behavior of an URM terraced house. More research into the out-of-plane behavior of both the case studies is deemed to be interesting. Additionally, more research is required in order to verify whether the determined out-of-plane capacity is correct according to annex H of the NPR9998.
- Experimental research into the failure mechanism splitting failure would be interesting. It is now inconsistently defined in the NPR9998 and the differences in the displacement capacity for the mechanism determined as either brittle or ductile at global level are significant.
- The variation study was mainly focused on the influence of the geometric variations of the pier on the seismic behavior. A variation study focused on the influence of the spandrels on the seismic behavior is deemed to be interesting. Additionally a variation study in which the windows are irregular placed at the facade (different heights per window on the same level) would be interesting.

- An analysis into the imposition of the floor. If the floor spans between the in-plane loaded walls, is the 50% strength decay still relevant. Or should this decay be lower since it is more likely that dynamic instability is reached before the 50% strength decay. Additionally, a study into the connection between the floor and the load bearing elements would be usefull. How does the connection affect the seismic behavior.
- More sensitivity analysis which are focused on the material properties of the structure would be interesting.

BIBLIOGRAPHY

Angelillo, M. (2014). *Mechanics of Masonry Structures*, volume 551.

ARUP & NAM (2018). Groningen Earthquakes Structural Upgrading Data Documentation Exposure Database. Technical Report Version 5.

ATC (1996). Seismic Evaluation and Retrofit of Concrete Buildings. Technical report, Applied Technology Council, Redwood City.

Backes, H. (1985). *On the Behaviour of Masonry Under Tension in the Direction of the Bed Joints*. Phd thesis, Aachen University of Technology.

Calderini, C., Cattari, S., and Lagomarsino, S. (2009). In-plane strength of unreinforced masonry piers. (November 2008):243–267.

Ćosić, M. (2009). About the Required Capacity of Nonlinear Deformations of the SDOF System with the Pushover Analysis. In *2nd International Congress of Serbian Society of Mechanics*.

D'Ayala, D. and Speranza, E. (2003). Definition of Collapse Mechanisms and Seismic Vulnerability of Historic Masonry Buildings. *Earthquake Spectra*, 19(3):479–509.

de Groot, A. (2019). *Structural window design for in-plane seismic strengthening*. Master of science, Delft University of Technology.

Deniz Dalgic, K., Mariani, V., Hendriks, M., and Rots, J. (2017). NONLINEAR PUSHOVER ANALYSIS OF TYPE K-TERRACED HOUSES.

Esposito, R., Jafari, S., Schipper, H. R., and Rots, J. G. (2018). Influence of the behaviour of calcium silicate brick and element masonry on the lateral capacity of structures. In *The 10th Australasian Masonry Conference*, pages 11–14, Sydney, Australia.

Esposito, R., Terwel, K., Ravenshorst, G., Schipper, H., Messali, F., and Rots, J. (2017). Cyclic pushover test on an unreinforced masonry structure reseambling a typical Dutch terraced house. In *Proceedings of the 16th World Conference on Earthquake Engineering 2017*, pages 1–12, Santiago, Chile.

Fajfar, P. (1999). Capacity spectrum method based on inelastic demand spectra. *Earthquake Engineering and Structural Dynamics*, 28(November 1998):979–993.

Fantastic Handyman Team (2018). Cracks in Bricks Walls: Why Brick Walls Crack and How to Repair Cracked Bricks.

Hayen, R., Balen, K. V., and Gemert, D. V. (2004). The mechanical behaviour of historic masonry structures. pages 1–10.

Kilar, V. and Petrovc, S. (2013). Seismic failure mode interaction for the equivalent frame modeling of unreinforced masonry structures. 54:9–22.

Krawinkler, H. and Seneviratna, G. (1998). Pros and cons of a pushover analysis of seismic performance evaluation. *Engineering structures*, 20(4-6):452–464.

Lagomarsino, S., Penna, A., Galasco, A., and Cattari, S. (2013). TREMURI program : An equivalent frame model for the nonlinear seismic analysis of masonry buildings. *ENGINEERING STRUCTURES*, 56:1787–1799.

Laurenço, P. (1996). *Computational Strategies for Masonry Structures*. Phd thesis, Technical University of Delft.

Laurenço, P., Rots, J., and Blaauwendraad, J. (1995). Two approaches for the analysis of masonry structures : micro and macro-modeling. *HERON*, 40(4):313–340.

Magenes, G. and Calvi, G. M. (1997). IN-PLANE SEISMIC RESPONSE OF BRICK MASONRY WALLS. *Earthquake Engineering and Structural Dynamics*, 26(July 1996):1091–1112.

Mosalam, K., Glascoe, L., and Bernier, J. (2009). Mechanical Properties of Unreinforced Brick Masonry, Section1. pages 1–26.

NZSEE (2017). C8 -Unreinforced Masonry Buildings.

Page, A. W. (1982). An Experimental Investigation of the Biaxial Strength of Brick Masonry. In *Proceedings of the Sixth International Brick Masonry Conference (Rome)*, pages 3–15.

Petry, S. and Beyer, K. (2014). Flexural deformations of URM piers : Comparison of analytical models with experiments. In *9th International Masonry Conference*, pages 1–12.

Pfeifer, G., Ramcke, R., Achtzicker, J., and Zilch, K. (2001). *Masonry construction manual*.

Priestley, M., Calvi, G., and Kowalsky, M. (2007). *Displacement-Based Seismic Design of Structures*. IUSS PRESS, Pavia, Italy.

Russell, A. P. and Ingham, J. M. (2010). The influence of flanges on the in-plane seismic performance of URM walls in New Zealand buildings. In *Proceedings of 2010 NZSEE Conference*, New Zealand.

S.T.A. DATA srl (2019). 3muri User Manual release:10.9.0.

Themelis, S. (2008). *Pushover analysis for seismic assessment and design of structures*. Docter of philosophy, Heriot-Watt University.

Vaculik, J. (2012). *Unreinforced masonry walls subjected to out-of-plane seismic actions*. Phd thesis, The University of Adelaide.

van der Pluijm, R. (1992). Material properties of masonry and its components under tension and shear. In *Proceedings of the 6th Canadian Masonry Symposium*, pages 675–686, Saskatoon, Canada. University of Saskatchewan.

van der Pluijm, R. (1999). *Out-of-plane bending of masonry : behaviour and strength Out-of-Plane Bending of Masonry Behaviour and Strength*. Phd thesis, Technical University of Eindhoven.

Yi, T., Moon, F., Leon, R., and Kahn, L. (2008). Flange effects on the nonlinear behavior of URM piers. *TMS Journal*.

A RESULTS CASE STUDY 1

In this chapter additional results related to the first case study as elaborated in Chapter 5 are presented.

Reinforced concrete beams

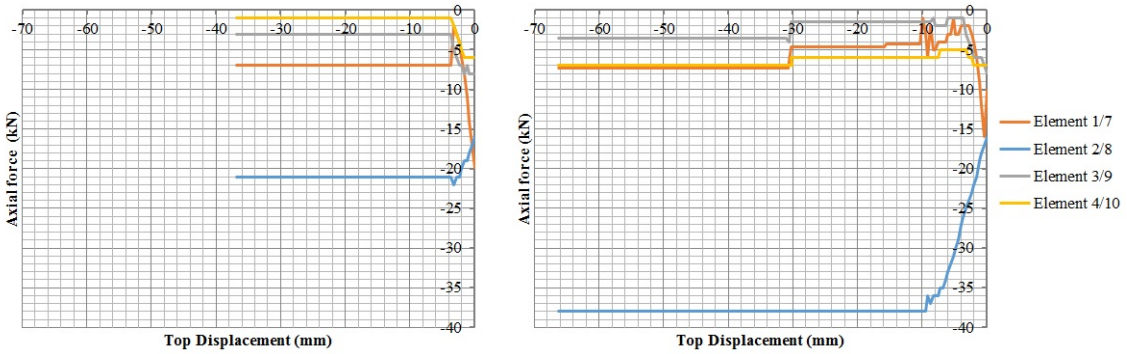

Figure A.1: Axial load distribution in the piers loaded into the negative direction, left: RC beam size; h=165 mm, w=100 mm and on the right: RC beam size; h=100 mm, w=100 mm. The concrete class of the beams is C55/67

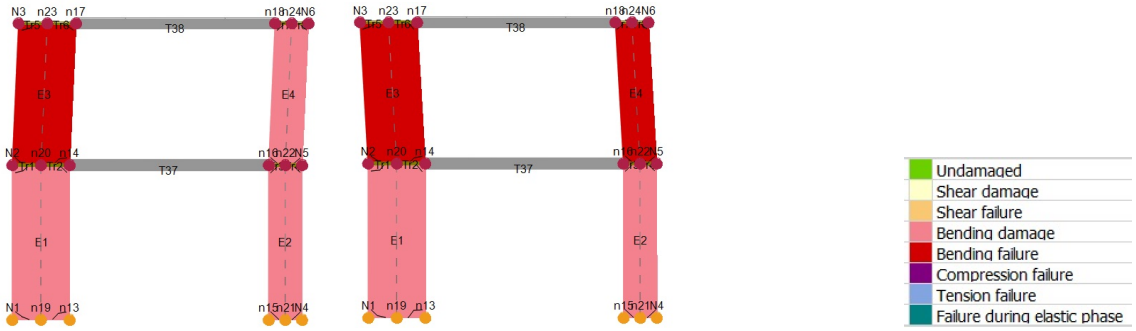

(a) Positive direction **(b)** Negative direction **(c)** Failure legend

Figure A.2: Failure mechanism of the reinforced concrete beam with dimensions h=100 mm, w=100mm and concrete class C55/67.

Encirclement

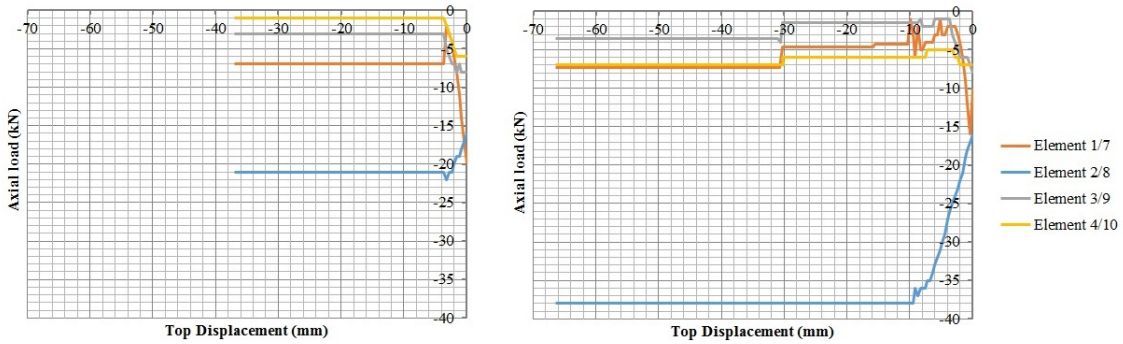

Figure A.3: Axial load distribution in the piers loaded into the negative direction, left: encirclement size; h=165 mm, w=100 mm and on the right: encirclement size; h=100 mm, w=100 mm. The concrete class of the encirclements is C55/67.

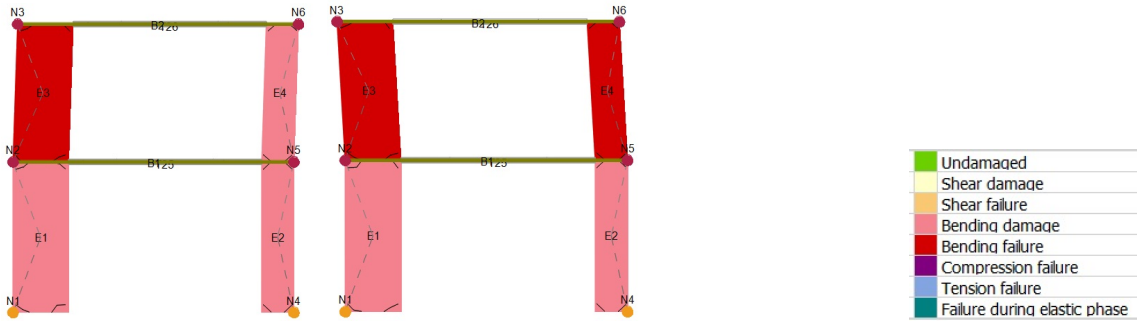

(a) Positive direction **(b)** Negative direction **(c)** Failure legend

Figure A.4: Failure mechanism of the encirclement with dimensions h=165 mm, w=100mm and concrete class C55/67.

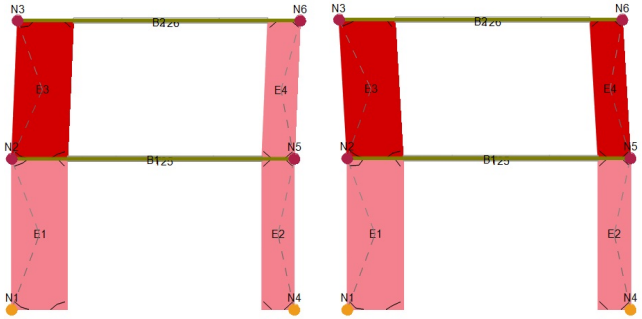

(a) Positive direction **(b)** Negative direction

Figure A.5: Failure mechanism of the encirclement with dimensions h=100 mm, w=100mm and concrete class C55/67.

B | INFLUENCE CONNECTIONS

In this section the influence of the connections will be clarified by an additional variation study. The variation study concerns the first case study: the relative simple two-storey URM structure which was tested in the TU Delft lab. The characteristics of this case study are introduced in Section 5.1. Two variations are made as regards the connection between the pier and the floor at the first level as visualized in Figure B.1a. It must be noted that the influence of the connections is not considered in the report and that this section serves as a clarification.

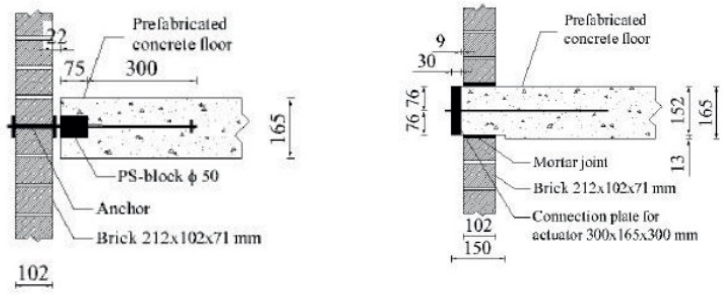

(a) Connection floor, pier **(b)** Connection floor, transverse wall

Figure B.1: Detailing first floor level case study 1.
Source: Esposito et al. (2017)

Variation 1: Floor imposed at pier on both levels

The connection of the pier and the floor at the first level, as visualized in Figure B.1a, is changed to the connection as visualized in Figure B.1b. In this variation the floor at the first level is imposed at both the piers and the transverse walls. The schematization of the loads of the new variation is visualized in Figure B.2. With the new connection, the piers are no longer spanning vertically between the ground floor and the second floor level. Consequently, the geometry of the piers has changed.

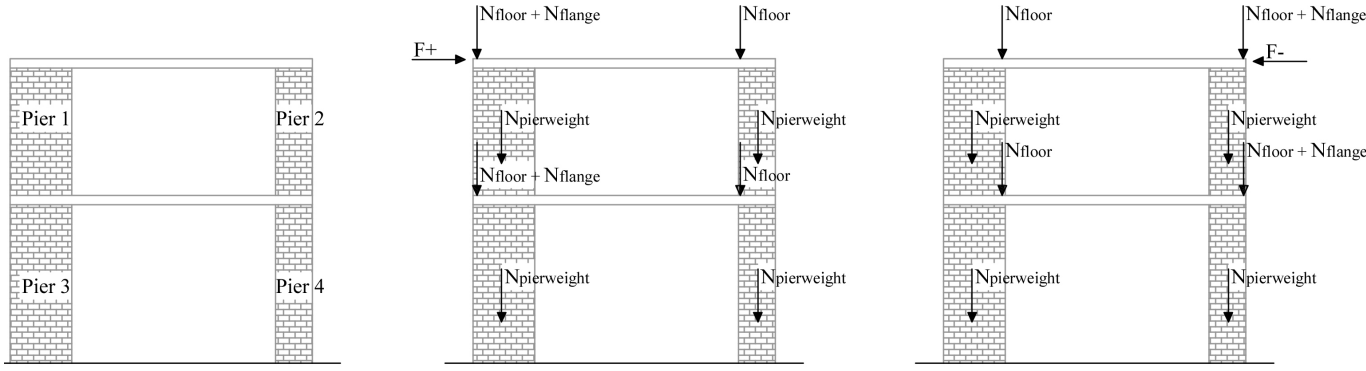

Figure B.2: Schematization of piers if the the first floor level is imposed at the piers

In Table B the resistance of the elements is visualized per pier in both the positive and negative direction. It must be noted that it is assumed that 25% of the floor load of both the first and second floor level is transferred to the piers during the analysis. The flexural failure mechanism is governing for all the piers, except pier 1. It must be noted that the diagonal tensile mechanism is here not taken into account since this failure mechanism is not relevant for this type of structures as explained in the report.

Table B.1: The resistance per element per failure mechanism for the new connection variation 1 (kN)

Element	Dir.	Sliding	Splitting	Flexural
Pier 1	+	25.4	19.9	20
	-	18.9	15.2	15.3
Pier 2	+	17.2	12	8.1
	-	23.6	16.5	10.1
Pier 3	+	49	34.2	32.3
	-	38.3	26.7	26.3
Pier 4	+	34.6	24.1	13.2
	-	45.3	31.6	16

In Figure B.3 the pushover curve of the individual elements is visualized. With the changed connection, both the geometry of the piers and the axial load in the elements has changed. This results into an increase of the lateral capacity, the compression strut is less steep and therewith the lateral resistance increases. The displacement capacity on the other hand decreases, this is related to the decreased slenderness ratio (H/L).

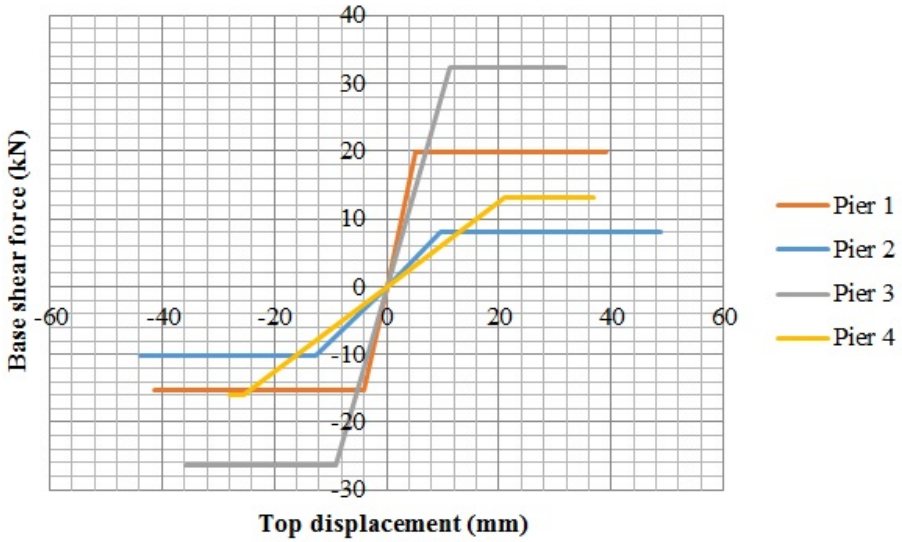

Figure B.3: Pushover curve of the individual piers if the floor is imposed on both the piers and transverse wall

In Figure B.4 the global pushover curve of the new structure is visualized. The capacity of the pier 1 to 4 is doubled since the structure is symmetric. The base shear capacity is 312% higher in the positive direction and 232% into the negative direction with respect to the original model. The changes are significant, but this is mainly related with the changes in the geometry.

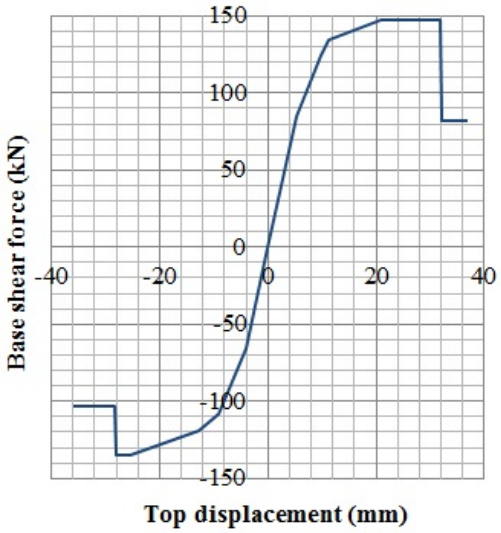

Figure B.4: Global pushover curve if the floor is imposed on both the piers and transverse wall

Variation 2: Floor connected with spring anchors

In the second variant the pier is horizontally dilated with respect to the first floor level. The floor is here connected to the piers with spring anchors which are only able to distribute the horizontal loads parallel to the facade. The floor at the first level spans thus between the transverse walls. Consequently, the load of the first floor level is only visible in the piers via the flange effect. With the horizontal dilatation the geometry of the piers is similar as variation 1, see also Figure B.2 for the geometry of the piers.
The capacity of the individual elements is presented in Table B.2, and visualized in Figure B.5.

Table B.2: The resistance per element per failure mechanism for the new connection variation 2 (kN)

Element	Dir.	Sliding	Splitting	Flexural
Pier 1	+	25.4	19.9	20
	-	18.9	15.1	15.3
Pier 2	+	17.2	11.9	8
	-	23.6	16.5	10.6
Pier 3	+	49	34.2	32.3
	-	23.8	17.3	17.2
Pier 4	+	20	14	8.4
	-	45.3	31.6	16

From the figure it can be derived that the changed connection only influences the lateral capacity of the element if the flange is not activated. If the flange is activated, the load of the first floor level is transferred to the piers via the flange. In Figure B.6 the global capacity of the new variation is visualized. The base shear capacity is 7% lower in the positive direction and 13% lower in the negative direction with respect to variant 1. The displacement capacity increased with respect to variant 1. This is related to the lower axial load on top of the piers, the stress in the compressed corner is relatively lower and therewith higher drifts can be obtained before failure.

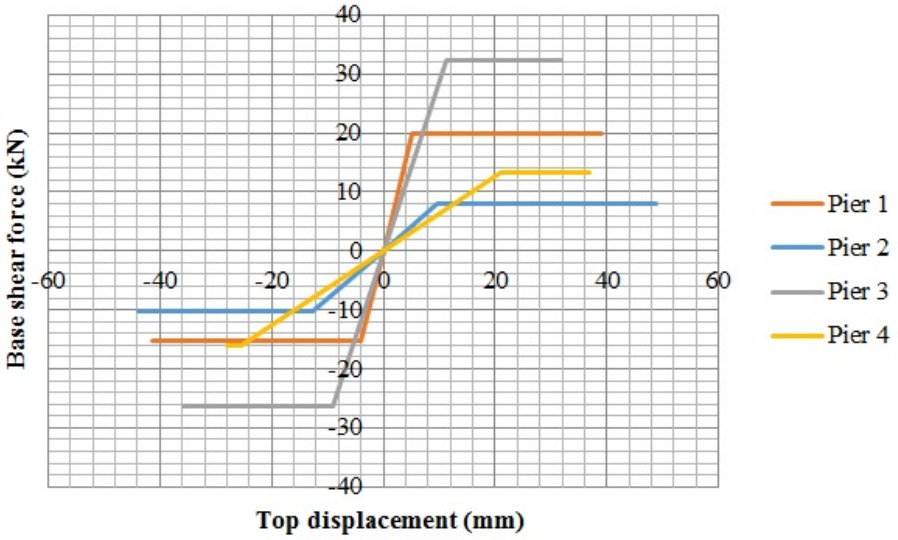

Figure B.5: Pushover curve of the individual piers if the floor at the first level is connected to the pier by a horizontal joint and spring anchors.

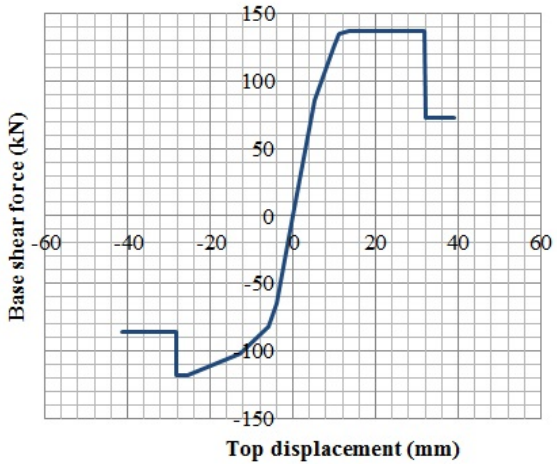

Figure B.6: Global pushover curve if the floor at the first level is connected to the pier by a horizontal joint and spring anchors.

In both the variances it is assumed that the flange is activated due to the interlocking effect of the bricks and the transverse wall. Another option would be that the transverse wall and the pier are connected to each other by a vertical joint and steel ties. In this case there is thus no interlocking effect between the pier and the transverse wall. The additional overburden due to the flange effect would no longer be visible in the adjacent pier. Therewith, the base shear force capacity would decrease significantly. However, this type of connection is not usual for these structures. and therefore not taken into account.

C MARTINI TYPE K DRAWINGS

FLOOR PLANS

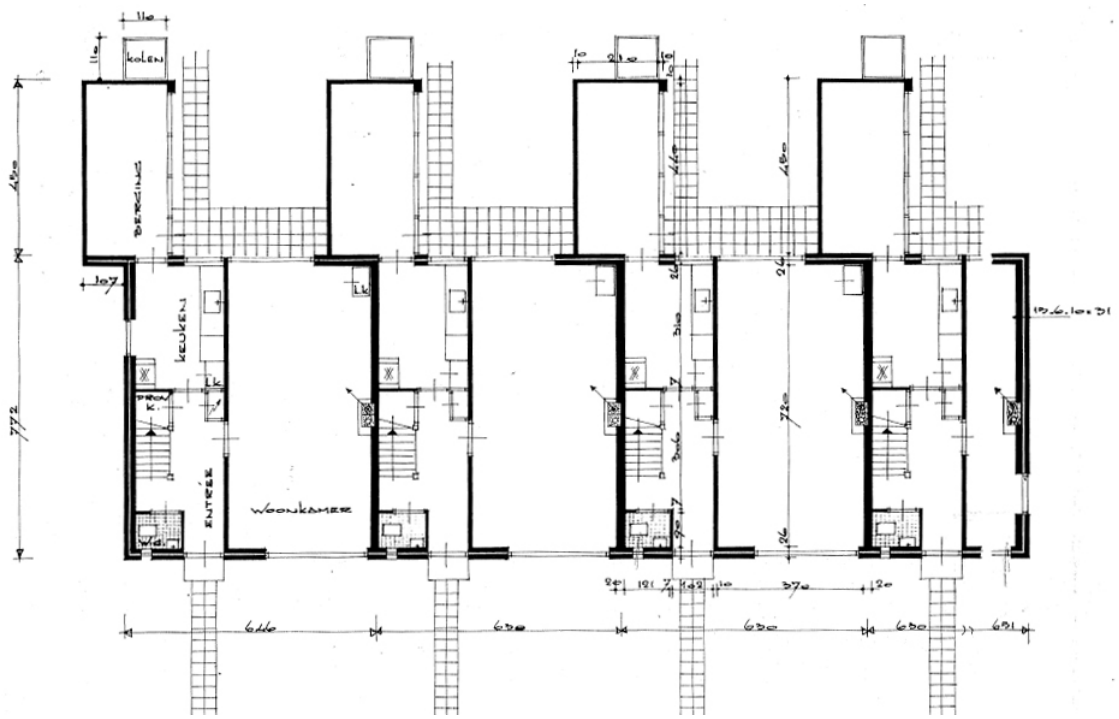

(a) Ground floor level

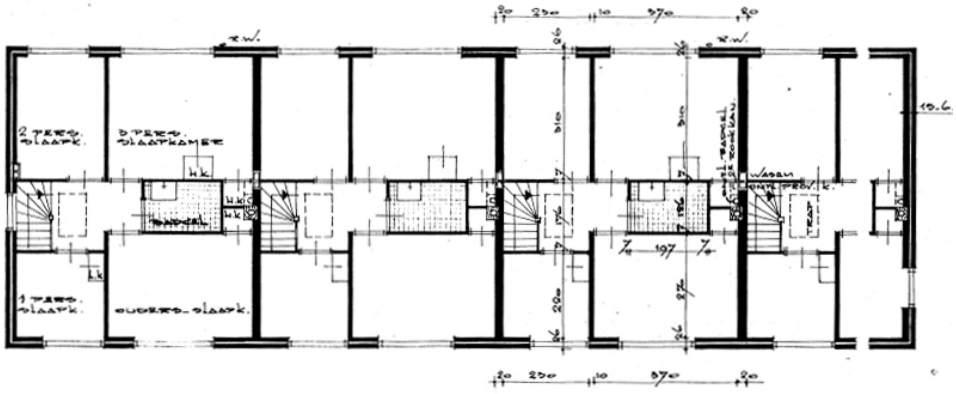

(b) First floor level

Figure C.1: Floorplans Martini type K.

Facade

(a) Front facade

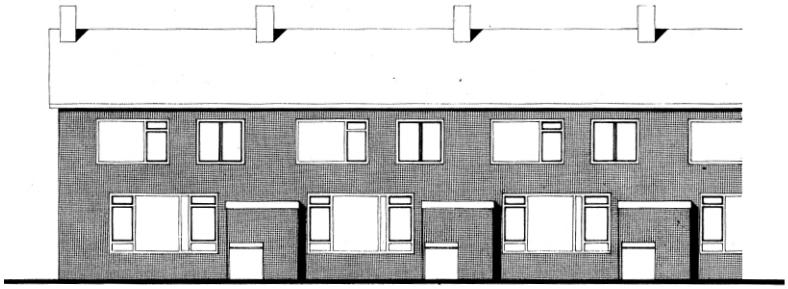

(b) Back facade

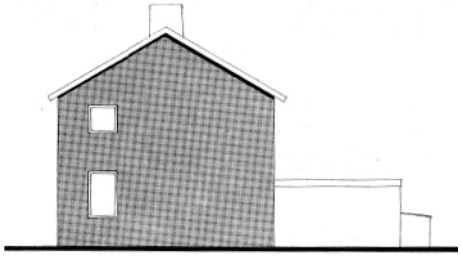

(c) East facade

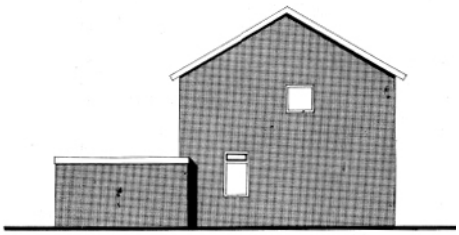

(d) West facade

Figure C.2: Facade Martini type K.

Section

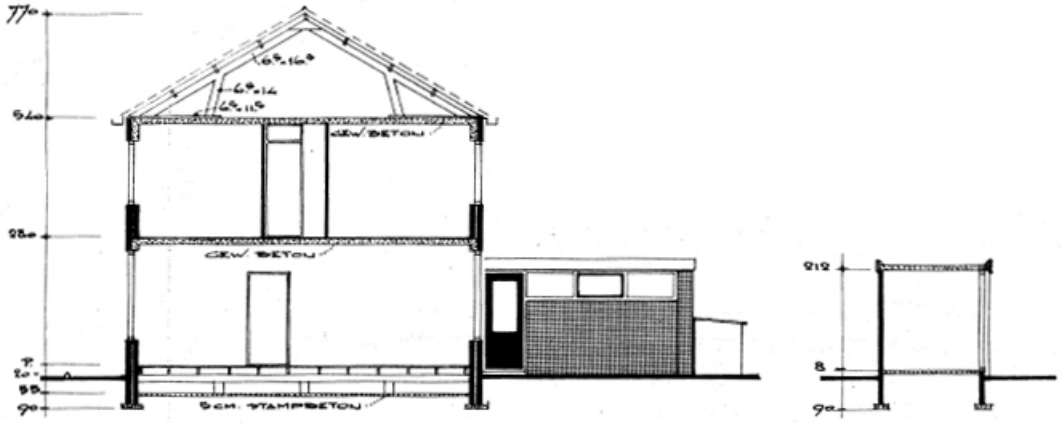

Figure C.3: Section Martini type K.

D PROPERTIES OF THE PIERS MARTINI TYPE K HOUSE

Properties of the piers loaded into the positive direction.

	Pier 1	**Pier 2**	**Pier 3**	**Pier 4**
Width [mm]	970	740	920	1390
Heigth [mm]	1900	1350	1350	2050
Flange	Yes	Yes	Yes	No
Axial loading [kN]	58.7	19.9	42.4	6.8
Governing failure mechanism	Flexure	Splitting	Splitting	Splitting
Shear force capacity [kN]	27	10.1	24.6	4.5

	Pier 13	**Pier 14**	**Pier 15**	**Pier 16**
Width [mm]	1220	480	490	650
Heigth [mm]	2050	1350	1350	1900
Flange	No	Yes	Yes	Yes
Axial loading [kN]	7.7	20.6	40.6	57.6
Governing failure mechanism	Splitting	Flexure	Flexure	Flexure
Shear force capacity [kN]	4.5	6.8	15.8	16.8

	Pier 5	**Pier 6**	**Pier 7**	**Pier 8**
Width [mm]	1540	1000	1480	410
Heigth [mm]	3000	1550	2700	2700
Flange	Yes	Yes	Yes	No
Axial loading [kN]	158.7	44.6	143.6	8.8
Governing failure mechanism	Flexure	Splitting	Flexure	Flexure
Shear force capacity [kN]	67.6	24.7	67.1	1.3

	Pier 9	**Pier 10**	**Pier 11**	**Pier 12**
Width [mm]	1810	350	1700	310
Heigth [mm]	2700	1550	2700	3000
Flange	No	No	No	No
Axial loading [kN]	24.1	12.3	25	5.1
Governing failure mechanism	Splitting	Flexure	Splitting	Flexure
Shear force capacity [kN]	15.4	2.5	15.0	0.51

PROPERTIES OF THE PIERS LOADED INTO THE NEGATIVE DIRECTION

	Pier 1	**Pier 2**	**Pier 3**	**Pier 4**
Width [mm]	970	740	1310	1390
Heigth [mm]	2050	1350	1350	1900
Flange	No	No	Yes	Yes
Axial loading [kN]	5.9	4.8	42.4	46.5
Governing failure mechanism	Flexure	Splitting	Sliding	Splitting
Shear force capacity [kN]	-2.8	-2.6	-34	-30

	Pier 13	**Pier 14**	**Pier 15**	**Pier 16**
Width [mm]	1220	480	1110	650
Heigth [mm]	1900	1350	1350	2050
Flange	No	Yes	Yes	Yes
Axial loading [kN]	60.3	20.6	40.6	3.5
Governing failure mechanism	Splitting	Flexure	Splitting	Flexure
Shear force capacity [kN]	-32.9	-6.6	-28.6	-1.1

	Pier 5	**Pier 6**	**Pier 7**	**Pier 8**
Width [mm]	1540	1000	1580	410
Heigth [mm]	2350	2700	1550	2200
Flange	No	No	No	Yes
Axial loading [kN]	16.3	16.3	18	81.3
Governing failure mechanism	Splitting	Flexure	Sliding	Flexure
Shear force capacity [kN]	-10.3	-5.9	-16.6	-10.2

	Pier 9	**Pier 10**	**Pier 11**	**Pier 12**
Width [mm]	1810	350	1700	310
Heigth [mm]	2200	2700	1550	2350
Flange	Yes	No	Yes	No
Axial loading [kN]	128.8	12.1	145.6	152
Governing failure mechanism	Splitting	Flexure	Splitting	Flexure
Shear force capacity [kN]	-80	-1.5	-104.5	0

E VARIATION STUDY

In this chapter the failure mechanisms obtained with the 3MURI models in the variation study of Chapter 7 are presented. The results are obtained according to the Eurcode 8 or the NPR9998-2018. In Figure E.1 the failure chart for both the guidelines is visualized.

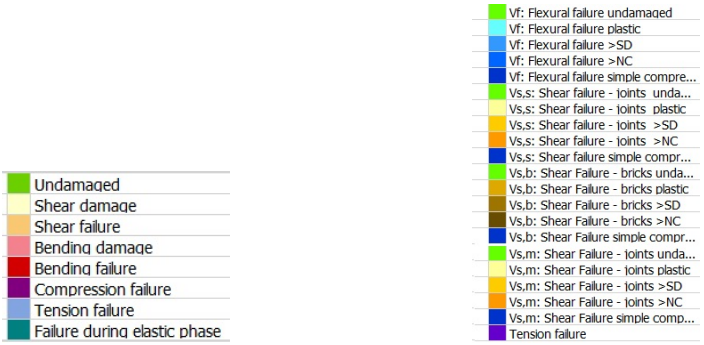

(a) Eurocode 8 **(b)** NPR9998-2018

Figure E.1: Failure charts of 3MURI for the guidelines.

HEIGHT = 950 MM

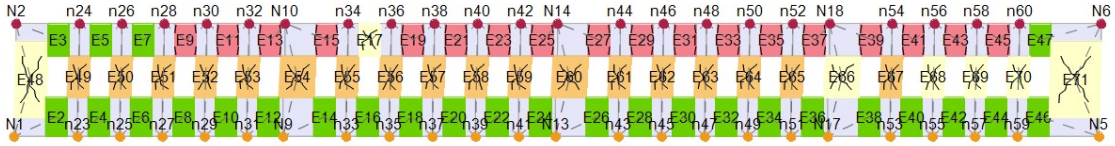

(a) Facade 1: 3MURI-EC8

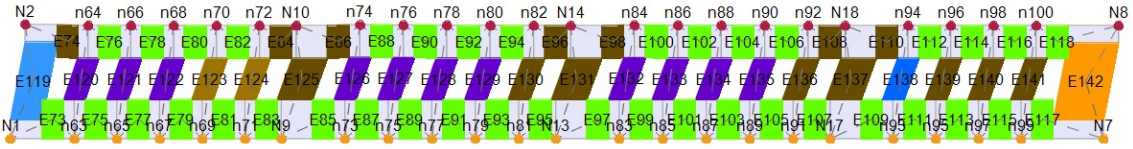

(b) Facade 1: 3MURI-NPR9998-2018

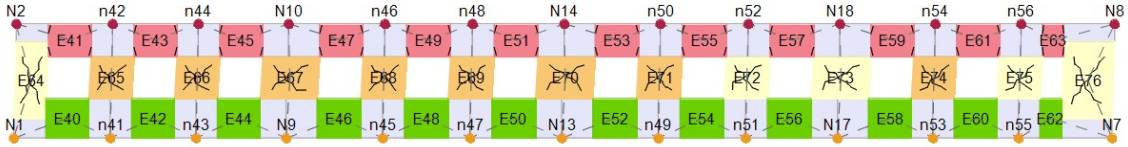

(c) Facade 2: 3MURI-EC8

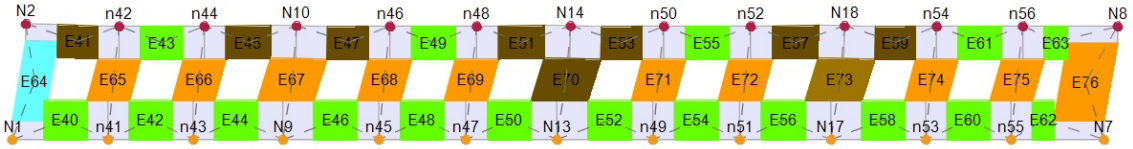

(d) Facade 2: 3MURI-NPR9998-2018

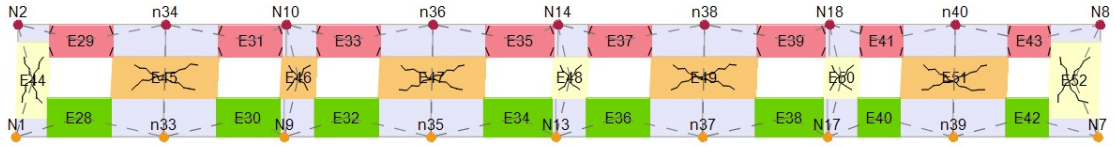

(e) Facade 3: 3MURI-EC8

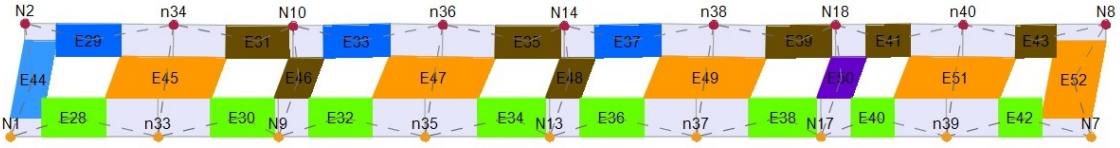

(f) Facade 3: 3MURI-NPR9998-2018

Figure E.2: Relation between the height and width of the piers and its governing failure mechanism into the positive direction.

HEIGHT = 1350 MM

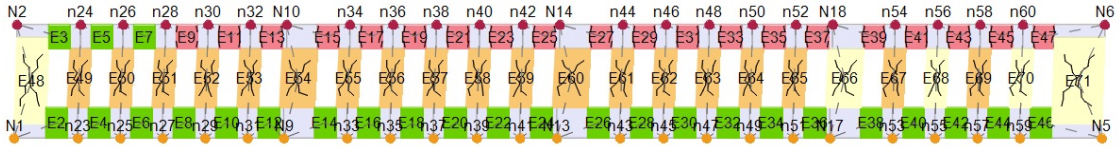

(a) Facade 1: 3MURI-EC8

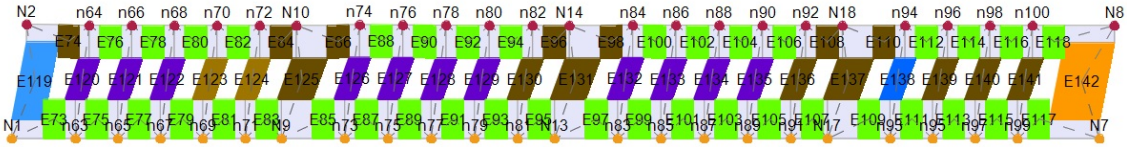

(b) Facade 1: 3MURI-NPR9998-2018

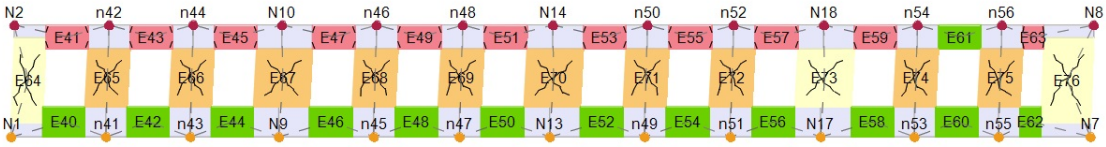

(c) Facade 2: 3MURI-EC8

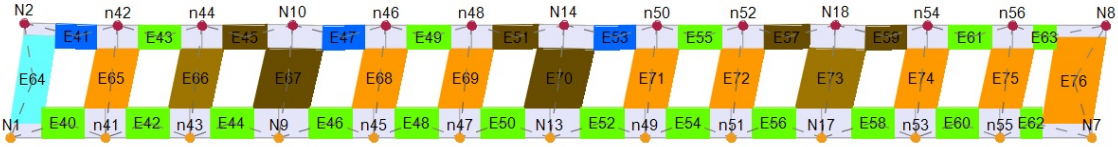

(d) Facade 2: 3MURI-NPR9998-2018

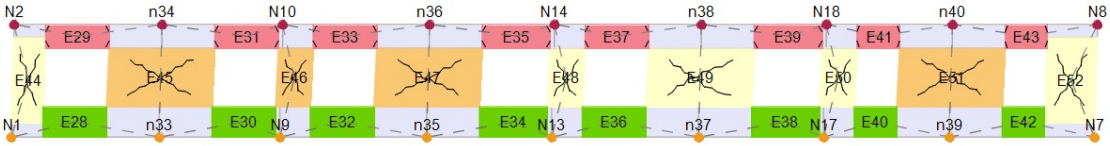

(e) Facade 3: 3MURI-EC8

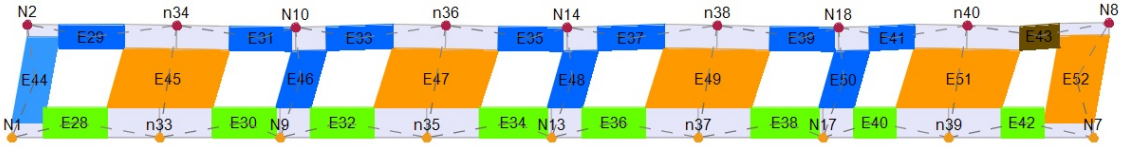

(f) Facade 3: 3MURI-NPR9998-2018

Figure E.3: Relation between the height and width of the piers and its governing failure mechanism into the positive direction.

HEIGHT = 1750 MM

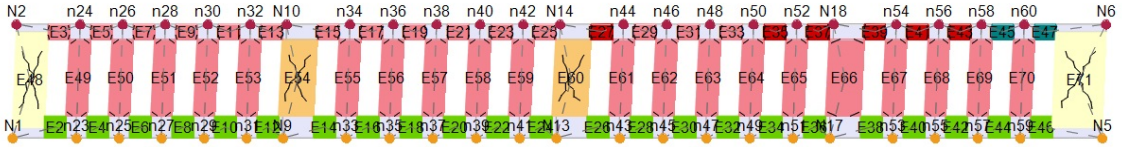

(a) Facade 1: 3MURI-EC8

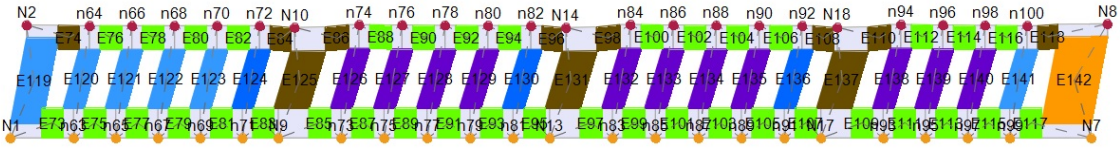

(b) Facade 1: 3MURI-NPR9998-2018

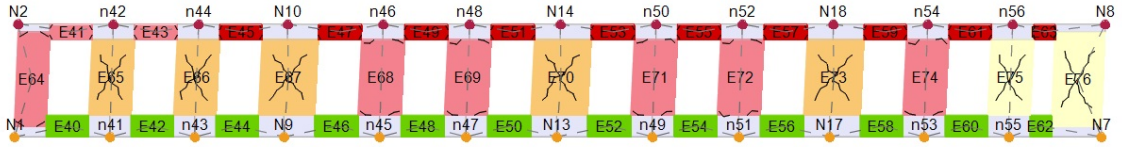

(c) Facade 2: 3MURI-EC8

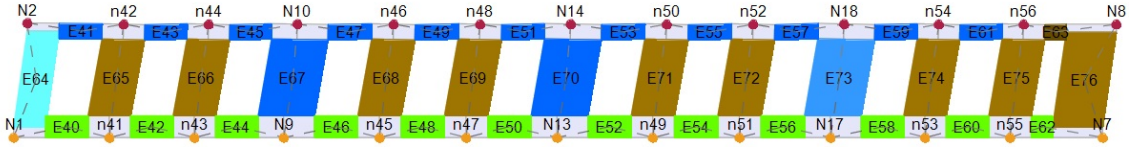

(d) Facade 2: 3MURI-NPR9998-2018

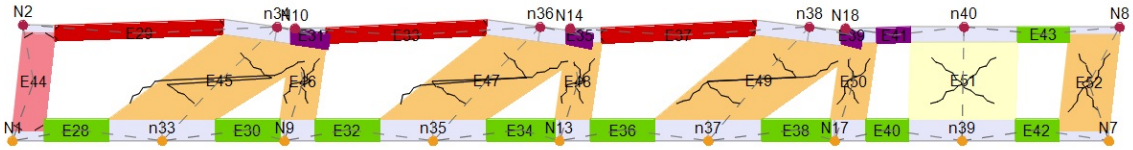

(e) Facade 3: 3MURI-EC8

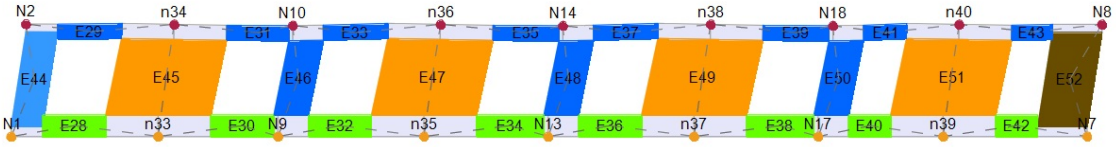

(f) Facade 3: 3MURI-NPR9998-2018

Figure E.4: Relation between the height and width of the piers and its governing failure mechanism into the positive direction.

COLOPHON

This document was typeset using LaTeX. The document layout was generated using the `arsclassica` package by Lorenzo Pantieri, which is an adaption of the original `classicthesis` package from André Miede.